Development of an Optofluidic Platform Based on Total Internal Reflection- Application of Dissolved Oxygen Sensing for Water Monitoring

By

Fei Du, B.Sc.

A Thesis

Submitted to the School of Graduate Studies

In Partial Fulfillment of the Requirements for the Degree

Master of Applied Science

in

Biomedical Engineering

McMaster University

TITLE: Development of an Optofluidic Platform Based on Total Internal Reflection- Application of Dissolved Oxygen Sensing for Water Monitoring

Author: Fei Du,

                          B.Sc., Peking University

Supervisor: Qiyin Fang, Ph.D.

Abstract

Water quality is of great importance to human as well as other forms of lives. The concentration of dissolved oxygen (DO) is one of the essential indicators for water quality. DO sensing has been widely used in many environmental applications such as natural water monitoring and waste water treatment. Three methods are currently used for DO measurement, namely titration, electrochemical and optical. In the optical method, DO is quantified by the reduction of fluorescence emission intensity of Ru based fluorophores through fluorescence quenching process. This optical method is compatible with autonomous DO monitoring while the titration method is not, and it has the advantages of faster response and higher sensitivity than the electrochemical method. These properties make the optical method suitable for surveillance of water quality over time as well as near real-time and high sensitivity detection of contaminations. In this thesis, we report the design, simulation, fabrication and characterization of a fluorescence quenching based DO sensing optofluidic device with the focus on sensitivity enhancement and cost/size reduction. In our method, DO detection sensitivity was improved by 4 folds through employing total-internal-reflection of the excitation light and optimizing the fluorophore film thickness in a multilayered microfluidic sensor structure. System cost and size were also reduced in this design.

Acknowledgement

I would like to express my sincere gratitude to my supervisor Dr. Qiyin Fang, who has always been helpful and has guided me through the whole course of this project. He has given me many opportunities to gain hands-on experiences in optics and also spent valuable time on reviewing and revising this thesis.

Thanks to Dr. Ravi Selvaganapathy and Dr. Herb Schellhorn, who have been the members of the Examining Board and provided valuable comments on this work.

I would also like to thank to my collaborator Mr. Leo Hsu, without whom this project cannot be realized. Also thanks to other members of Biophotonics group at McMaster University, including Dr. Samir Sahli, Dr. Allison Yeh, Dr. Zhaojun Nie, Mr. Anthony Tsikouras, Mr. Du Le, Mr. Ramy Yehia, Ms. Sharon Goh, Mr. Eric Mahoney, Mr. Ian Phillips, Mr. Nehad Hirmiz and Dr.Wenbin Zhang. They have always been helpful and encouraging, and created such a cozy environment in our lab.

Finally, I would like to thank my family and my boyfriend Ivan for their continuous love and support. The experience of M.A.Sc study has taught me to appreciate their love and love them more.

Table of Contents

List of Abbreviation

BSA: bovine serum albumin

CCD: charge-coupled device

CMOS: complementary metal-oxide-semiconductor

DO: dissolved oxygen

DOA: bis(2-ethylhexyl)adipate

DOP: dioctylphthalate

DOS: bis(2-ethylhexyl)sebacate

E.Coli: Escherichia coli

FIB: fecal indicator bacteria

FWHM: full width at half maximum

LED: light emitting diode

NA: numerical aperture

OD: optical density

ORR: oxygen reduction reaction

PDMS: poly(dimethylsiloxane)

PMMA: poly(methylmethacrylate)

PMT: photomultiplier tube

PS: polystyrene

PVC: poly(vinyl chloride)

poly(TMSP): poly (1-trimethylsily-propyne)

SERS: surface enhanced Raman scattering

SPR: surface plasma resonance

TIR: total internal reflection

Chapter 1   Introduction

Water quality is essential to human health, environment, agriculture and industry. Dissolved oxygen (DO) serves as one of the most important indicators of water quality. Multiple methods exist for DO measurement and they are suitable for different applications and scenarios. In this chapter, the significance of water quality and the classification of aqueous pollutants are introduced in Section 1.1. The role DO plays in water quality monitoring is described in Section 1.2. Section 1.3 gives an overview on different methods used for DO measurement, with a focus on the optical method. Section 1.4 lists the basic requirements for DO sensors in environmental applications. Section 1.5 touches the current problems for existing DO sensing techniques. Detailed targets for the optical DO sensor design in this work are given in Section 1.6.

1.1 Water quality crisis

Water quality is very important to human and wildlife [1]. To begin, human health is directly linked with the quality of water for drinking and other purposes. Microbes or chemical contaminants in drinking water may cause serious diseases: for example, Escherichia Coli (*E. Coli*) can cause diarrhea and even death in immunocompromised individuals; Dracunculiasis leads to allergic reactions, nausea and vomiting; arsenic ions contribute to skin cancer and cardiovascular diseases; long-term excessive consumption of aluminum leads to Alzheimer's disease [2]. The microbes in beach and river water for swimming and clothes washing can also enter into the human body through mucosa and result in sicknesses. Besides its importance to human health, water quality is essential for the environment because polluted water cannot sustain normal flora and fauna [1]. A variety of factors, such as a drop in DO concentration and a severe eutrophication in natural water, lead to marine species loss and deterioration of aquatic ecosystems [2]. A reliable supply of water with acceptable quality also plays a vital role in agricultural and industrial production worldwide [1].

Increasing population and pollution results in a water crisis worldwide, which indicates both water shortage and quality degradation [3]. Pollution is one of the main reasons for water quality degradation. Water pollutants could be classified into four categories, namely chemical, physical, radioactive and pathogenic pollutants [3]. Chemical and pathogenic pollutants are the sources of most common and disease-causing water quality issues and have attracted attention for control, detection and remedy research for decades [3]. Chemical pollutants refer to chemical ions or molecules that are disposed into natural water. Their existence or amount exceeds the self-cleaning capability of natural water and leads to adverse effects on the water communities, e.g. species loss and/or disruption of food chains [4]. Chemical contaminants, especially heavy metal ions and chlorine-based disinfectant by-products, also significantly increase the incidence of various cancers, reproductive problems and neurologic diseases after intake of polluted water [4]. In comparison, pathogenic contaminants in natural water refer to the microbes that commonly come from agricultural and municipal sewage, especially human and animal fecal waste. The quantification of fecal indicator bacteria (FIB) remains one of the most common methods to monitor water quality and to forecast microbial pollution outbreaks [5]. These pathogenic microbes in drinking water give rise to fecal-mouth transmission of various diseases. Considerable attention towards drinking water quality has been drawn in Canada since two consecutive water-borne disease outbreaks: the Walkerton, Ontario *E.coli* incident in 2000 and the North Battleford, Saskatchewan Cryptosporidium incident in 2001 [6]. Consensus has been reached that chemical and pathogenic contaminants act as the most tangible and dangerous risks to drinking water safety [6].

Continuous and rapid sensing techniques should be in place for these contaminants to monitor natural water quality. These services can function as a warning system to apply remedy methods, e.g.

recommending further purification steps by users (such as filtering, chemical treatment and boiling for drinking water) and/or cutting off the water supply [6]. Yet current monitoring systems for water quality are far too labor intensive and time-consuming, which led to limited number of analytes, high cost and slow response time. Consider the Walkerton *E.Coli* outbreak as an example. A drinking water sample was collected on May 15 2000, but it was not tested to show E. Coli contamination until May 17 when the first groups of victims started to have symptoms associated with *E.Coli* [7]. For complicated contaminants sensors which directly screen chemical and pathogenic pollutants, the current target for design and implementation is to reduce the processing time from several days in laboratory to near real-time on-site monitoring [8].

1.2 Dissolved oxygen as an indicator of water quality

Besides direct monitoring of water contaminants, some attributes of water could act as indicators of overall water quality [9]. These attributes range from temperature and pH to salinity and turbidity [9]. The concentration of DO is one of the essential attributes that indicate water cleanliness [10]. DO concentration can be representative of organic contaminations in water: organic chemical pollutants arouse microbial oxygenation, in which oxygen molecules are rapidly consumed. As oxygen level decreases, aerobic organisms perish and anaerobic microbes prosper, leaving the water with toxic substances from anaerobic metabolisms and destroying the aquatic ecosystems [10].

In this section, we first discuss the characteristics of DO monitoring in natural water and then consider the control of DO concentration in waste water treatment.

DO in water are the oxygen molecules that are not chemically bonded to other elements [11]. A proper range of DO concentration is essential to the survival and progeneration of all forms of aquatic animals, plants and microbes: oxygen consumption is necessary for the respiration of all aerobic creatures and thus supports the functioning of ecosystems [1]. Oxygen in water is obtained by aquatic photosynthesis or by entry from the air. The DO concentration depends on multiple factors in natural water, and this dependency influences how we set the 'proper range of DO concentration' for each location: DO is stratified with depths in water, generally decreasing at greater depths due to photosynthesis reduction [12]; DO concentration is dependent upon physical factors such as pressure, temperature and salinity, which change the solubility of oxygen in water [12]; field measurements reveal that DO concentration also fluctuates within a day and with different seasons at the same location [12]. Typically DO sensors for field use in natural water require a measurement range of 0-10 ppm (mg/L), which is well below the saturation level of oxygen in water under atmosphere pressure (40 ppm) [13].

The gap is impressively huge between ideal and realistic situations of DO monitoring in natural water. Consider Lake Ontario as an example. The surface area of this lake is 19,000 km^2 [14]. As described in Great Lakes Surveillance Program by Environment Canada, a total number of 80 on-line sensors are desired at different locations in the lake and hourly results are in demand for timely prediction of microbial pollution outbreaks [14]. Yet the realistic situation is another story: only one DO sensor is involved in the monitoring of Lake Ontario, and marine technicians ship around the lake to measure DO amount at different locations once per month [14]. This colossal difference indicates that considerable development of DO sensors for environmental applications is urgently required. For example, to increase the quantity of DO sensors, single sensor cost is needed to be reduced significantly.

Besides in natural water, DO concentration is important to monitor in waste water treatment plants. Oxygen must be supplied in the oxygenation process of organic contaminants and it functions as an indicator for the clearance of these organic contaminants as well. Waste water treatment typically consists of the primary treatment and the secondary treatment [15]: solid physical pollutants such as glass, twigs, rocks and soil are filtered in the primary treatment process and contaminants are chemically targeted

during the secondary treatment [15]. To eliminate organic wastes in water, certain microorganisms capable of decomposing organic substances are added to the waste water in aeration tanks; sufficient oxygen (in the form of pure oxygen gas or air) is also supplied continuously in this process [16]. DO concentration in this tank is carefully monitored until it recovers to the normal range (6-8 ppm), which signals the completion of organic treatment and prepares the water for direct discharge into natural watercourses [16].

Oxygen pumping process can take up 30% - 60% of total power consumption in waste water treatment plants [17]. Real-time and more accurate monitoring of DO concentration is capable of cutting off the oxygen supply in time, which avoids unnecessary pumping. It is estimated that up to 50% of power consumption in the oxygenation process could be saved given sufficiently accurate DO monitoring [17].

In summary, the importance of DO concentration is reviewed in this section. In natural water, an appropriate DO level is integral in sustaining a healthy ecosystem and it also functions as an indicator of organic chemical contaminants. In waste water treatment, DO is supplied in the process of organic treatment and DO monitoring has profound influences on the energy cost reduction. Based on what we discussed in this section, accurate, near real-time and less-costly DO sensors are in high demand for environmental applications [18].

1.3 Overview of DO measurement

Three methods are used for measuring DO concentration in water: chemical, electrochemical and optical [18]. Extensive investigations have been conducted over the past several decades to develop reliable DO sensors based on these methods [18]. We review the three methods respectively in this section and compare their benefits and limitations.

Chemical methods for DO measurement which use chemical reactions with oxygen were developed initially and still remain the most reliable methods for DO monitoring: the most well-known Winkler method is considered the gold standard of DO measurement [19]. The Winkler method typically involves two steps: first, mix water with manganese (II) salt, iodide (I^-) and hydroxide (OH^-) ions to form a precipitate, which is oxidized by DO in the sample and becomes yellow. In the second step, the reaction of the yellow precipitate and a strong acid which is further added to the sample converts iodide ion (I^-) to purple iodine (I_2), which could be observed by color change (when starch is present) or automatically monitored at 680 nm by a spectrometer [19]. In this measurement the amount of DO is proportional to the titration of iodine with a thiosulfate solution [19]. The Winkler method provides a very accurate way to measure the amount of DO in water sample, yet the titration process either requires lab work which cannot be operated automatically or necessitates flow control units and chemical reservoirs in spectrometer monitoring. These complex modules make it very costly to build an automatic DO sensor based on the Winkler method [18].

The electrochemical DO sensor is a miniaturized electrochemical reaction pool and often based on Clark electrodes configuration [20]. In such configuration, the working electrode is a catalyst (usually Pt) which can trigger oxygen reduction reaction (ORR); it is placed along with a silver/silver chloride reference electrode and a counter electrode in a standard electrolyte solution. All these electrodes are separated from the external environment by a gas permeable membrane which is usually made of Teflon [20]. Application of a constant electrical potential at the working electrode leads to the establishment of an electrical ORR current that is proportional to the diffusion speed of DO in the electrolyte (from the external environment through the membrane to the working electrode) [20]. Thus the DO concentration in the external environment can be calculated directly from the electrical current obtained in the stable stage. This method is simpler than titration in terms of system configuration, which is favorable for low-cost sensor development [20]. Nevertheless, there are still some common drawbacks of electrochemical

sensors such as a rather long time to establish stable current and a limited device lifetime because of the aging of the catalyst electrode [20].

In optical DO sensing, oxygen molecules are quantitated based on their ability to reduce the intensity of fluorescence emitted by excited fluorophores (e.g. $Ru(dpp)_3^{2+}$). This process is called oxygen quenching. The fluorophores are typically immobilized in a polymer matrix and incorporated into an optical system, which also includes a light source, an optical detector and an emission filter etc. We will explain the details of oxygen quenching principles in this section as below: Jablonski diagram is generally used as the physical model of the quenching process and Stern-Volmer equation is used for mathematical expression.
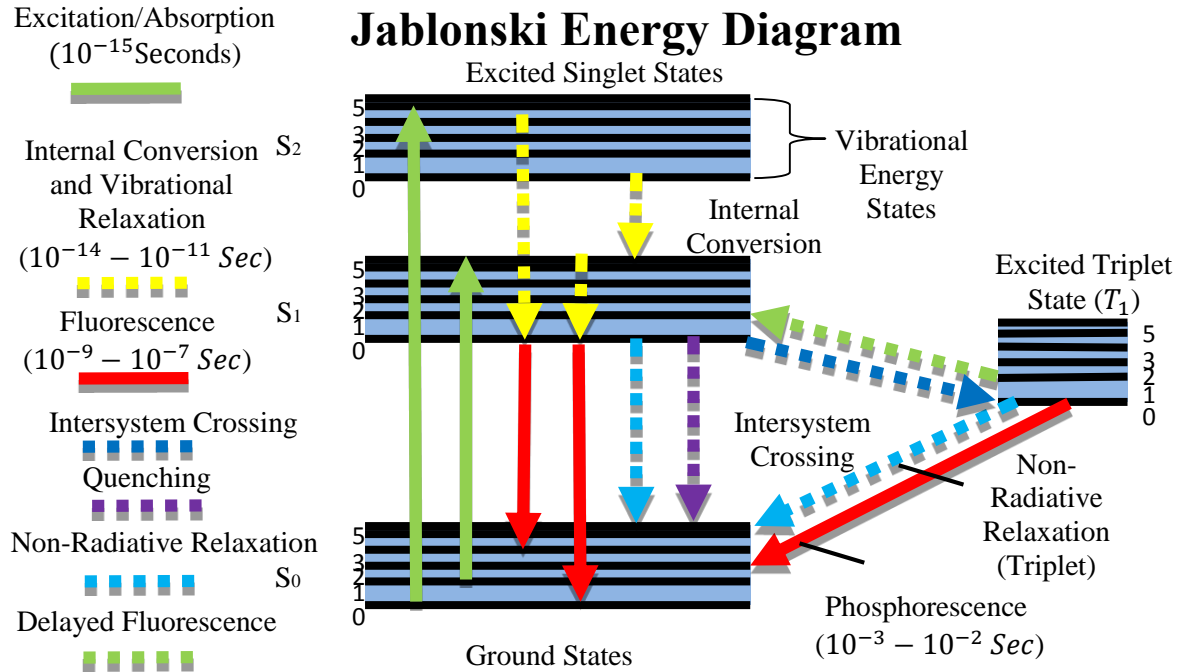

Figure 1.1 Jablonski energy diagram for explanation of related processes in fluorescence. The emission of light results as electrons drop down from excited electronic states to some levels in S_0 state; then the electron is quickly thermally relaxed to the ground vibrational level in S_0 [21]. Because of the tendency to maintain atomic geometry pattern, the jump back of the electron is likely to reach the same vibrational level in S_0 as the destination vibrational level in the excited electronic state when light absorption occurred before [21]. This fact gives rise to the phenomenon that shapes of excitation and emission spectra, which depict vibrational levels distribution, often have mirror symmetry [21].

The emission of light from a material which is optically excited is called luminescence, which is usually depicted by Jablonski diagram (Figure 1.1) [21]. Jablonski diagram shows the distribution of different electronic energy levels in certain material. Light absorption and emission are typically related to jumps between different electronic states of the substance, e.g. singlet ground state (S_0) and first or second excited states (S_1 or S_2). Within each electronic state, there are multiple vibrational states (illustrated by 0, 1, 2 in Figure 1.1). Although each vibrational level can be further subdivided into different rotational energy levels, a typical Jablonski diagram omits such details. Light absorption can excite the substance from singlet ground state to higher electronic states, and then, without any light emission, the substance

rapidly decays to the first vibrational level in this electronic state due to thermal relaxation [21]. Specifically if the vibrational levels strongly overlap different electronic states, the reduction from some vibrational levels in S_2 or higher to the ground vibrational level in S_1 is termed internal conversion [21].

The light emissions that happen between different singlet electronic states, as we described before, are termed fluorescence, which has a comparatively shorter lifetime (the term fluorescence is also used to replace the word luminescence sometimes). In the excited electronic states, the molecule can also undergo 'intersystem crossing', in which the electron transfers from the singlet electronic state to a lower-energy triplet state [21]. As objects to Pauli Exclusion Law, the jump back from excited triplet states to ground singlet state (termed phosphorescence) takes a much longer time compared to fluorescence [21]. Heavy metal atoms in molecules, act either as the central atoms or a substituent in the ligand, increase the chances of intersystem crossing and thus elevate the light emission efficiency of phosphorescence (up to unity) [21].

Several concepts and rules that are frequently used in fluorescence and phosphorescence are worth elaboration here. The quantum yield (also called quantum efficiency) is the ratio between the number of photons emitted and the number of photons absorbed, based on which the energy transfer efficiency could be calculated. The lifetime of the excited state is the average time the fluorophores spend in the excited state before returning back to the ground state. For a single exponential decay this lifetime is defined by the time it takes for 63% of molecules to decay back to the ground state [22]. Stokes shift refers to the phenomenon that the emitted light generally has a longer wavelength and lower energy than the excitation light; this term is also used to describe this wavelength shift [22]. The Stokes phenomenon is due to various energy losses between the moments of light absorption and of fluorescence emission that we mentioned before. Photobleaching is the permanent loss of luminescence capability, usually resulting from a change in chemical structure of the substance due to excessive light excitation [22].

The intensity of the emitted light can be reduced via various processes. Quenching is the term to describe the phenomenon that the intensity (and sometimes lifetime) of emission decreases only in the existence of quenchers, which is different to the permanent photobleaching. Quenching can be categorized into collisional quenching and static quenching. Collisional quenching is the energy transfer during bimolecular collision between the excited fluorophore and the quencher, during which the fluorophore is relaxed to the ground state and the quencher is excited; collisional quenching reduces the fluorescence lifetime as well as emission intensity [22]. Oxygen is a well-known quencher to many luminescence processes. When the concentration of fluorophores exceed certain thresholds, they could also quenched by collision together with themselves and/or with solvent molecules [21]. In contrast, static quenching is the bimolecular combination of the fluorophore and the quencher; the combination is unable to fluoresce. This process happens in ground electronic state and could be regarded as the reduction in the number of fluorophores, which only affects luminescence intensity.

Besides Jablonhski diagram which describes the physical processes of luminescence and quenching, Stern-Volmer equation is employed to mathematically calculate reduced emission intensity in the presence of certain quencher concentration. If we specify oxygen as the quencher, the equation could be written as

$$\frac{I}{I_0} = \frac{\tau}{\tau_0} = 1 + k_0\tau_0[O_2] \qquad (1\text{-}1)$$

Where k_0 is the Stern-Volmer constant, I_0 and I are the emission intensities, and τ_0 and τ are the lifetimes without and with oxygen quenchers respectively [21]. Quenching rate constant, k_q, is related to the Stern-Volmer constant k_0 and dependent upon various physical parameters of the sensing system; it could be described by the modified Smoluchowski-Einstein equation as

$$k_q = pk_0 = 4\pi N_A(D_f + D_q)pR \times 10^{-3} \qquad (1\text{-}2)$$

where D_f and D_q are the diffusivities of the excited fluorophore and of the quencher, respectively, p the quenching probability per collision between the fluorophore and the quencher, R the sum of collision radii $(R_f + R_q)$ and N_A the Avogadro number. D_f could be omitted if it is significantly smaller than D_q in polymer matrices [23].

The slope in the Stern-Volmer equation, which is k_0 times τ_0, is generally representative of the sensitivity in DO measurement systems. From the equations above, we see that longer lifetime of fluorophores and higher oxygen diffusivity are the two most flexible parameters that could be easily changed using different materials in DO sensing systems [23]. These two factors are determined respectively by the type of fluorophores and their surrounding environments (which usually imply immobilized polymer matrices).

To summarize, different methods to measure DO concentration, including chemical, electrochemical and optical methods, were reviewed in this section. The optical method based on oxygen's role in fluorescence quenching was discussed in detail, as it demonstrates the potential for easy automation, fast response time, good sensitivity and long sensor lifetime, which was superior to the other two methods. However, the expensive optical components which are integral in fluorescence based DO sensing system make it less attractive for mass use [23]. As one of the most common ways to reduce system cost and to further increase response speed, miniaturization on the system level is a key to the development of optical DO sensors [23].

1.4 Requirements for environmental applications

Oxygen sensors have been used in different settings and applications, ranging from medical monitoring to food packaging and combustion gas control in automobiles [24]. The design and implementation of oxygen sensors vary significantly among different applications, in response to specific requirements in each case [24]. Basic requirements of DO sensors for environmental applications are discussed in this section, and the desired sensing method, materials and sensor configurations could be suggested.

First, automated and continuous monitoring capability (rather than one-time use) of DO sensors are highly desired in environmental applications, as it is impractical to perform such measurements manually over large areas [24]. Besides, long device operation lifetime (time interval without the need to repair or replace) is required, which can further reduce the labour cost [24]. In applications targeting waste water treatment plants, a near real-time response of the sensor accurately controls the oxygen amount in bioreactors, saving power energy cost [16]. All these properties imply the desired sensing method for environmental applications: the optical method is considered advantageous based on what we discussed in Section 1.3.

In addition, low cost and small size would make DO sensors more attractive in environmental applications. Cost reduction could lead to an increased quantity of DO sensors in natural water monitoring, giving a more detailed and reliable measurement result. In the bioreactors in waste water treatment plants, multiple DO sensors could be located at different places in the same bioreactor, to precisely monitor the DO concentration distribution and to cut off oxygen supply accordingly [16]. Miniaturized DO sensors would fit into the settings with space limitations more easily. The cost/size reduction of DO sensors can be achieved by use of simple optical parts, use of cost-friendly fluorophores, and mature microfabrication techniques in optical DO sensors.

In the end, biocompatibility (non-toxicity) is required in environmental applications [17]. This criterion limits the choices of fluorophores and of polymer matrices in the sensor. As we will mention in Chapter 2, biofouling is a process occurring in natural and waste water that significantly degrades sensor

performances, so the compatability of anti-biofouling treatment is another factor to consider when choosing sensor materials [25].

1.5 Current Problems for Existing Technologies

There are a number of drawbacks that limit the use of existing DO sensors in environmental applications. In this section we would discuss the main challenges in current DO technologies. These problems are taken into consideration in the design of the optofludic DO sensor in this work.

The high cost of individual DO sensor is one of the main limitations preventing its wide use. For an advanced sensor with good DO accuracy (0.2 ppm or higher), the price of a commercially available electrochemical device exceeds US $200 and the price of an optical option goes beyond US $700 [26]. The operation cost is even higher considering the short lifetime of the sensor membrane (elaborated in Section 2.4). Biofouling occurs in both freshwater and marine environment, which is the limiting factor of the membrane lifetime. Membranes without anti-biofouling treatments completely lose their performances within a single day in water. Even with state-of-the-art anti-biofouling techniques, sondes of the sensors need to be replaced within 60-90 days in freshwater and within 45-90 days in marine [26], probably much shorter in waste water treatment applications.

Besides the cost of DO sensors themselves, installation, calibration and maintenance are a major part in the total operation cost of the sensors. Both electrochemical and optical sensors require regular calibration to overcome drift: daily calibration is suggested for electrochemical sensors and every a few months for optical sensors. The calibration is usually performed by sensing air saturated water and/or water saturated air by human manipulation. In addition to calibration, the sensing elements in both types of sensors also need to be changed regularly because of degradation. The Pt catalyst for ORR in electrochemical sensors ages with time, and the reaction pools are better to be replaced every 2-8 weeks [26]. The fluorophores in optical sensors will photobleach and lose their fluorescence capability, which requires replacement annually. These service requirements significantly increase the operation cost of DO monitoring; they also make the results from DO sensor less believable in waste water treatment plants, where the current practices are to ignore the DO readings but continuously pump up oxygen as suggested in the operation manual [27].

Furthermore, electrochemical DO sensors have another pitfall that they can only work in flowing water environment. Oxygen molecules are consumed in the sensing process, so the water sample near the sensor needs to be refreshed on a continuous basis to prevent bias. Besides, the size of DO sensor probes could be as long as 35 cm (Horiba^{TM} sensor we used in this work), which becomes problematic on certain conditions where a miniaturized device is desired.

1.6 Goals for this work

In Section 1.4, we listed a number of requirements for DO sensors designed for environmental applications. Although a portion of these criteria have been met in some existing technologies, they separately target different aspects of specific applications. Their possibilities of combination and influences on the system performance (e.g. DO sensing accuracy) remain undeveloped. In this section, several factors we mentioned before are listed as the targets in this project, and all the work hereafter follow one or more of these goals.

- **Automation**

In the three typical methods of DO measurement, the operation of titration typically requires the labor of a technician; thus titration is the least suitable method for autonomous applications. Although the operation

of electrochemical sensors is autonomous, as we mentioned in Section 1.5, they require more labor work in terms of calibration and maintenance compared with optical sensors. For applications that target to long-term automation of DO sensing, we choose the optical method as the focus in this project.

- **Low cost**

As we mentioned in Section 1.2, cost reduction in DO sensors is desired for water monitoring in large areas. Besides the basic fluorophores and polymer matrices, an excitation light source, an optical detector and one or more optical filters are integral parts in the optical sensing system. When the budget for the whole system is limited, we try to use a cost-friendly combination of these optical parts in this project. For example, lasers are typically used in optical DO sensing systems for their high power and wavelength coherence; yet lasers are much more expensive than diode lasers and light-emitting diodes (LED) [27], which we turn to in this project. In addition, some existing technologies employed spectrometers as the optical detectors, which differentiate the excitation and emission wavelengths on their own; in this work we would use lower-cost photodiodes or optical power meters as the detectors, which function as well together with an emission filter. Furthermore, a carefully chosen diode laser would be applied, with proper central wavelength and FWHM (full width at half maximum) to omit the excitation filter in this system. We also try to discover the minimum size of the emission filter in the design process, in order to potentially reduce the filtering material cost.

- **Miniaturization**

Miniaturization is another objective in this project. As we mentioned above, it is one of the most common means to achieve cost reduction, and it also stands as a future direction in itself [28]. In this project, we try to realize device miniaturization by reducing the structure sizes. Microfabrication techniques are employed and fast prototyping is accomplished by using an optofluidic platform [29]. With the use of 3D-printed molds in soft lithography process, PDMS sensor structures could be realized with resolution under 100 μm [29]. Besides fabrication, we discuss different methods and their effects on size reduction in the design and characterization as well.

- **Sufficient sensitivity and accuracy**

Much more often than not, a consequence of system cost/size reduction is performance degradation, which is hard to mitigate [28]. Hence one of the goals in this work is to maintain good sensing performances, represented by sensitivity and accuracy, at a reduced cost and size. Sensitivity enhancement methods are considered in this project, and different methods are evaluated and compared. Total-internal-reflection (TIR) is selected eventually for its reliability, controllability and thus suitability for mass production. A detailed review of TIR application in optical DO sensors could be found in Chapter 2. The influences of sensor structures and different optical parts on the sensitivity are also discussed in the design and characterization.

Chapter 2   Literature review

Water quality is essential to human lives. Dissolved oxygen (DO) concentration serves as an important indicator of water quality. DO sensors are required for water monitoring. In different DO sensing methods, the fluorescence quenching based one has the advantages of continuous capability, fast response and high sensitivity. Optofluidic sensor structure could be employed in DO sensors to realize cost/size reduction. In order to maintain good sensitivity at a reduced cost and size, sensitivity enhancement methods are considered. In this chapter, the details of fluorescence based DO sensing, such as different fluorophores and immobilized polymer matrices, are introduced in Section 2.1. An overview of optofluidics based sensing is given in Section 2.2. Section 2.3 discusses different sensitivity enhancement methods used for DO sensors. Section 2.4 describes anti-biofouling techniques in aquatic applications, which are necessary to preserve the sensor surfaces in natural and waste water environment.

2.1 Fluorescence quenching based DO sensing

In Chapter 1, we reviewed the basic principles in fluorescence quenching based DO sensing, including various physical processes occurred in Jablonski diagram and the mathematical expression Stern-Volmer equation. In this section we elaborate on the material and system aspects of this topic, discussing the choices of different fluorophores, polymer matrices and sensing schemes, and the issue of sensing specificity.

2.1.1 Fluorophores

Here an overview is given on the state-of-the-art oxygen indictors available for optical oxygen sensing. Although several absorption based oxygen probes exist [30], we limit our discussion to fluorescence quenching based indicators only. Transition metal polypyridyl complexes, metalloporphyrins, cyclometallated complexes and the indicators not based on heavy atoms are introduced sequentially in this section [30].

Transition metal polypyridyl complexes are probably the earliest widely used family for fluorescence based oxygen sensing [30]. The transition metals typically used are Ru(II) and Os(II) [30]. The complexes in this species are characterized by 1) excitation and emission spectra in the visible range, 2) a large Stokes shift which alleviates the filter requirement, and 3) excellent photostability that implies long device lifetime [30].

Within this group, Ru(II) polypyridyl complexes have been used more frequently due to their higher brightness and longer lifetime [30]. These characteristics are especially obvious in $Ru(dpp)_3^{2+}$ which has a quantum yield of 0.366 and a luminescence lifetime of 6.4 μs [31]. Furthermore, $Ru(dpp)_3^{2+}$ is fairly easy to prepare and commercially available now, the reason why it is so popular as an indicator for oxygen sensors [30]. Yet $Ru(dpp)_3^{2+}$, just like the majority of other Ruthenium (Ru) polypyridyl complexes, has a problem that its luminescence lifetime (several μs) easily results in low system sensitivity if the oxygen diffusivity is not enough [32]. Another disadvantage is that Ru based fluorophores suffer from crosstalk to temperature as their excited triplet states are also subjected to thermal quenching [31]. That being said, other fluorophores that have widely been used in DO sensing include $Ru(bpy)_3^{2+}$, $Ru(dpb)_3^{2+}$, $Ru(phen)_3^{2+}$ and $Ru(5\text{-}odap)_3^{2+}$.

Another large family of oxygen indicators is Pt(II) and Pd(II) porphyrins, which are popular fluorophores in recent years [30]. Comparing with transition metal polypyridyl complexes, their most obvious advantage is the significantly prolonged lifetime ranging from several hundred μs to several ms [21],

which leads to higher oxygen sensitivity according to Stern-Volmer equation. Furthermore, the lifetime could be tuned by altering the heavy atoms in the molecules: Pd based metalloporphyrin complexes enjoy longer lifetime while their Pt analogs possess two to three times higher quantum yield [18]. A general disadvantage of these indicators is their rather low photostability, which makes them more suitable in fluorescence lifetime based sensing than intensity based sensing [33]. The high price and scarcity of platinum and palladium also make these complexes less attractive for cost-efficient and large-scale applications.

PtOEP and PdOEP remain popular indicators in the family thanks to their impressive quantum yield of 0.5 and 0.2 respectively [30]. Their drawback lies in severe photobleaching, which makes them very difficult to play a role in intensity based sensing scheme [33]. PtTFPP thus was proposed as it shows less photodeterioration [33]. Yet the indicators mentioned above absorb only in UV-visible region and therefore suffer from the pitfall that severe autofluorescence are likely to be aroused [33]. Efforts have been made to tune the absorption and emission spectra of the oxygen indicators in this family: PtOEPK/PdOEPK, PtTPTBP/PdTPTBP and PtCP/PdCP have been developed, with the last pair having their absorption/emission in red/near infrared region which resides in the window of human blood absorption [30].

Cyclometallated complexes of Ir(III) and Pt(II) are also used for oxygen sensing [34]. The last decade has seen prosperity in the field of cyclometallated complexes which was driven by the development of OLED (organic light emitting diode) [34]. Some of these dyes were also brought to the area of oxygen sensing. Nevertheless, their pitfalls include lower absorption rate in the visible range compared with transition metal polypyridyl complexes and shorter lifetime with respect to metalloporphyrins [34].

Several substances that are not based on heavy atoms also luminesce and are quenched by oxygen. The thermally activated fluorescence of fullerene C_{70} has been exploited to make an oxygen sensor which was especially suited for ultra-low concentration detection (down to ppb range); such a low detection limit was resulted from the exceptionally long lifetime [35]. The fluorescence spectrum of poly(9,9-dioctylfluorene) (PF8) was observed to be dependent on oxygen concentration: in addition to irreversible oxidation of PF8, reversible fluorescence quenching was measured [36].

In conclusion, when we choose a suitable fluorophore, several criteria are worth considering as below. Absorption and emission spectra are essential when checking whether there are compatible excitation light sources, emission detectors and excitation/emission filters. The absorption coefficient and the quantum yield of the fluorophore determine the brightness of the emitted light; higher brightness can reduce the power consumption of the light source. Luminescence lifetime is proportional to the sensitivity of DO detection, and crosstalk to other parameters has to be taken account when neutralizing interferences and/or creating references [27]. Furthermore, commercial availability (or synthetic easiness) and the financial cost are crucial factors to consider for mass applications [30]. Chemical stability and photostability are important if long operation time of the sensor is desired. Toxicity of the indicator is also of concern for biological and environmental applications.

2.1.2 Immobilized polymer matrices

Polymer matrices are used to encapsulate fluorophores in DO sensors. A number of critical requirements exist for the choice of appropriate polymer. Permeability to oxygen and solubility of fluorophores are the two most essential qualifications [23]. We could first look at oxygen permeability here. Gas permeability in a polymer equals the product of the gas diffusivity and solubility in the material. Oxygen diffusivity is proportional to quenching sensitivity as shown in Stern-Volmer equation; oxygen solubility determines how much oxygen could get in touch with fluorophores. Thus oxygen permeability in the polymer has profound influences on DO sensing performances. At the same time, only when the selected fluorophore

has a good solubility in the polymer matrices, a homogenous sensing film could be formed and function consistently [27]. Non-homogeneity of fluorophores in the film easily results in non-obeisance to Stern-Volmer equation and sensor performance drift along with operation time [27]. As another factor, the mechanical strength of the polymer determines whether any additional substrate is needed to hold the sensor in shape. If the sensing film is patterned on a water channel surface, the adhesion between the polymer matrix and the channel material should be sufficient such that they are not detached or damaged by the channel flow [29]. For biological and environmental applications, the polymer matrices must be biocompatible.

Silicone polymers and organic glassy polymers are the two major classes of polymer matrices people use in optical oxygen sensors. The most widely used silicone as the polymer matrix is poly(dimethylsiloxane), which is also known as PDMS [23]. Enjoying a very impressive oxygen diffusivity ($40 * 10^{-6}$ cm^2/s) which is at least one magnitude larger than that of organic glassy polymers, PDMS lacks mechanical strength in thin films [23]. Nevertheless, it has recently be known that the oxygen solubility of poly(1-trimethylsily-propyne) [poly(TMSP)] is about 5 times larger than that of PDMS and their oxygen diffusivities are similar; poly(TMSP) also provides a tough thin film [37]. Poly(TMSP) film is porous in microscale, indicating that the oxygen could contact with fluorophores in gas phase [38]. Systematic research on poly(TMSP) is still under development currently.

Although organic glassy polymers such as poly(vinyl chloride) (PVC), polystyrene (PS) and poly(methyl methacrylate) (PMMA) have lower permeability, diffusivity and solubility for oxygen than silicone polymers, these materials lend impressive mechanical strength to thin films [23]. To compensate for their drawbacks in oxygen permeability, various plasticizers have been added to the polymers to alter their properties [39]. The most used plasticizers are bis(2-ethylhexyl)adipate (DOA), dioctylphthalate (DOP), and bis(2-ethylhexyl)sebacate (DOS), to name a few [39]. Increasing the plasticizer ratio (sometimes even more than 50%) usually elevates the gas diffusivity in the polymers [39]; as a result the sensitivity and the response speed of the sensors are enhanced. However it must be noted that the plasticizer influence depends on many factors including the preparation steps, the type of the polymers and the interested range of DO sensing; in some cases the addition of plasticizers could reduce sensitivity performances [40].

Good pairs of fluorophores and polymer matrices can assure desired solubility of the fluorophores in the polymer matrices. Typical instances of polymer matrices for fluorophores include: PDMS for Ru(dpp)$_3$, Ru(phen)$_3$ and PtOEP, polystyrene for Ru(dpp)$_3$, PtOEP, PtOEPK and PdOEPK, PVC for Ru(dpp)$_3$, PtOEPK and PdOEPK, and PMMA for PtOEP, PDMA for PtOEPK [27].

2.1.3 Sensing schemes

The process of oxygen quenching in luminescence belongs to collisional quenching, where the quenchers reduce the luminescence intensity and lifetime at the same time. Naturally there are two categories of methods to detect quenching efficiency: one uses emission intensity and the other uses luminescence lifetime. Both categories are discussed in this section.

Emission intensity sensing is far easier than lifetime sensing in terms of operation principles and system setups, so this sensing scheme is mainly targeted for the low-end market which requires low cost and simple configuration [27]. Besides the fluorophores and the polymer matrices, an excitation light source, an optical detector and one or more optical filters are needed in the system. The light source can be either narrow band or wide band, yet an excitation filter is necessary if the excitation band of the light source enters into the emission spectrum of the fluorophore. Once the excitation reaches the fluorophores, emission light is generated and detected by the optical detector in the system. The optical detector can be either wavelength discernible such as spectrometers and hyper-spectral imaging devices, or wavelength indiscernible such as PMTs (photomultiplier tubes), photodiodes and power meters etc [41]. To image the

2D distribution of DO concentration, optical imagers such as CCD and CMOS can be employed [42]. For wavelength indiscernible detectors or imagers, an emission filter is necessary to minimize excitation and environment interferences to the emission intensity. Although intensity based sensing scheme is cost-friendly and simple in setups, it is inherently susceptible to a number of influences, such as fluorophores' photobleaching, absorption and scattering in different samples and excitation power fluctuations, to name a few [27].

A number of strategies have been proposed in order to overcome these influences [43]. One of the most widely-used examples is the ratiometric intensity sensing scheme [44]. In this method, two kinds of fluorophores which have the same excitation band and different emission bands are employed, with one fluorophore oxygen sensitive and the other insensitive. Two emission intensities are detected and compared, and the ratio is indicative of DO concentration [43]. Influences coming from factors such as excitation power fluctuation and absorption/scattering effects in different samples can be circumvented in this method, because the emission intensities from both fluorophores are influenced.

Lifetime-based sensing mechanism is more accurate and immune to photobleaching, but it is also more complicated in both principles and system setups than the intensity-based sensing scheme; thus lifetime-based sensing is mainly targeted for high-end applications that do not require repetitive quantities of the sensors. Lifetime-based sensing could be subdivided into time domain and frequency domain. Typically a sinusoidally modulated excitation is used for frequency domain and a square modulated one is for time domain [21]. The 'pulse-and-gate' technique is often employed in time domain [27], where the optical detector is gated and only opens for several short time intervals in the decay time of the emission light. For single exponential decay, lifetime can be calculated by the ratio of intensities from two gates, and although more gates are also used for accuracy enhancement [27]. In frequency domain sensing, a phase-lag between the emission and excitation sinusoidal waves is measured, which is representative of the fluorescence lifetime [27]. Frequency domain sensing relieves the accuracy of time measurement parts and is better than time domain sensing in the terms of separating long lifetime background noises [21].

2.1.4 Sensing specificity

An oxygen sensing configuration is not only dependent upon the fluorophores, polymer matrices and sensing schemes in use, but only related to any existing inferences to oxygen sensing. Here we discuss the issue of oxygen sensing specificity. For example, many oxygen indicating fluorophores are known to be subject to thermal quenching, so these fluorophores suffer from crosstalk to temperature. This crosstalk can be verified by the emission intensity change with temperature in the absence of oxygen [45]. Besides that, a higher temperature leads to an increased collisional quenching rate between the oxygen molecules and fluorophores, so temperature also influence the system performance in a thermodynamic way [46]. These two effects contribute to a reduced luminescence lifetime and lower emission intensity at elevated temperatures.

Thermal effects on luminescence quenching can be expressed by

$$\tau = \left[k_0 + k_1 \exp\left(-\frac{\Delta E}{R(T+273)} \right) \right]^{-1} \qquad (2\text{-}1)$$

where τ is the fluorophore lifetime, k_0 is temperature-independent decay rate, k_1 a pre-exponential coefficient, ΔE the energy gap between the emitting vibrational level and destination ground levels, R the perfect gas constant, and T the temperature (in ℃) [46]. The temperature crosstalk of DO sensors could be compensated by the measurement from a thermometer [46]. In fact, $Ru(phen)_3$ has been widely used as a temperature sensing fluorophore to work together with another oxygen fluorophore in DO sensing

system [46]. Different models with much greater details were established for temperature compensation, which have been widely employed by most commercial DO sensors [46].

Besides temperature, reports have also shown crosstalk effects to $N_2O/NO/NO_2$ gases [47]. Although the majority of these oxynitrides become nitride ions when dissolved in water, and ions cannot pass the polymer matrices where fluorophores reside, some residual gas molecules could be dissolved in the liquid [47]. In fact, $Ru(bpy)_3$ has been researched to function as an NO_2 gas indicator in the combustion engine: comparable sensitivity level as to oxygen was observed [47]. Further research is needed before we could evaluate their influences in aqueous environments on DO sensors.

In summary, if we know that there are some crosstalk effects in certain DO sensing systems, measures are better to be taken either to fix these factors or neutralize their effects. Take the temperature as an example: a typical method would be the addition of a thermometer in the system, and a model is employed to compensate their effects on DO sensing; as an alternative way, we may create a temperature stable environment to contain the DO sensor, where the model is omitted and higher accuracy can be achieved in this case, at the expense of larger financial cost.

2.2 Optofluidics based sensing

For the sake of cost and size reduction in DO sensors, a sensor structure based on optofluidic platform is considered in this project. We would use the techniques employed in optofluidics to fabricate the device. Therefore the origin of optofluidics would be discussed first; after that, we elaborate on the materials and fabrication aspects of optofluidics based structures.

2.2.1 Background

The term "optofluidics" was created at the beginning of this century to define a research direction that combines microfluidics and optical technology [29]. After that, great prosperity has been seen in the development of this field [29]. The confluence of optical techniques and the strengths of microfluidics gives rise to numerous opportunities.

In the perspective of optical practitioners, microfluidics has certain advantages compared with gas and solid structures. Immiscible fluid-fluid interfaces are smooth, with accuracy much greater than the grinding quality of solid lenses, thus fluidic lenses could be realized and changed in real-time in size, shape and refractive indices [48]. In addition, fluidic diffusion could create a controllable blend of optical properties; for example, a concentration and refractive index gradient could be realized by mixing of two kinds of liquids [49]. Liquid is also comparatively easy to input, move and manipulate, which act as an excellent transport medium of light [50].

On the other hand, optical technology also arms the microfluidics with new weapons to target for even smaller marks and to adjust for new applications. The variety of light-matter interactions is remarkably broad, which not only include fluorescence which we discuss in this work but also have reflection, refraction, elastic scattering, Raman scattering and second harmonic generation [51]. These mechanisms can be employed on a wide range of chemical and biological sensing, and they enjoy fast response and high sensitivity/specificity. Besides, light-matter interactions occur at biological interesting scales, where fluidic control is still possible, so this property gave rise to many new ideas such as fluidic microscope and MOEMS (micro-opto-electro-mechanical-systems) [52]. In the end, light can also manipulate fluidics, which supplements conventional control methods in microfluidic devices [53]. All these characteristics would facilitate further development in the field of optofluidics.

Optofluidic sensing is the use of light-matter interactions to measure substances on optofluidic platforms. It could be divided into two large categories, namely the 'off-chip' and the 'in-chip' approaches. In the 'off-chip' approach, macroscale optical components are still used and introduced into the micro-sensor by optical fibers or waveguides; in the 'on-chip' approach, micro-optical functionalities are all included in the micro-sensor [54]. The 'off-chip' approach remained the mainstream of current research in optofluidic sensing, as it was relatively easier to realize based on the experience of macroscale systems.

There are four kinds of optical detection methods that have been widely used in optofluidic sensing: absorbance, fluorescence, chemiluminescence and surface plasma resonance (SPR) detection [54]. Absorbance is the most widely used method in macro sensing infrastructures, yet there are only a few impressive examples of its application in micro-sensors, mainly because of the difficulty to achieve reliable sensing in reduced areas [55]. In contrast, fluorescence became the most widely used detection in micro-sensors, thanks to its superior sensitivity and specificity in microscale. Fluorophores are often immobilized in polymer matrices, where the excitation light is targeted and emission light is collected [56]. Chemiluminescence is the opposite of photochemical reactions; in a chemiluminescence process, light is produced in a chemical reaction from an excited intermediate, which later breaks down and gives out emission. This method enjoys high sensitivity and simple instrumentation, yet the drawback is the very limited range of chemiluminescent reagents [57]. Unlike the above methods which all employ direct monitoring of light itself, SPR detections often measure the modulation of its properties [58]. Changes in incident angles and refractive indices etc. are monitored in SPR applications and superior sensitivities are realized. When combined with optical processes such as Raman Scattering, SPR techniques, for example surface-enhanced Raman Scattering (SERS), increase their sensitivities by several orders of magnitude in micro-sensors.

2.2.2 PDMS and soft-lithography techniques

Although optical principles vary significantly in optuofluidic sensing applications as we mention above, similar fluidic platforms are shared. Techniques for the design, fabrication and implementation of the fluidic structures are deeply rooted in the field of microfluidics. PDMS is the most commonly used material in microfluidics, and it also maintains its popularity in optofluidics given its superior optical properties [27]. PDMS is optically transparent in the visible and near-infrared range and it provides a very low level of autofluorescence which is comparable to BK-7 glass [29]. The use of PDMS facilitates fast prototyping of optofluidic devices at a greatly reduced cost.

Some basic properties of PDMS are listed here. PDMS is transparent from 240 nm to 1100 nm wavelength, thus capable of using in optical detection in the UV-vis/visible/Near-infrared range [59]. PDMS is electrically insulating with a breakdown voltage of $2 * 10^7$ V/m, which could serve as the substrate for embedded circuits and also allows for intentional breakdown to open connections [59]. It is elastomeric and conforms to surfaces, and thus could be released from molds and reverse from deformation [59]. It is thermally insulating and remains stable up to 300 ℃, so it is safe to serve as the container for room temperature applications [59]. It also has a very low permeability to polar liquids yet a high permeability to gases and nonpolar organic solvents, so it could be used for liquid channels which allow for gas sensing [59]. It is non-toxic and biocompatible, and demonstrates suitability for in-vivo sensors and support materials for cell growth [59].

Another advantage of PDMS lies in its capability of fast prototyping, which enables easy and low cost demonstration of devices and systems. Fabrication of PDMS structures is realized by soft-lithography and these structures are easily integrated with other materials. Soft lithography is the replication of a topographically defined structure on the master (mold) [60]. The master structures are obtained by 3D printing or conventional photolithography where the photoresists such as SU-8 and PMMA turns to

master molds [60]. Liquid PDMS prepolymer is poured into the mold and cured for 1 hour to 24 hours to become solid [60]. The PDMS cube is then peeled off and sealed with other structures to function in microfluidic systems. By exposing the surface of PDMS and the surface of another material to air/oxygen plasma, PDMS structures can be sealed permanently with PDMS, glass, silicon, polystyrene and polyethylene [61]. It could also be reversibly sealed by Van der Waals contact with a wide range of materials [62]. These prototyping processes are all carried out in ambient laboratory conditions and the molds can be used for many times without degradation. Thus soft-lithography techniques enable rapid, simple and cost-friendly fabrication process of PDMS. We would use such materials and techniques in the fabrication of sensors in this project.

2.3 Sensitivity enhancement methods in optical DO sensing

When miniaturized, DO sensors are in demand of sensitivity enhancement methods in order to prevent performance degradation. Various reasons give rise to sensitivity decrease in small and lost-cost fluorescence sensors. For example, reduced power of excitation light leads to a reduced difference of emission light intensities in the absence and presence of dissolved oxygen; yet the use of cost-friendly detector weakens the capability in differentiating emission intensities, which naturally forms a gap. To tackle with this problem and others, several sensitivity enhancement methods have been proposed previously, which we will review here, and we also give some simple ideas which may contribute to sensitivity enhancement.

2.3.1 Total-internal-reflection

Total-internal-reflection (TIR) is a phenomenon that happens when light encounters the interface between two different media and is entirely reflected back into the medium with the larger refractive index. As a method to enhance the sensitivity of DO sensing, TIR is used to bend the excitation light pathway and to excite the fluorophores for multiple times.

In ref [63], D. A. Chang-Yen et al. claimed to use the evanescent part of the excitation light to enhance system sensitivity. Excitation light is confined within a waveguide in TIR mode, and the waveguide's surface was spin-coated with the fluorophores. The emission light was collected at the end of the waveguide where a spectrometer was placed. The authors claimed that comparing with a system using the same dye and a non-evanescent setup, this system was capable of detecting less intensity and achieving one tenth in standard errors, which led to resolution and sensitivity increase of the system. Ref [64] from the same group also used a very similar method to obtain DO sensitivity increase based on waveguide sensors.

As we could see, although fluorescence emission was isotropic [21], in these two works, only the part of emission light that could be TIRed inside the waveguide was collected by the optical detector, so the other part of the emission intensity was wasted. In addition, both of the works failed to provide an optical model to explain how the excitation light travelled inside the waveguide. They even failed to demonstrate whether the excitation light that reached the fluorophores was actually in the evanescent mode: as they used an optically transparent polymer matrix to immobilize fluorophores on the waveguide surface, it was possible that the excitation light traveled through this layer and excited the fluorophores directly. Furthermore, a systematic and convincible experiment is in lack to show that TIR did contribute to the achieved sensitivity gain.

2.3.2 Other methods

Several other methods also exist that can increase the sensitivity of DO sensing. In a work [65], the authors utilized microporous light-scattering support material to make the fluorophores spread out and in-

depth (3D) coated. 3D coating was realized by either casting the fluorophore solution over the membrane or dispensing the fluorophore solution with a pipette. The oxygen sensitive layer was resulted covering a very large surface area with a very small thickness; system sensitivity of DO sensing was thus increased. Although good experimental results were obtained, the authors failed to provide a convincible physical model to explain this phenomenon. Besides, the device-to-device deviation of the performances was conceived to be large and thus this setup was unsuitable for mass production.

There are also several works that focused on silica nanoparticles to enhance system sensitivity. Ref [66] employed oxygen indicators adsorbed in the pores of silica nanoparticles, which were then self-assembled layer-by-layer to form the sensing film. In ref [67], the fluorophores were entrapped in core-shell silica nanoparticles which were then embedded in the polymer matrix. These works took advantage of nanotechnology to increase the surface-to-volume ratio of the fluorophores, enhancing their chances to have contact with the quenchers and upgrading sensitivity. Yet nanotechnology is still under development and is in demand of particular equipment for fabrication; the sensors based on such techniques were also expensive and suffered from repeatability issues, so this method was also unsuitable for large-scale applications.

Inspired by these works, we perceive that, in a DO sensing system, multiple fluorophore films that are placed in parallel in the same excitation light pathway could also be used for sensitivity enhancement. All of the fluorophore films are DO contactable and absorb the excitation light, so the total emission intensity is the sum from all fluorophore films. However, this method suffers from the problem that additional layers of fluorophore films contribute to the financial cost of the system [30].

In summary, we could see that although the research on TIR is insufficient, it still presents the advantages of better controllability, repeatability and less cost compared with other methods. Therefore it is regarded as the best potential method for sensitivity enhancement in this project. A detailed physical model as well as systematic experiments is in demand to fully demonstrate the effectiveness and efficiency. In addition, a better collection of the emission light requires further research, which could make the system touch its full potential.

2.4 Anti-biofouling

In spite of the advantages of PDMS in microfluidic systems we mentioned in Section 2.2, its strong hydrophobicity results in severe biofouling effects in natural and waste water conditions. This problem has become the bottleneck for many PDMS based sensors [20]. With an untreated PDMS surface, microfluidic sensors lost almost all their sensitivities within a day in natural water environments [20]. This rapid loss of sensor performance made all efforts useless for continuous monitoring. Thus the topic of anti-biofouling in PDMS based sensors is of great significance.

Biofouling is the accumulation of organic substances, proteins, microorganisms, plants, algae or animals on a wetted surface [68]. Biofouling reduces the permeability of the film so sensors are greatly influenced. Being common yet complicated, the principles and processes of biofouling have not been fully understood, and the methods to reduce biofouling have been researched for decades [68]. There are a number of good reviews on this topic, such as [68] [69] [70]. Here we briefly discuss different factors that influence protein adsorption rate and several typical methods for anti-biofouling treatments on PDMS.

The protein's adsorption on a surface is determined by the liquid environment, the protein properties and the surface properties [69]. External parameters such as pH, ionic strength, temperature and buffer composition in the liquid influence biofouling process, although these factors are relatively fixed if certain biological or environmental conditions are used or mimicked [69]. For instance, temperature has an effect on both the final states and the processess of protein adsorption [71]. As increased adsorption

rate is expected at a higher diffusion speed of proteins, biofouling increases at elevated temperatures [71]. The concentration of ions in the liquid also influences protein adsorption. A higher ionic strength weakens the lateral electrostatic interactions between different proteins adsorbed on the surface, so a decrease of protein-protein repulsion and an increase in the packing density are expected [72].

The intrinsic properties of the protein also affect its adsorption performance on a given surface. Regarding to their interfacial behavior, proteins can be classified by their relative size, composition and structural stability [69]. Small and rigid proteins are not likely to change their structure upon surface adsorption; in contrast, intermediate sized proteins experience conformational reorientations in surface adherence [69]. As for those proteins with a very high molecular weight, individual parts are separately considered and classified as charged/uncharged, polar/non-polar and hydrophilic/hydrophobic [69].

Important parameters of the surface, such as surface morphology, polarity, surface energy and charge, are also related to the interactions between proteins and surfaces [73]. Take polarity as an example. Proteins tend to adsorb more easily to non-polar surfaces than polar surfaces [73]. It has been postulated that proteins could be destabilized near non-polar surfaces, which leads to increased levels of interactions between different proteins and between proteins and surfaces [74]. This principle basically explains why hydrophobic surfaces adsorb more proteins than their hydrophilic counterparts, and it is also the reason why the biofouling of PDMS looks especially significant.

Given the fact that PDMS is hydrophobic and thus prone to biofouling, three categories of methods have been proposed for anti-biofouling treatments on PDMS, namely surface activation (or oxidation), physical adsorption and covalent modification [69]. Among them the surface activation of PDMS is usually employed together with the other two methods, serving as a preparation step for additional modifications [69]. These treatment methods and their pros and cons are summarized as below.

Both the cleaning and the oxidation of PDMS surface are regarded as surface activation, aiming at the purposes to 1) alter the surface into hydrophilic for promoting liquid filling in microscale channels, 2) facilitate PDMS bonding to other materials and/or 3) add PDMS surface with Si-OH groups for tethering of functional groups in next steps [75]. Commonly used procedures for PDMS surface activation include oxygen or air plasma, UV/ozone and corona discharges [76]. Atomic oxygens are generated in these processes and they damage the backbone of PDMS to form Si-OH surface structures [76]. One of the disadvantages of these physical modifications is that the modified surface of PDMS recovers its hydrophobicity within hours when exposed to air [75]. This is the reason why in plasma based bonding of PDMS it is recommended to contact the two surfaces immediately when air/oxygen plasma finishes.

Physical adsorption of PDMS surface enjoys great advantages of simplicity and efficiency compared with covalent surface modification [77]. Depending on electrostatics or other surface interactions, in this method PDMS surface and an additional thin layer of material are put together without any chemical reactions. A common example is the use of BSA (bovine serum albumin) or milk powder on PDMS [78]. Materials also used in this method include non-ionic surfactants, charged polymers and polyelectrolyte multilayers [79]. However, the likely denaturation of treated surface and the lack of opportunities for further tethering of functional groups limit the range of use in physical adsorption [79].

Compared with physical adsorption, covalent modifications are more widely used for applications that are intended for long-term use and need to endure mechanical, chemical or thermal changes in the environments [80]. Boosting much stronger interactions with the bottom surface, covalent modifications obtain better surface robustness at the cost of complexity, processing time and success rate [80]. Covalent modifications could be subcategorized into self-assembled monolayers (SAM), "grafting-to" coating and "grafting-from" coating methods [81]. SAM is realized by spontaneous tethering of the reactants to the reactive surface. PEG (polyethylene glycol) thin layers are generally applied to PDMS or silicon surface

via SAM [81]. The changes acquired from this method function either as the final functional layer or as an anchor layer for subsequent grafting, which may enjoy even better chemical and mechanical properties. The "graft-to" method tethers end-functional groups directly to the anchor layer on the surface; it suffers from low grafting density and comparatively thinner film due to the hindrance of existing polymers toward new-comers [81]. In order to tackle this problem, "grafting-from" method has been proposed for achieving thicker and denser modification layers. In this method, the polymerization of monomers can only be triggered at certain activated anchors sites on the surface [81]. This method employs continuous activation and deactivation processes of the anchor sites on the surface by repetitive removing and recapturing of the capping agents on the polymer chains. With the fact that activation frequency is fairly the same on different anchor sites, this method can more accurately control the thickness and uniformity of the modification layer and achieve targeted brush density and polydispersity [81].

In conclusion, we reviewed the basic principles of protein biofouling on surfaces, and looked at the major methods for anti-biofouling treatments on PMDS surface in this section. This field is still in rapid development: numerous devices targeted for biological and environmental applications could benefit from future breakthroughs in this area.

Chapter 3   Design and fabrication

The design and fabrication process of a low-cost and miniaturized fluorescence quenching based dissolved oxygen (DO) sensor is demonstrated in this chapter. Choices of materials and the basic design of the sensor structure are introduced in Section 3.1. A feasibility discussion on the use of low-cost optical parts in the system is given in Section 3.2. Section 3.3 presents modeling results on sensitivity enhancement, where we discuss a variety of influences coming from the incident angle of excitation, the optical power meter position and the fluorophore film thickness etc. Section 3.4 lists the detailed steps in the sensor fabrication.

3.1 Basic design of sensor

3.1.1 Choices of fluorophores

The intensity based sensing scheme is selected in this work as the sensing principle for the environmental DO sensor, because of its simple setup and thus friendly cost. The characteristics and advantages of intensity based sensing have been reviewed in Section 2.1.

Fluorophore is one of the major components of the intensity based DO sensor; it will have a big impact on the device sensitivity, lifetime and cost, so it requires a detailed analysis before the sensor design. There are three main criteria to evaluate the fluorophore in this work, namely (i) brightness, (ii) lifetime and (iii) photostability.

The brightness of a fluorophore is defined as the product of its molar extinction coefficient and quantum efficiency [30]. The molar extinction coefficient ε expresses the efficiency of light absorption of particular chemical substance at a particular wavelength which is an intrinsic property of this substance [30]. Quantum efficiency Φ, also known as quantum yield, is the efficiency of the fluorophore in energy transfer from incident excitation to fluorescent emission. The quantum efficiency is defined as the number of emitted photons per absorbed photon. The brightness of individual fluorophore is defined by both extinction coefficient and quantum efficiency. Generally, fluorophore with high extinction coefficient and quantum efficiency can effectively transfer the excitation energy to fluorescence emission. These fluorophores are most suitable in sensor application since the requirements of both light source and the optical detector are low, which alleviate design restrictions and operation burden.

Another criterion for the fluorophore is lifetime, which is the time duration of certain fluorophore to return from the excited state to the ground state [21]. It refers to the time a population of excited fluorophores decay to 1/e of the original amount. Since fluorophore with longer lifetime can induce higher chances for the oxygen molecules to collide and to quench the fluorescence emission, a fluorophore with a long lifetime is thus desired for high sensitivity of the DO sensor.

Photostability is also an intrinsic property of fluorophores and it is defined as the time (seconds) for a fluorophore to reduce its brightness by 50% [27]. For a fluorophore, the loss of part of its emission intensity with time is mainly due to photobleaching, which is the photochemical change of the fluorophore which makes it permanently unable to fluoresce. Such photochemical changes include cleaving of covalent bonds and non-specific reactions between the fluorophore and surrounding molecules [27]. Better photostability of the fluorophores enables a longer operation lifetime of the sensors.

Comparison of Potential Fluorophores

Fluorophores	Molar extinction coefficient ($M^{-1}cm^{-1}$)	Quantum efficiency	Lifetime (µs)
$[Ru(dpp)_3]^{2+}$	29500	0.366	6.40
$[Ru(bpy)_3]^{2+}$	14600	0.089	1.15
$[Ru(phen)_3]^{2+}$	20000	0.019	0.28
$[Ru(dpb)_3]^{2+}$	28000	0.306	1.95
PtTFPP (λ_{abs}=390 nm)	323000	0.088	60
PdTFPP (λ_{abs}=406 nm)	192000	0.21	1650
PdOEPK (λ_{abs}=398 nm)	86200	0.12	60
PdOEPK (λ_{abs}=410 nm)	82600	0.01	455

Table 3.1 Comparison between potential candidates for the fluorophore in DO sensor in this project. Intrinsic properties of the fluorophores included are the molar extinction coefficient, quantum efficiency and lifetime. These three factors determine the DO system sensitivity: the higher the molar extinction coefficient and the quantum efficiency and the longer the lifetime, the better DO sensitivity is. It is also desired that the excitation light for the fluorophore is outside UV-visible range, which is known for autofluorescence excitation in a wide range of materials. Based on all these, $[Ru(dpp)_3]^{2+}$ is chosen as the fluorophore in this project.

In Table 3.1, molar extinction coefficient, quantum efficiency and lifetime of eight frequently used oxygen sensing fluorophores are summarized [30]. These eight fluorophores are well known as being less photobleaching and hence superior photostability. The first four fluorophores in Table 3.1 belong to transition metal polypyridyl complexes. These complexes are the earliest ones that have been used for oxygen sensing and they are still a default choice for intensity based oxygen sensing till now. These fluorophores are characterized by large Stokes' shift (which makes emission filtering easier), excitation and emission spectra in visible wavelengths and good photostability. Among all these fluorophores $[Ru(dpp)_3]^{2+}$ possesses the highest brightness and the longest lifetime.

Other fluorophores in Table 3.1 are metalloporphyrins. One common drawback for most fluorophores (not listed here) in this family is their rather low photostability, such as PtOEP and PdOEP. Thanks to chemical modifications that have successfully improved their photophysical properties, the fluorophores in Table 3.1 enjoy a good photostability, which is comparable to that of transition metal polypyridyl complexes. Metalloporphyrins typically experience a large molar extinction coefficient and an impressively long lifetime. However, the fact that they only absorb in UV-visible region raises the problem that a high level of autofluorescence could be produced in a wide range of materials [82], which we would discuss in Section 3.2. In addition, these fluorophores have a rather low solubility in many polymer matrices, which limits the range of available polymer matrices and negatively influences the consistency of sensor performance.

To summarize, we choose $[Ru(dpp)_3]^{2+}$ in this project for its high brightness, long lifetime and good photostability. Moreover, it is low cost and commercially available which are advantages in practical sensor design applications. The basic properties and fabrication process of Ru(dpp) for use in DO sensor have been addressed in early researches; how the sensitivity of these sensors are still not adequate for environmental DO sensing. Thus this thesis concentrates on the exploration of sensor design for sensitivity enhancement.

3.1.2 Choices of polymer matrices

In conventional intensity based DO sensing, the fluorophores are usually immobilized in certain gas permeable polymer matrix. Ideally, polymer that has high fluorophore solubility and high DO diffusivity is desired to be applied as the polymer matrix for fluorescence quenching based DO sensors [23]. The influences of these two properties to sensitivity can elaborated when analyzing the mathematical expression of the quenching efficiency.

The Stern-Volmer equation is as below,

$$\frac{I}{I_0} = \frac{\tau}{\tau_0} = 1 + k_0\tau_0[O_2] \qquad (3\text{-}1)$$

where I_0 and I are the emission intensities, and τ_0 and τ are the lifetimes without and with oxygen quenchers respectively [23]. Quenching rate constant, k_q, is related to this equation: it could be described by the modified Smoluchowski-Einstein equation as

$$k_q = pk_0 = \frac{4\pi N_A (D_p + D_q)pR}{1000} \qquad (3\text{-}2)$$

where D_f and D_q are the diffusivities of the excited fluorophore and of the quencher in the polymer, p the quenching probability per collision between the fluorophore and the quencher, R the sum of collision radii $(R_f + R_q)$ and N_A is the Avogadro number [23].

Comparison of Potential Immobilized Polymer Matrices

Polymer matrix	Oxygen diffusivity (cm^2/s)	Optical refractive index n
PDMS	$4.0*10^{-5}$	1.41
PS (polystyrene)	$7.4*10^{-10}$	1.58
PVC (polyvinyl chloride)	$1.2*10^{-6}$	1.54
SU-8 photoresist (epoxy based)	$4.9*10^{-8}$	1.82
Poly (1-trimethylsily-1-propyne) (poly(TMSP))	$6.5*10^{-5}$	1.42
PMMA	$1.0*10^{-6}$	1.49
ethylcellulose	$6.39*10^{-7}$	1.47
Teflon	$1.7*10^{-7}$	1.38

Table 3.2 Comparison between potential candidates of immobilized polymer matrices in the DO sensor in this project. Intrinsic properties of the polymer matrices included are oxygen diffusivity and optical refractive index. The oxygen diffusivity of the polymer matrices is proportional to DO system sensitivity according to Smoluchowski-Einstein equation; refractive index is related to the optical model analysis and is listed here as another factor. Easiness and wide choices of anti-biofouling treatments are also considered. Based on all above, PDMS is chosen as the immobilized polymer matrix in this project.

For most polymer matrices, D_f is negligible since it is significantly smaller than D_q. The sensitivity of DO sensor is then directly proportional to the diffusivity of oxygen in the polymer matrix . For the sake of

total-internal-reflection analysis later in this chapter, we also list in Table 3.2 the refractive index of potential candidates of polymer matrices, which affects the light pathways and influence the sensing performance [23].

Table 3.2 shows that PDMS enjoys one of the best oxygen diffusivity among various frequently used polymers. Although poly (1-trimethylsily-1-propyne) contains the highest oxygen diffusivity, it is not commonly used microfluidic devices. In contrast, the application of PDMS in microfluidic aspect is well-studied which is most suitable in designing a microfluidic based DO sensing device. Additionally, PDMS also enjoys a plethora of methods to be anti-biofouling treated as presented in Chapter 2. PDMS is thus regarded the best option for the DO sensor in this project.

3.1.3 Sensor structure

One of the main purposes of this project is to enhance optical sensitivity in fluorescence quenching based DO sensors by modifiying the sensor structure and the system setup. As suggested in Chapter 2, the sensitivity can be achieved by increasing the surface-to-volume ratio of the fluorophore film which can benefit light excitation and oxygen contacting.

Several methods, including total-internal-reflection (TIR), excitation light scattering, nanoparticle fluorophores, and multiple layers of fluorophore films are reviewed in Chapter 2 for sensitivity enhancement. TIR is superior to other methods in the environmental oxygen sensing application due to the following reasons: To begin with, environmental applications require miniaturized sensors which are beneficial to cost reduction. TIR gains performance improvements from sensor structure miniaturization, because the TIRed light is confined to a small space which corresponds to a high excitation efficiency. In contrast, excitation light scattering desires a large sensing area in thin-film format, and the sensitivity degrades with sensor miniaturization. Second, the number of excitation sites in the fluorophore film is directly linked with sensitivity enhancement factor, which is determined by the incident angles of excitation in TIR device. Based on this fact, TIR based device is easily to be massively reproduced with low device-to-device discrepancy. Furthermore, the sensitivity enhancement factor is also tunable since the number of excitation sites in TIR based DO sensors could be tuned by changing the incident angle. The sensitivity enhancement factor of TIR devices can be simply manipulated according to the interested range of DO concentration and the accuracy of the light detector. Additionally, TIR method is low cost since no extra fabrication or sensing components is required , which is a significant advantage when compared with other methods such as multiple layers of fluorophore films and nanoparticles (additional layers of fluorophores and nanoparticle fabrication would contribute significantly to the cost of sensors).

Figure 3.1 illustrates the schematic of the DO sensing system. This microfabricated oxygen sensor is comprised of a glass slide substrate (1 mm thick, 7.4 * 2.5 cm large), spin-coated fluorophore film (1-300 μm thick), PDMS channel (1 mm thick, 1-2 mm wide, 4 cm long) and PDMS water channel cap (3 mm thick) from bottom to top. The water channel length direction is defined as Z axis, as it is the water flow and excitation light propagation direction; X and Y axis are defined according to the right-hand system as shown Figure 3.1. When performing experiments, a 445-450 nm excitation light from the laser diode is first focused by a microscopic objective lens and then encounters the edge of glass slide substrate. The angle between the excitation light direction and the glass substrate bottom surface is defined as the incident angle θ. After entry into the sensor, the excitation light is total internal reflected through the entire fluorophore film, which results in the generation of fluorescence emission. This emission light is generated isotopically and collected by an optical power meter which is placed behind an OD 6 emission filter.

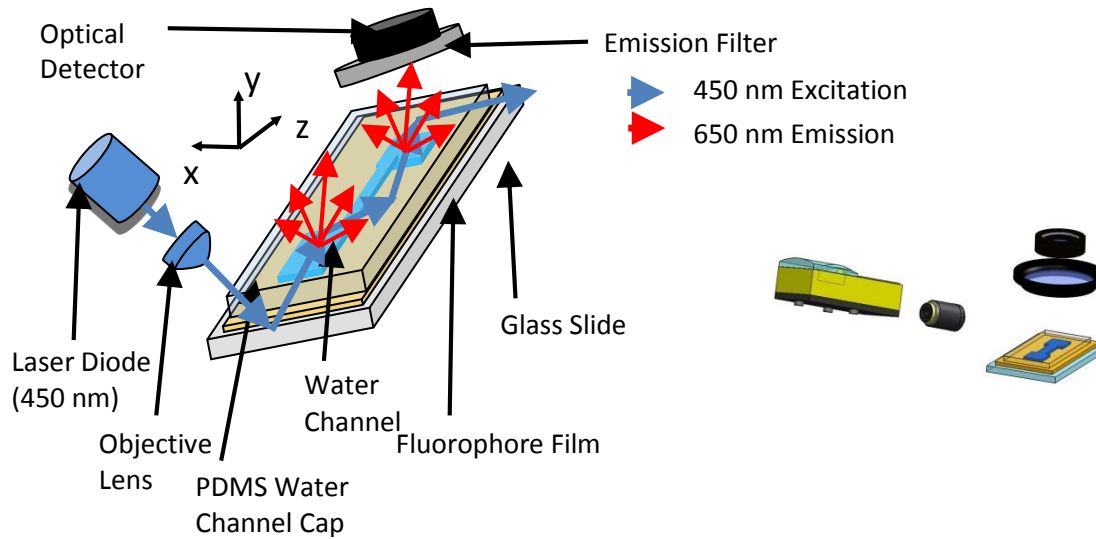**The Schematic of Sensor Design and System Setup**

Figure 3.1 The schematic of sensor design and system setup of fluorescence quenching based dissolved oxygen sensor. The inset is a snap from SolidWorks design. The 4-layer structure of the DO sensor contains, from bottom to top, glass slide substrate (1 mm thick, 7.4 * 2.5 cm large), fluorophore film (1-300 μm thick), water channel (1 mm thick, 1-2 mm wide, 4 cm long) and PDMS water channel cap (3 mm thick). A 445-450 nm excitation light from the laser diode is first focused by a microscopic objective lens and then encounters the edge of glass slide substrate. The angle between the excitation light direction and the glass substrate bottom surface is defined as the incident angle θ. After entry into the sensor, the excitation light goes back and forth through the fluorophore film in the pattern of total-internal-reflection. Emission light is generated isotopically and collected by an optical power meter which is placed behind an OD 6 emission filter. We define the water channel length direction as Z axis, as it is the water flow and excitation light propagation direction; X and Y axis are defined according to the right-hand system.

3.2 System feasibility

3.2.1 Differentiation between excitation and emission

Since the fluorescence emission intensity was conceived to be 10^6 times lower than the excitation intensity [21], an OD 6 emission filter was employed in the system to prevent the excitation light from being detected by the optical detector. A feasibility experiment was conducted to ensure this oxygen sensing setup can differentiate the emission and the excitation light.

For comparison purpose, a purple diode laser (200 mW, 405 nm, Model 10000059, Laserland, Wuhan, China) and a blue diode laser (350 mW, 445-450 nm, Model 20003151, Laserland, Wuhan, China) were used as the excitation light sources without additional excitation filter. Both of them were located in the absorption band of the fluorophore Ru(dpp). 405 nm was known to induce autofluorescence in a wide range of materials. Figure 3.2 was the spectral information of the two diode lasers with spectral resolution 0.3 nm set in the spectrometer. We could estimate that the FWHM for these two diode lasers was both ~2 nm. Figure 3.3 was the absorption and emission spectra of fluorophore $Ru(dpp)_3^{2+}$ from the manufacturer. 445 nm was near the peak of max absorption range of the fluorophore and 405 nm was chosen as a reference here for its autofluorescence excitation: UV-visible range was well-known for its

autofluorescence excitation in many materials including PDMS, which was the basic structure in this sensor.

To analyze the origin of light seen by the optical power meter in sensing setup (Figure 3.1), a setup for the feasibility experiment was designed and the schematic was shown in Figure 3.4. Our purposes were to tell apart the residual excitation light, the Ru fluorophore emission and the autofluorescence that passed the emission filter. When using a spectrometer, instead of a power meter, excitation and fluorophore emission could be told apart by their spectral difference, according to Figure 3.4. To differentiate the emission from the fluorophore Ru(dpp) and the autofluorescence from any other sources in the system, a control experiment was implemented, and the emission intensity from a complete DO sensor and that from the structure without the fluorophores were compared. The OD 6 emission filter was still used in order to mimic the sensing setup. By quantitatively comparing the spectral results in the feasibility experiment, the percentage of pure emission from fluorophore Ru(dpp) over the total intensity seen by the optical detector could be calculated.

Spectral Information of Two Diode Lasers Used (405 nm and 445 nm)
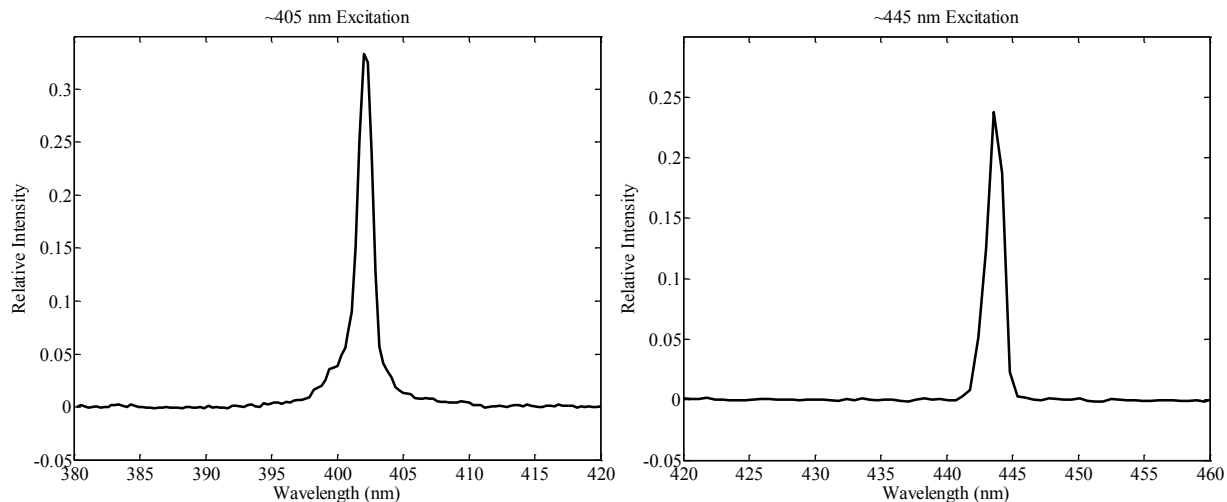

Figure 3.2 Spectral information of the two diode lasers (405 nm and 445 nm). Spectral resolution was set at 0.3 nm in the spectrometer. Both of these diode lasers were located in the absorption band of the fluorophore Ru(dpp) as shown in Figure 3.3. 405 nm was known to induce autofluorescence in a wide range of materials including PDMS. From the figure we can estimate FWHM for these two diode lasers was both ~2 nm.

Absorption and fluorescence emission of Ru(dpp) in toluene solution
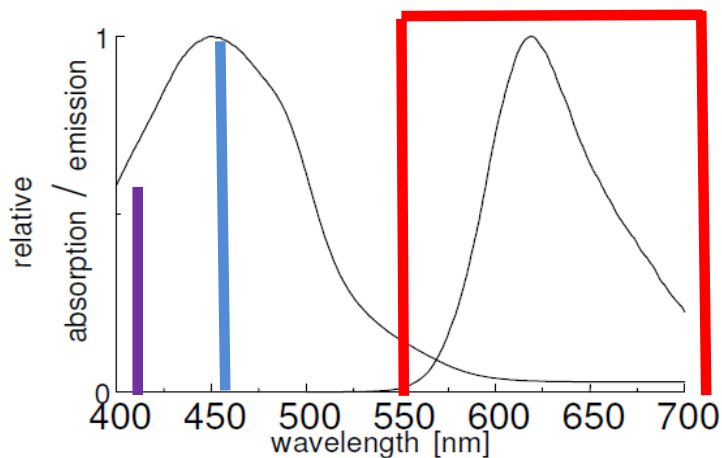
abs. λ_{max} 455 nm, luminescence λ_{max} 613 nm

Figure 3.3 Absorption and fluorescence emission of Ru(dpp) in toluene solution (copyright permission of Sigma AldrichTM). We used alcohol as the solvent instead for better solubility in PDMS, so excitation and emission peak might change. 405 nm and 450 nm diode lasers (depicted in purple and blue lines) were used as the excitation light sources in feasibility experiments and an OD 6 bandpass emission filter with window at 520-700 nm (depicted in red window) was employed to reduce the excitation interference. Spectra information courtesy by
http://www.sigmaaldrich.com/content/dam/sigma-aldrich/docs/Fluka/Datasheet/76886dat.pdf

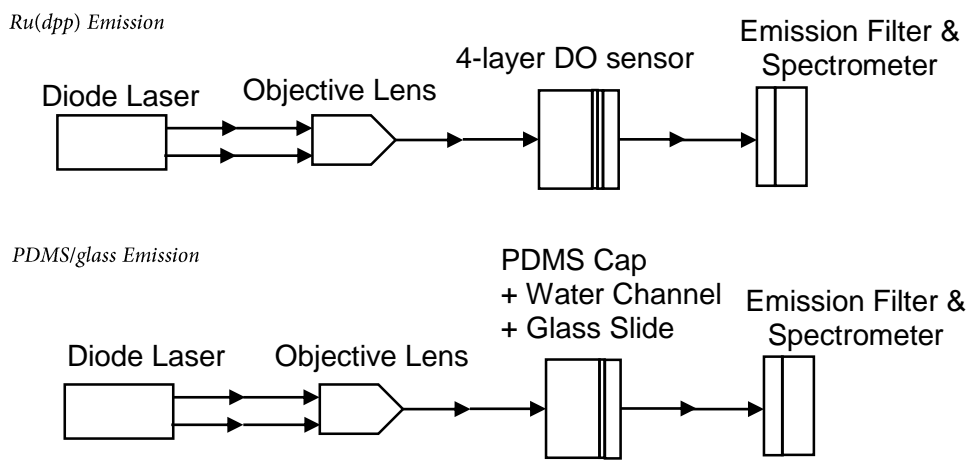**Setup Schematic in Spectral Feasibility Experiment**

Figure 3.4 The schematic of setup in spectral feasibility experiment. The emission filter was placed right before the spectrometer in order to reduce excitation intensity.The emission from the whole sensor was first recorded, in which the 4-layer DO sensor included PDMS cap, water channel, fluorophore Ru(dpp) and glass slide; as a control group, the emission from PDMS cap, water channel and glass slide was then measured. By quantitatively comparing the emission results from the two experiments, pure emission from fluorophore Ru(dpp) could be calculated.

Spectral results from the feasibility experiment were summarized in Figure 3.5. The above two graphs presented the spectrum of the DO sensor at the optical detector under 450 nm and 405 nm excitation respectively; both diode lasers were set at output power 150 mW (optical power outputs were measured by a power meter) and the integration time of spectrometer was 16 s for all of them. The bottom left figure showed the spectrum of the PDMS/water/glass in the control group at the optical detector; it was clear that 405 nm could excite ~3 times more autofluorescence than 450 nm light source. The bottom right graph delineated the spectrum of the DO sensor under 450 nm excitation at 1 s integration time of spectrometer, which was for calibration purpose of the spectrum obtained at 16s integration; good shape and counts-per-second match were observed between this graph and the spectrum under 450 nm at 16 s integration, so we knew that 16 s integration time was suitable for this setup and the first three graphs were not saturated.

The experiment results are presented as the the percentage of pure emission from fluorophore Ru(dpp) over the total intensity detected by the optical detector. The results were calculated based on the spectra data by integration of each peak in different graphs, The calculation results show that 94.5% of the collected energy was from fluorophore emission under 450 nm excitation, with 4.3% from excitation and 0.2% from emission from other sources such as PDMS and glass; while under 405 nm excitation 89.5% of the collected energy was from fluorophore emission, with 8.4% from excitation and 2.1% from emission from other sources. These results demonstrated that using a 450 nm diode laser as the excitation light source was indeed more appropriate for noise reduction in the system. The results also suggest that a low costpower meter and a laser diode are adequate to be applied in the DO sensing setup instead of expensive spectrometers and lasers since 95% of the energy detected by the power meter is contributed from the emission of fluorophores.
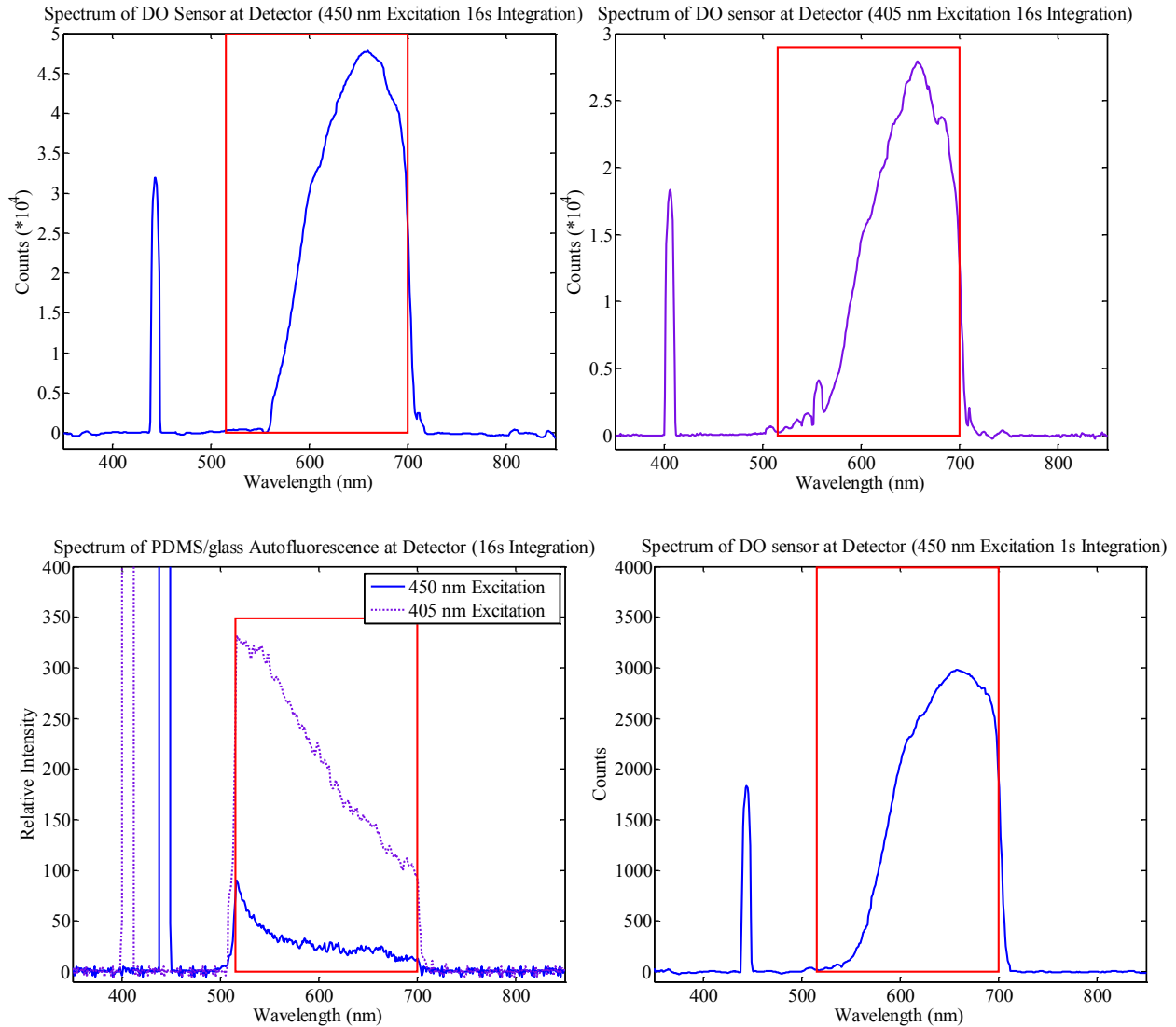
Results Summary of Spectral Analysis

Figure 3.5 Results summary of spectral analysis on DO sensor and PDMS/glass control.The above two graphs presented the spectrum of DO sensor at the optical detector under 450 nm and 405 nm excitation respectively; both diode lasers were set at output power 150 mW (optical power output was also measured by power meter) and the integration time of spectrometer was 16 s for both of them. The bottom left figure showed the spectrum of the PDMS/glass in the control group at the optical detector; it was clear that 405 nm could excite ~3 times more autofluorescence compared with 450 nm light source. The bottom right graph delineated the spectrum of DO sensor under 450 nm excitation at 1 s integration time of spectrometer; good shape and counts-per-second match were observed between this graph and the spectrum under 450 nm at 16 s integration, so we knew that 16 s integration time was suitable for this setup and the first three graphs were not saturated.

3.2.2 Excitation beam profile

In the system setup, a ZEISS A-plan 10X/0.25 Ph1 objective lens in microscopes was added in the light path of excitation, in order to make it focused and fit into the thickness of glass slide in the sensor. In the optical model that would be presented later, the values of the diameter and cone angle of the excitation light will be used. Thus in this part the beam size and the divergence of the excitation will be experimentally measured.
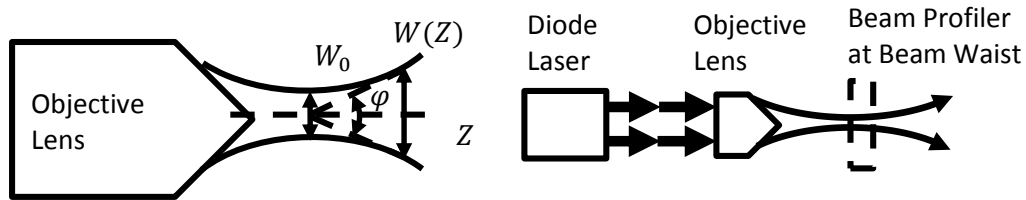
Illustration of Excitation Beam Profile

Figure 3.6 (left) The beam profile of TEM 00 mode light and (right) the schematic of the beam diameter testing setup.The minimum beam diameter W0 was observed in the beam waist and larger beam sizes were observed before and afterward. A 445 ~ 450 nm diode laser and a 10X ZEISS objective lens were placed as the light source and the CCD detector of beam profiler was spatially adjusted to the beam waist of the light.

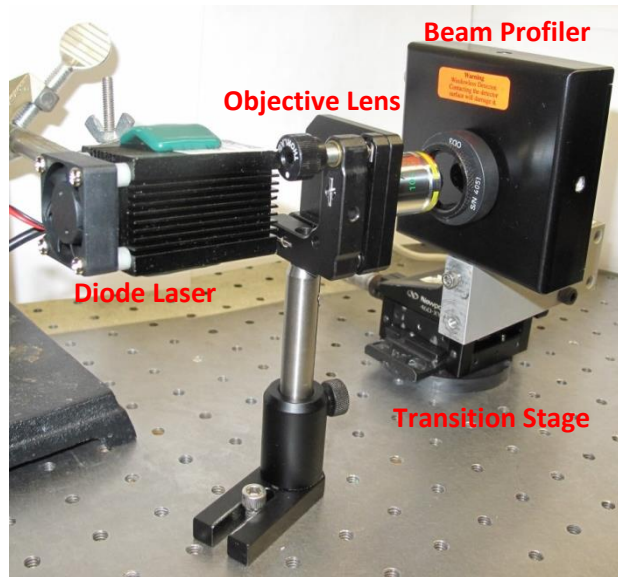**Photograph of Beam Diameter Test Setup**

Figure 3.7 Photograph of the beam diameter testing setup. A 445-450 nm diode laser and a 10X ZEISS objective lens were the light source and the CCD detector of beam profiler was spatially adjusted to the beam waist of excitation light. A two-dimensional transition stage was applied for the beam profiler, which then was enabled to capture larger pictures.

A CCD-based laser beam profiler (Model USB L230 81590126, Spiricon, USA) was used for the characterization of the beam profile. For a Gaussian beam in TEM 00 mode, the beam profile was

illustrated in the left graph of Figure 3.6, with the minimum beam diameter W_0 in beam waist and larger beam sizes before and afterward. A schematic of the beam diameter testing setup was shown in the right graph of Figure 3.6. The 445 ~ 450 nm diode laser and the 10X ZEISS objective lens were the light source and the CCD detector of beam profiler was spatially adjusted to the beam waist of the excitation.
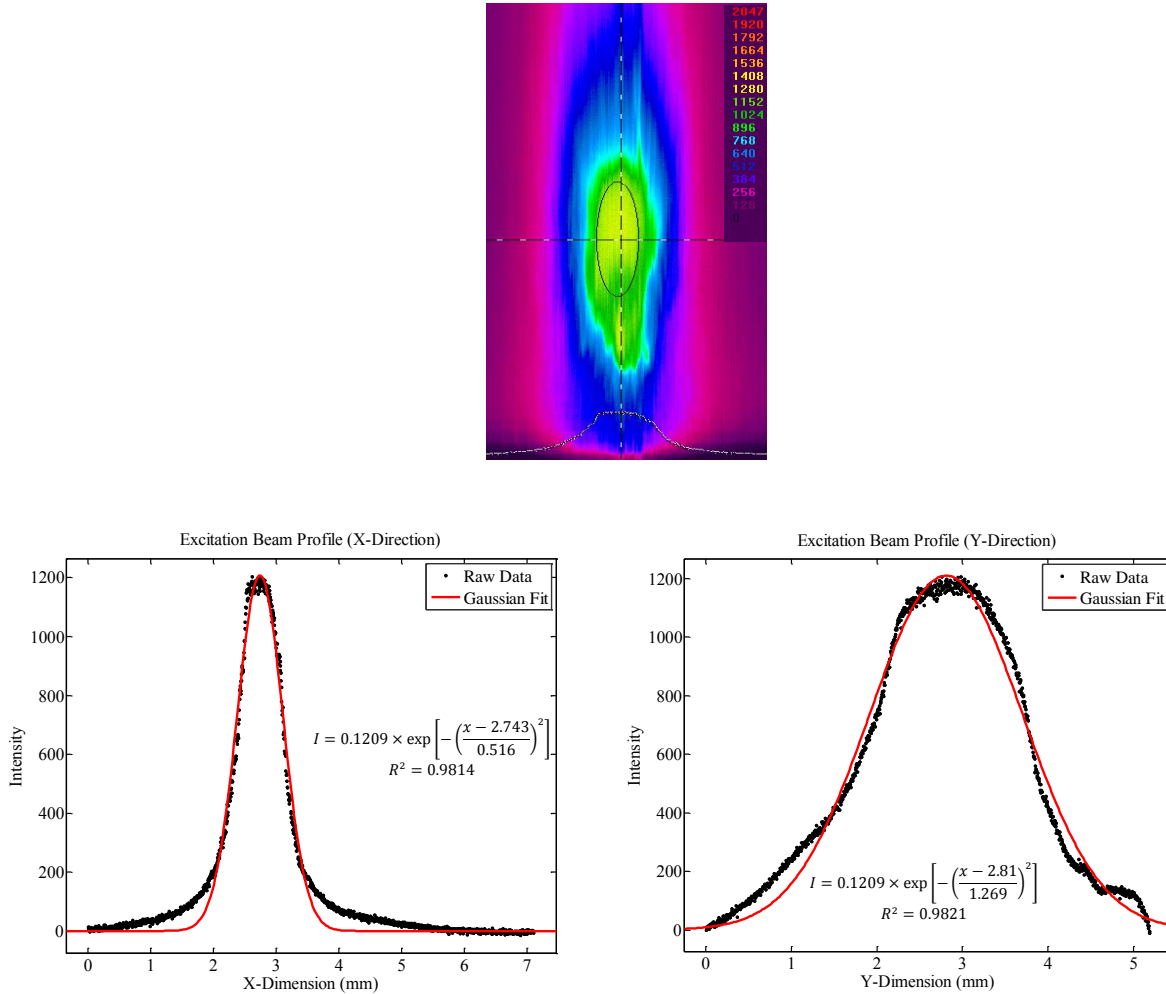
Excitation Beam Contour and Gaussian Fitting

Figure 3.8 (top) The excitation beam contour obtained by the beam profiler and (bottom left and right) excitation beam profiles in X and Y direction respectively. Good correlations with Gaussian distribution were observed in both directions, with R2 larger than 0.98. Y direction had a significantly larger spatial distribution range than X direction, as shown in the fact that the standard deviation for X direction was 0.37 μm and that the standard deviation for Y direction was 0.90 μm. This fact was resulted from the diode laser itself whose output had a very large aspect ratio.

The laser beam profiler was comprised of a Sony™ ICX274 CCD which had 1616*1216 4.40 μm square pixels, so the spatial detection range for this beam profiler was 7.1 * 5.4 mm. This size was enough for the characterization of the beam waist, but was not sufficient for beam divergence measurements that

required beam diameter tests at longer distances. In the light of this, a two-dimensional transition stage was applied for the beam profiler, which was then enabled to capture larger pictures. Figure 3.7 showed the photograph of the setup for beam profile bench testing.

The excitation beam shape was characterized first, in order to verify whether it followed Gaussian distribution. Figure 3.8 showed the contour of the excitation beam intensity as well as Gaussian fitting results in X and Y directions respectively (the coordinate system was the same with the one used in system demonstration in Figure 3.1). Good correlations were observed in both directions with R^2 larger than 0.98, so the assumption of Gaussian beam was confirmed. Y direction had a significantly larger spatial distribution range than X direction, as shown in the fact that the standard deviation for X direction was 0.37 μm and that the standard deviation for Y direction was 0.90 μm. This fact was resulted from the diode laser itself whose output had a very large aspect ratio. The spatial standard deviation for X direction was used in the optical model in Chapter 3.

Table 3.3 was a summary of beam diameter results obtained according to different methods. The major axis (with a larger diameter) referred to Y direction in Figure 3.8 and the minor axis referred to X direction. The data of beam diameters ranged from 0.5 μm to more than 3 μm depending on different definitions for the beam diameter, which are elaborated as below.

The D4σ (4 Sigma) width is the ISO international standard definition of the laser beam diameter. The horizontal and vertical diameters are calculated by 4 times the standard deviation of the spatial distribution σ, respectively. For example in the horizontal direction [83],

$$D4\sigma = 4\sigma = 4\sqrt{\frac{\int_{-\infty}^{\infty}\int_{-\infty}^{\infty} I(x,y)(x-\bar{x})^2 dxdy}{\int_{-\infty}^{\infty}\int_{-\infty}^{\infty} I(x,y)dxdy}}, \qquad (3\text{-}3)$$

where $\bar{x} = \frac{\int_{-\infty}^{\infty}\int_{-\infty}^{\infty} I(x,y)xdxdy}{\int_{-\infty}^{\infty}\int_{-\infty}^{\infty} I(x,y)dxdy}$.

Although suitable for all kinds of beam shapes including both Gaussian beams and non-Gaussian beams, the D4σ (4 Sigma) method is susceptible to background noises. The intensities with greater distance to the beam center contribute more (square relationship) to the calculated diameter result according to above equation, so baseline subtraction is highly recommended in this method. The background noise could be calculated by the average intensities of all pixels without the target light source. After the background is subtracted, the residual intensities in all pixels are used for spatial distribution calculation.

Summary of Beam Diameter Results

Method	Diameter in Major Axis (mm)	Diameter in Minor Axis (mm)
D4σ (4 Sigma)	3.59	1.47
90/10 Knife Edge	3.22	1.34
86.5% of energy	2.76	1.18
1/e² of peak	2.66	1.16
1/e of peak	1.80	0.72
50% of peak	1.21	0.55

Table 3.3 Summary of beam diameter results based on different definitions of beam diameters. The Standard deviations were 0.03 mm for all diameters based on repetitive measurements.

In contrast, 90/10 knife edge width is a more conventional method widely used when 2D optical imagers have not come into place. A schematic demonstrating the conventional test setup is shown in Figure 4.5. A razor moves from one side of the light distribution to the other, recording the intensity ratio at each position over the full intensity without the razor blocking. The width of the beam is defined as the distance between the points of intensity ratios that are 10% and 90% of the full value (whole beam energy). Modern beam profilers with 2D optical imagers still have this method in their software calculations.

The two methods mentioned above are defined in regardless of the beam profile; yet there are other methods which are deeply rooted in the shape of Gaussian distribution. The edges of a beam diameter could be defined either with the irradiance percentage over the peak irradiance of the beam or with the sandwiched energy over the total energy of the beam. As a typical definition, the distance between the positions that have irradiance of $1/e^2$ (0.135) of the max irradiance of the beam is used as the beam diameter. For a Gaussian beam, 86.5% of the total energy is included in this range. Other similar definitions use Full-Width-at-Half-Maximum or $1/e$ of the maximum irradiance to define their edges. Although derived from Gaussian distribution, they are also widely used in various kinds of beam distributions currently.

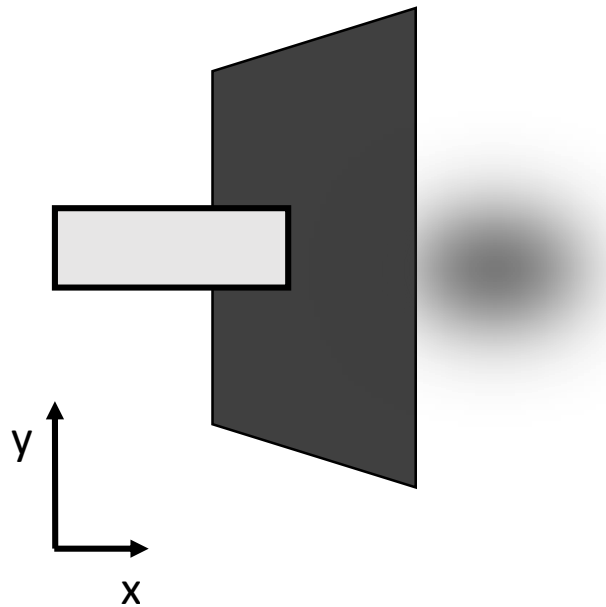**Test Setup for Knife-Edge Method**

Figure 3.9 The schematic of test setup for the knife edge method of beam diameter measurements.

Finishing the discussion on beam diameter, excitation beam divergence is another part of characterization in this section. The total angular spread of a beam is used to represent the divergence, and it is illustrated by the cone angle φ in the schematic of Figure 3.10. Commonly there are two methods that exist for the measurement of the cone angle: one is the far-field method and the other is the focal length method. We used both of them to measure the divergence of excitation as shown below.

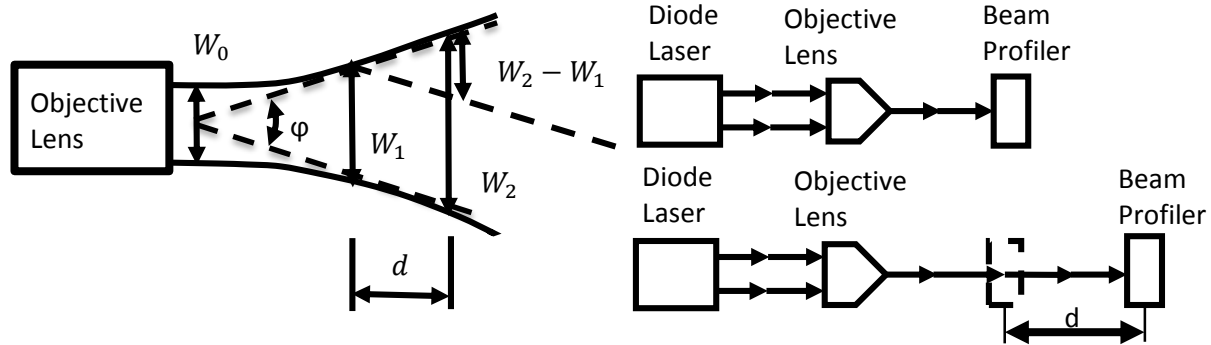## Beam Divergence Definition and Test Setup in the Far-Field Method

Figure 3.10 (left) The schematic of beam divergence definition and (right) the schematic of test setup in the far-field method of beam divergence measurement.

In Figure 3.10, it was seen that the cone angle of a beam was defined by the trendlines of the beam edge in the far-field method. A schematic of the testing setup was created following this idea (shown in Figure 3.10). In the first step the beam profiler was positioned in the beam path to acquire a beam width W_1 ($1/e^2$ of the peak definition was usually applied). It was assumed that this first sample position was the one nearer to the beam waist, and thus a smaller beam width. Next, move the beam profiler a distance further away and a second beam width was acquired as W_2. The divergence (or cone angle) result was described as

$$divergence = 2 \times tan^{-1}\left(\frac{w_2 - w_1}{2 \times d}\right) \qquad (3\text{-}4)$$

where W_1 was the beam width at the first location, W_2 was the beam width at the second location and d was the separation distance between the two sample positions. The results obtained in five experiments using different separation distances in the far-field method were shown in Table 3.4. According to statistical analysis, the cone angle of the excitation beam in the far-field method was $21.02° \pm 0.18°$.

Results Summary of Cone Angle Measurement in the Far-Field Method

Test No.	W_1 (cm)	W_2 (cm)	d (cm)	Cone angle (°)
1	1.105	2.041	2.54	20.89
2	1.105	3.005	5.08	21.18
3	1.105	3.905	7.62	20.82
4	1.105	4.913	10.16	21.23
5	1.105	5.806	12.70	20.97

Table 3.4 Results summary of cone angle measurement in the far-field method. Different separation distances were used in these measurements. According to statistical analysis, the cone angle of the excitation beam in the far-field method was $21.02° \pm 0.18°$.

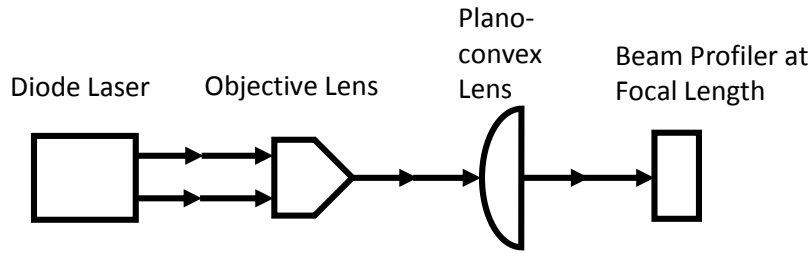**Test Setup in Focal Length Method of Beam Divergence Measurement**

Figure 3.11 The schematic of test setup in focal length method of beam divergence measurement. The use of a focusing optic, either reflective or refractive, was required in this method to transfer the information in the far field into the focal plane of the focusing optic. A plano-convex lens was employed here for aberration minimization.

Another method in beam divergence measurements was the focal length method. The use of a focusing optic, either reflective or refractive, was required in this method to transfer the information in the far field into the focal plane of the focusing optic. Thanks to the principle that the information on the focal plane could be regarded as a Fourier transform of the beam at infinite distance, this method took the ratio between the spot size at the focal plane and the focal distance of the optic as a function of beam divergence [84]. A plano-convex lens was employed here for aberration minimization and the setup was shown in Figure 4.7. In order to miniaturize diffraction effects, a large enough lens in diameter was required for this task. The divergence result could be described as

$$divergence = tan^{-1}\left(\frac{w_f}{f}\right) \qquad (3\text{-}5)$$

where W_f was the beam diameter at the focal plane of the optic and f was the focal length of the optic. The results we obtained in six experiments using different focusing optics were shown in Table 3.5. According to a statistical analysis, the cone angle of excitation beam in the focal length method was $20.9° \pm 0.3°$, which corresponded to the result $21.02° \pm 0.18°$ in the far-field method. The experimental result of cone angle was aligning with theoretical value, which was calculated by the numerical aperture (NA) of the objective lens.

Results Summary of Cone Angle Measurement in Focal Length Method

Test No.	Focal length (cm)	Spot size (cm)	Cone angle (°)
1	75.0	28.505	20.81
2	50.0	18.903	20.71
3	40.0	15.459	21.13
4	30.0	11.234	20.53
5	20.0	7.577	20.75
6	15.0	5.827	21.23

Table 3.5 Results summary of cone angle measurement in focal length method. Plano-convex lenses were employed here for aberration minimization. Different focal lengths of the focusing optics were used in the measurement. According to a statistical analysis, the cone angle of excitation beam in the focal length method was 20.9°±0.3°, which corresponded to the result 21.02°±0.18°in the far-field method. The experimental result of cone angle was aligning with theoretical value, which was calculated by the numerical aperture (NA) of the objective lens.

3.3 Model on system performance

In this section an optical analysis was focused based upon the sensor structure that we proposed in Section 3.1. A variety of factors, including excitation incident angles, sensor structure dimensions and optical parts positions, which can influence DO sensitivity would be discussed in detail. Sensitivity enhancement efficiency of the TIRed excitation light is concentrated throughout the discussion. Two of the essential optical principles involved in this section are Fresnel's Law and Beer-Lambert Law, which are first briefly introduced below.

Fresnel's Law describes the behavior of light when moving between media of different refractive indices. When light enters from the first medium (refractive index n_1) into a second medium (refractive index n_2), both reflection and refraction occur. Fresnel's equation describes the distribution of light reflection and transmission, which are dependent upon n_1, n_2, the incident angle and the polarization of incident light. In the equations below, the angles that the incident, reflective and refractive light rays make to the normal of the interface are depicted as θ_i, θ_r and θ_t respectively. The relationships between these angles are given by

$$\theta_i = \theta_r \qquad (3\text{-}6)$$

and

$$\frac{\sin \theta_i}{\sin \theta_t} = \frac{n_2}{n_1} \qquad (3\text{-}7)$$

If we define Reflectance R as the fraction of the incident power that is reflected back and Transmittance T as the fraction of the incident power that is transmitted through the interface, the reflectance of s-polarized incident light is

$$R_s = \left| \frac{n_1 \cos \theta_i - n_2 \cos \theta_t}{n_1 \cos \theta_i + n_2 \cos \theta_t} \right|^2 = \left| \frac{n_1 \cos \theta_i - n_2 \sqrt{1 - \left(\frac{n_1}{n_2} \sin \theta_i\right)^2}}{n_1 \cos \theta_i + n_2 \sqrt{1 - \left(\frac{n_1}{n_2} \sin \theta_i\right)^2}} \right|^2 \qquad (3\text{-}8)$$

and the reflectance of p-polarized incident light is

$$R_p = \left| \frac{n_1 \cos \theta_t - n_2 \cos \theta_i}{n_1 \cos \theta_t + n_2 \cos \theta_i} \right|^2 = \left| \frac{n_1 \sqrt{1 - \left(\frac{n_1}{n_2} \sin \theta_i\right)^2} - n_2 \cos \theta_i}{n_1 \sqrt{1 - \left(\frac{n_1}{n_2} \sin \theta_i\right)^2} + n_2 \cos \theta_i} \right|^2 \qquad (3\text{-}9)$$

Ts and Tp are given by, as a consequence of energy conservation,

$$T_s = 1 - R_s \qquad (3\text{-}10)$$

and

$$T_p = 1 - R_p \qquad (3\text{-}11)$$

In our cases, as a diode laser is employed as the light source, we assume that the incident light is unpolarized (which contains an equal mix of s- and p- polarizations); therefore the reflectance is given by

$$R = \frac{R_s + R_p}{2} \qquad (3\text{-}12)$$

Total-internal-reflection (TIR) is a special case under Fresnel's Law, when the incident light comes from the medium with a larger refractive index and the incident angle is greater than 'critical angle' with respect to the normal of the interface. In such case the wave cannot pass through the interface and is entirely reflected. From Fresnel's equation we can calculate the critical angle by

$$\theta_c = \theta_i = \arcsin\left(\frac{n_2}{n_1}\right) \qquad (3\text{-}13)$$

An important effect of total-internal-reflection is the appearance of 'evanescent wave' in the medium with smaller refractive index (near the interface of the two media). The evanescent wave travels along the boundary and exponentially decays with increasing distance normal to the interface. The intensity of the evanescent wave could be expressed as a function of the perpendicular distance z to the interface [85]:

$$I(z) = I(0)e^{-z/d} \qquad (3\text{-}14)$$

where

$$d = \frac{\lambda_0}{4\pi}(n_2^2 \sin^2\theta_i - n_1^2)^{-1/2} \qquad (3\text{-}15)$$

λ_0 is the wavelength of the incident light in vacuum and the penetration depth d decreases with increasing θ_i. Except for $\theta_i \rightarrow \theta_c$ where $d \rightarrow \infty$, d is in the same order of λ_0.

Beer-Lambert Law depicts the effects of light absorbing materials upon moving light and relates the attenuation of light with properties of the material. The law states that the transmission T of light through a substance is given by

$$T = \frac{I}{I_0} = e^{-\varepsilon cl} \qquad (3\text{-}16)$$

where I_0 and I are the intensities of the incident light and of the transmitted light respectively, ε is the absorptivity of the light attenuator, c is the concentration of the light attenuator in the material and l is the distance that light travels in the material. Absorbance A is defined as

$$A = -\ln\left(\frac{I}{I_0}\right) \qquad (3\text{-}17)$$

Finishing the discussion on optical principles, we can focus on our sensor structure now. We can see from above equations that TIR, which is the principle of sensitivity enhancement in the DO sensor, is heavily dependent on the incident angle of excitation. By defining the coordinates and the incident angle in the system setup, a cross-section picture of the sensor structure is shown in Figure 3.6, which serves as a basis for the discussion of optical model hereafter.

As in Figure 3.12, the optical analysis model of the DO sensor is simplified into a 4-layer structure, containing, from bottom to top, BK-7 glass slide (n=1.52), fluorophore film (n=1.42), water (n=1.33) and PDMS water channel cap (n=1.41). All refractive indices were measured by ellipsometry. The excitation light is incident on the lateral side of the glass slide, where the incident angle θ is defined as the direction of the incident light making to the normal of the lateral side of the glass. As the default dimensions in the optical model, the thicknesses of the four layers (glass, fluorophore film, water and PDMS cap) are set to be 1 mm, 10 μm, 1 mm and 3 mm respectively, unless otherwise mentioned. The left edge of the optical detector is assumed to be coincident with the start of the water channel in default setting; the 'detection length', which is the dimension (in Z axis in Figure 3.12) the optical detector covers (inside which the

emission light could be collected), is assumed to be 2.54 cm (1 inch), as is the diameter of a typical circular filter.

According to Fresnel's Law, when the incident excitation light arrives at the lateral side of the glass slide, both reflection and refraction may occur as shown in Figure 3.13. Following the same principle, when excitation light rays enter into the 4-layer structure and encounter interfaces between different media, they split into two rays as reflection and refraction respectively. A number of reflection and refraction rays are illustrated in Figure 3.13, which serve as an example of the rays considered in the optical model. Due to the fact that both reflection and refraction rays cycle after first several rounds, their total intensities, as well as influences on DO sensitivity, could be modeled as a geometric sequence.

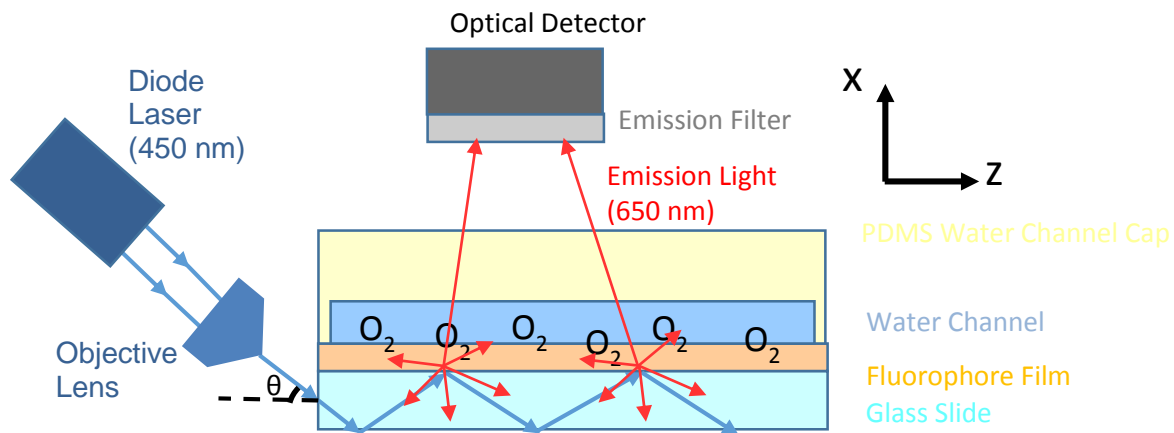**Cross-Section Vision of the Sensing System Setup**

Figure 3.12 Cross-section vision of the setup of DO sensing system. This picture serves as a basis for future discussion on the sensitivity enhancement efficiency of TIR under different scenarios. The 4-layer structure of the DO sensor contains, from bottom to top, glass slide substrate (1 mm thick), fluorophore film (10 μm thick), water in test (1 mm thick) and PDMS water channel cap (3 mm thick). Excitation light is total-internal-reflected inside the glass slide (when θ is smaller than 34.5 °), the bi-layer structure of fluorophore film and glass slide (when θ is between 34.5 °and 47.5 °), or the whole 4-layer structure (when θ is bigger than 47.5°).

The Schematic of Excitation Light Pathways Considered in the Model
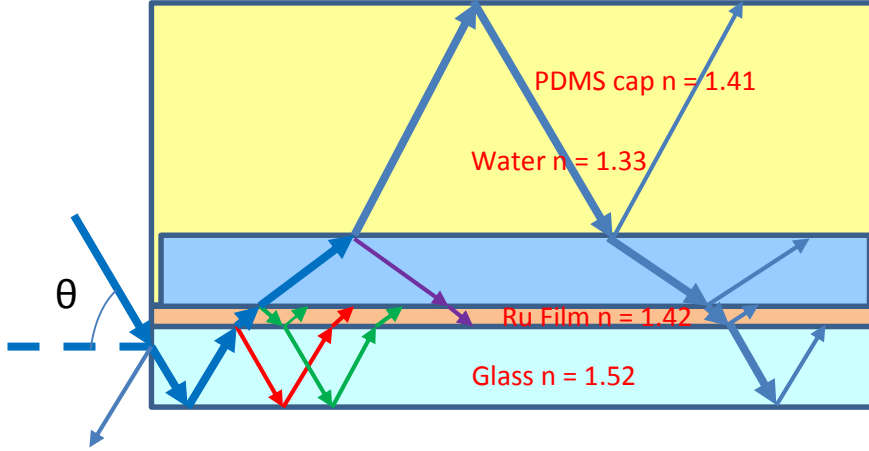

Figure 3.13 The schematic of excitation light pathways considered in the optical model. The refractive indices shown in the picture are chosen at the wavelength of excitation 450 nm and measured by ellipsometry. According to Fresnel's Law, when the excitation light encounters an interface, both reflection and refraction occurs, so one ray split into two after passing of each interface. Because of the fact that the refraction would dominate (>90% intensity fraction) when TIR is not met, we name this ray as the main ray while the reflective one as the minor ray. Since both major and minor rays cycle after the first several rounds, their total intensities and influences could be modeled as a geometric sequence.

Based on the calculation, no matter how the incident angle θ changes from 0 to 90 degree, the excitation light rays are always trapped inside the 4-layer structure because the possible rays always meet the TIR criterion at both the bottom glass/air interface and the top PDMS/air interface. Furthermore, calculation shows that the excitation light is total-internal-reflected inside the glass slide when the incident angle θ is below 34.5 °(Figure 3.14 Type 1), or total-internal-reflected inside glass and fluorophore film when the incident angle θ is between 34.5 °and 47.5 °(Figure 3.14 Type 2), or total-internal-reflected inside the 4-layer structure when the incident angle θ is larger than 47.5 °(Figure 3.14 Type 3). In Type 1 only the evanescent part of the excitation light is in contact with the fluorophores, while in type 2 and type 3, the excitation light directly cross the fluorophore film. Equations that describe how the relative sensitivity is calculated are shown as below.

Type 1

$$F = \emptyset \sum_i \int I_i(x)\, dx \qquad\qquad (3\text{-}18)$$

where $\qquad I_i(x) = I_i(0) e^{-\frac{x}{di}} \qquad di = \frac{\lambda_0}{4\pi}(n_{Ru}^2 \sin^2 \theta_i - n_{glass}^2)^{-1/2}$ (3-19)

Type 2 and Type 3

$$F = \emptyset \sum_i I_i(1 - e^{-\varepsilon c l i}) \qquad\qquad (3\text{-}20)$$

where *F* represents the fluorescence emission intensity, $\emptyset$ represents the quantum efficiency of fluorophores, I_i represents the excitation light intensity at certain excitation site on the fluorophore film and i represents the ith number of excitation site. A Matlab model is generated according to these equations and the influences coming from different factors in the system setup are analyzed, as shown later in this section.

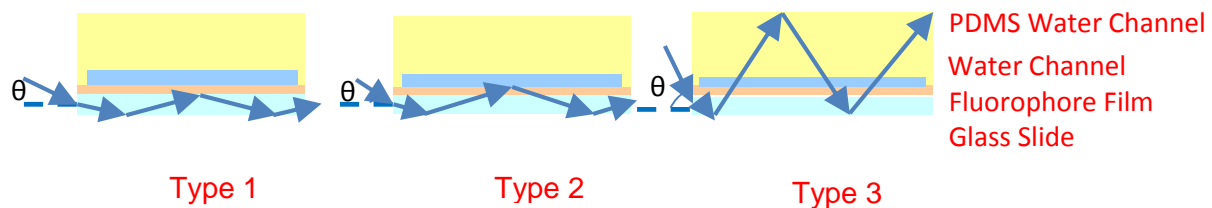**Three Scenarios of Total-Internal-Reflection Patterns in Sensor**

Figure 3.13 Three scenarios of total-internal-reflection patterns of the excitation light inside the sensor structure. In Type 1, the excitation is TIRed inside the glass slide when incident angle θ is smaller than 34.5 °; in Type 2, the excitation is TIRed inside glass slide and fluorophore film when θ is between 34.5 ° and 47.5 °; in Type 3, the excitation is TIRed inside the whole 4-layer structure when θ is between 47.5 ° and 90 °. Based on the calculation, no matter how the incident angle θ changes from 0 to 90 degree, the excitation light rays are always trapped inside the 4-layer structure, because the light rays meet the TIR criterion at both the bottom glass/air interface and the top PDMS/air interface. The refractive indices used for the 4 layers, from bottom to up, are 1.52, 1.42, 1.33, 1.41 respectively at 445-450 nm.

- **Incident and cone angle of excitation**

In the discussion before, the incident angle of excitation was mentioned as a factor that directly influenced the number of excitation sites on the fluorophore layer; it thus affected the relative sensitivity of DO sensing. Cone angle of excitation also disturbed the sensitivity, since a larger cone angle of excitation could be interpreted as a boarder averaging effect of a bunch of excitation rays at continuous incident angles. In the system setup, the incident angle was defined as the angle between the sensor plane and the objective lens, and the cone angle of excitation was determined by the numerical aperture of the objective lens. The cone angle was calculated by the arcsine function of the numerical aperture over the refractive index of air (which we used as the medium). The excitation light into the sensor was verified to be a Gaussian beam with a spatial standard deviation 0.37 mm so this number was also used in the optical model for sensitivity analysis. Results in the modeling of different incident and cone angles of excitation were shown in Figure 3.15.

According to the results in Figure 3.15, DO relative sensitivity was first increasing before 36 ° and then decreasing with the incident angle of the excitation. The numerical calculation also showed that near 36 ° the structure could absorb over 99% of incident excitation intensity, where the excitation light was TIRed inside the glass slide and the fluorophore layer. A schematic showing how the excitation and emission light behaved at 36 ° was shown in Figure 3.16. The colorbars were in logarithmic scale. The orange boxes indicated the fluorophore film (thickened 33 times for illustration purpose) and the white boxes indicated the glass slide. The excitation intensity was observed to decrease about a magnitude at each

excitation site on the fluorophore film, so only the first very few sites contributed meaningfully to the overall emission intensity.

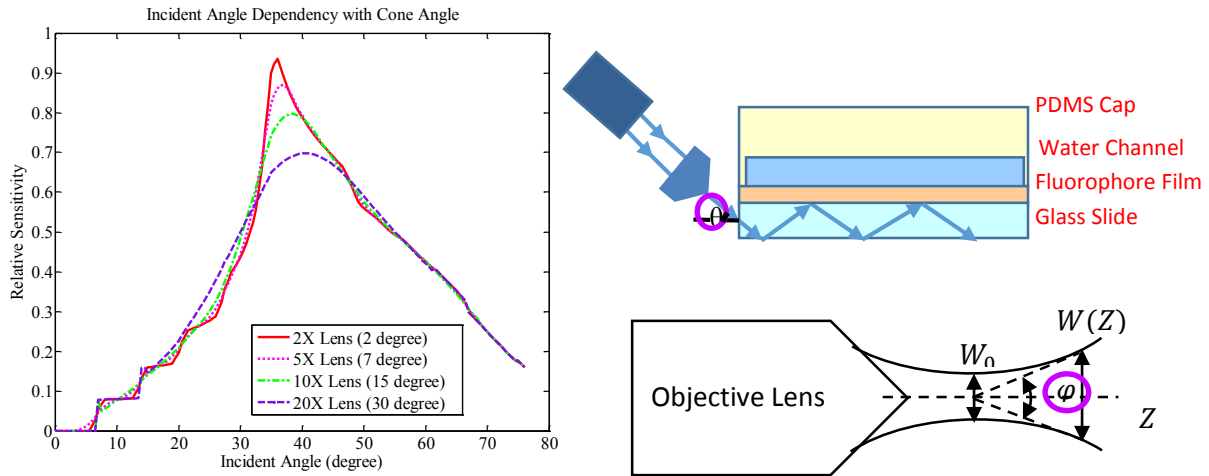**Model Results of Incident and Cone Angle of Excitation**

Figure 3.14 (left) Model results of the influences on relative system sensitivity from the incident and cone angles of excitation light and (right) schematics of how the incident and cone angles were defined in the system setup. θ was the incident angle of the excitation and φ was the cone angle of the excitation light coming from the objective lens into the sensor. As shown in the left graph, system relative sensitivity was first increasing before 36 °and then decreasing with the incident angle of excitation; the larger the cone angle of excitation, the lower the max value of the sensitivity and the wider the tolerance range of the incident angles for a good sensitivity was.

As also shown in Figure 3.15, when a Gaussian excitation beam with a larger cone angle was employed, the max value of DO sensitivity would be lowered. This was because that near 36 °incident angle, there was a larger proportion of rays that entered the sensor with an actual bigger or smaller incident angles. The widening of the beam angles led to a smoothing of the sensitivity peak, resulting in a lower value for the max sensitivity. Yet it is also observed in the graph that the acceptable range of the incident angle for good sensitivity was increased, when using a larger cone angle. This effect of tolerance widening alleviated the demand on adjustment accuracy of the incident angle. A balance needed to be struck to maintain the highest sensitivity and acceptable incident angle tolerance.

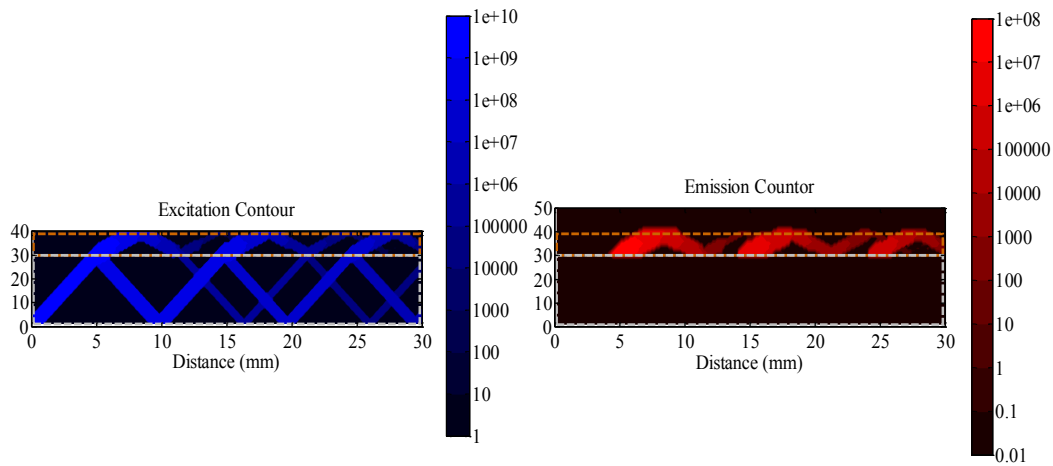**Excitation and Emission Energy Distributions**

*Figure 3.15 Excitation (left) and emission (right) intensity distributions inside the sensor at 36 °
incident angle of excitation. The orange boxes indicated the fluorophore film (thickened 33 times for
illustration purpose) and the white boxes indicated the glass slide. The excitation was total-internal-
reflected inside the glass slide and the fluorophore film under this incident angle. Emission intensity
reached the highest around this incident angle and the excitation absorption efficiency exceeded
99%. The numbers in X-axis represented the distance along water channel length in mm; Y-axis was
just for illustration purpose.*

- **Detection length of emission**

In above discussion of the incident and cone angle of excitation light, 2.54 cm (1 inch) was assigned to be
the detectable length of emission light counting from the very beginning of the water channel, for 1 inch
was the typical diameter of commercially available emission filters. From the fact that over 99% of the
excitation energy could be absorbed at 36 °incident angle, it is presumed that this detection length was
long enough if the highest DO sensitivity is interested. Yet if the size of the emission filter could be
customized in mass production case, the diameter of the filter might be shortened if such detection
dimension was not necessary. The size reduction of the filter can possibly reduce the cost of filtering
materials in the systems. An optical model about the influences of detection lengths on the sensitivity was
thus highly desired and conducted here.

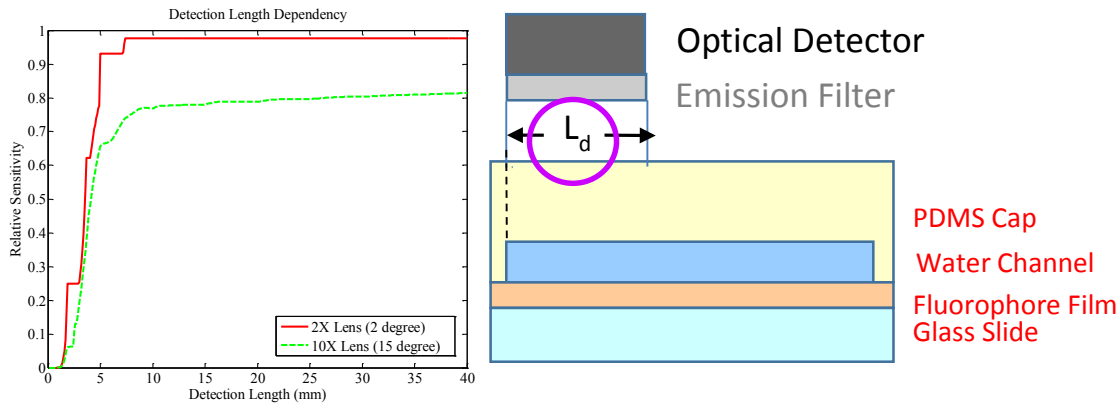**Model Results on Detection Lengths of Emission Light**

Figure 3.16 (left) Model results of relative sensitivity on different detection lengths of the emission light and (right) the schematic of how the detection length was measured in the setup. The beginning of optical detection range was assumed to start from the beginning of the water channel. As shown in the left graph, relative sensitivity increased with longer detection lengths and 7 mm length was enough for an adequate collection of emission. Because 1 inch (25.4 mm) emission filter is used in sensing setup, no additional convex lens was needed for emission collection.

The influences of the detection lengths upon the max DO sensitivity was first studied, which were shown in Figure 3.17. Detection lengths from 0 to 4 cm were examined, which covered the whole length of the water channel. All detection lengths were defined from the very beginning of the water channel as we stated before. The relative sensitivity increased with longer detection lengths obviously. Both of the beams from 2X and 10X objective lenses reached a flat sensitivity plateau after 5~7 mm of detection length, which corresponded to the position of the first excitation site at 36 °incident angle (see Figure 3.16). This fact proved that at 36 °incident angle, one excitation site was necessary for max sensitivity. It was also worth noting that the sensitivity obtained before 5 mm of detection length was resulted from incident angles scenarios larger than 36 °, where one or more excitation sites could be enabled at shorter detection lengths. In summary, a 7 mm long emission filter was enough for the collection of emission light in the sensors.

In addition to above analysis, the influences of detection lengths upon the range of the incident angle for good sensitivity was investigated, and the results were shown in Figure 3.18. Detection lengths of 5, 10, 20, 30, 40 mm were examined under a collimated excitation beam. Max point of sensitivity was unchanged when the detection length was greater than or equal to 10 mm, while the angle tolerance for this max point was smaller when reducing the detection length. We observed that Type 1 scenario (in Figure 3.8) with the incident angle less than 34.5 °(where excitation light was TIRed inside glass slide) were more affected by the decrease of detection lengths: the acceptable incident angle range was narrowed on the left side in detection length reduction. Based on this analysis, it was also necessary to take into account the acceptable incident angle range when reducing the filter size. An optimum detection length in such a sensor system can only be determined when a balance was struck between the cost of filtering material and the sensor performance. In the following parrts the detection length of the emission light is still assumed to be 2.54 cm (1 inch).

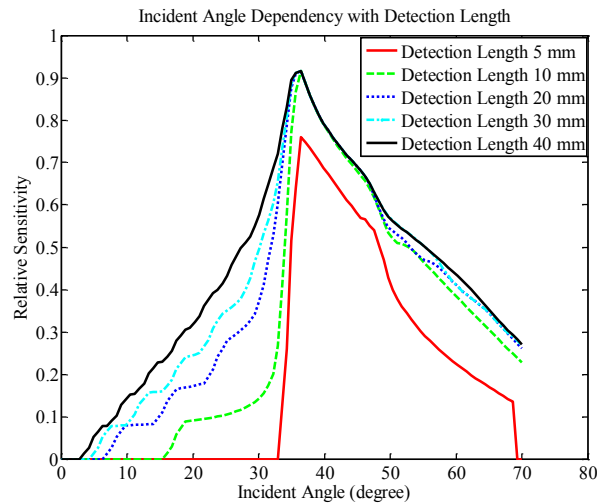**Model Results on Incident Angles Using Different Detection Lengths**

Figure 3.17 Model results of relative sensitivity on incident angles using different detection lengths. Max point of sensitivity was unchanged when detection length was greater than or equal to 10 mm, while the angle tolerance for this max point was smaller when reducing detection lengths. A balance needed to be struck between shorter detection lengths and good sensor performance.

- **Detector position**

In last part the detection length of emission light was discussed, which was defined from the very beginning of the water channel in DO sensor. In sensing setup the detector position could also be changed, which was defined here by the distance between the start of detection range and the beginning of the water channel (minus for left displacement of detector and plus for right displacement of detector). How this detector position could influence the sensitivity is related to the placement accuracy requirements of the detector. An optical model on the detection position was thus proposed here.

Model results on detector position for detection lengths 25.4 mm and 10 mm were shown respectively in Figure 3.19, together with a schematic to show how the detector position was defined in the sensor setup. As shown in the model results, the relative sensitivity remained unchanged when the detector position was in the range of -10 ~5 mm for detection length 25.4 mm, so the tolerance for detector position was 15 mm; in the same way the tolerance was 7 mm for detection length 10 mm. Thus a conclusion could be drawn that a fairly large position tolerance was observed in the model results, which meant that the detector position in experimental setup was not a critical factor, as long as the detector was placed near the beginning of water channel.

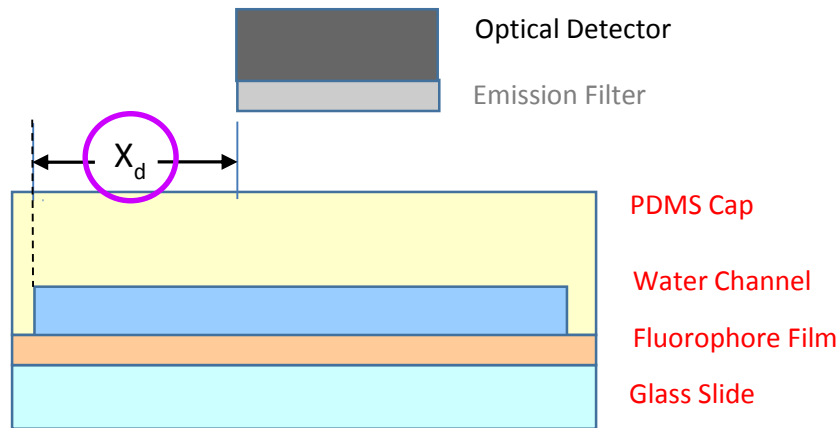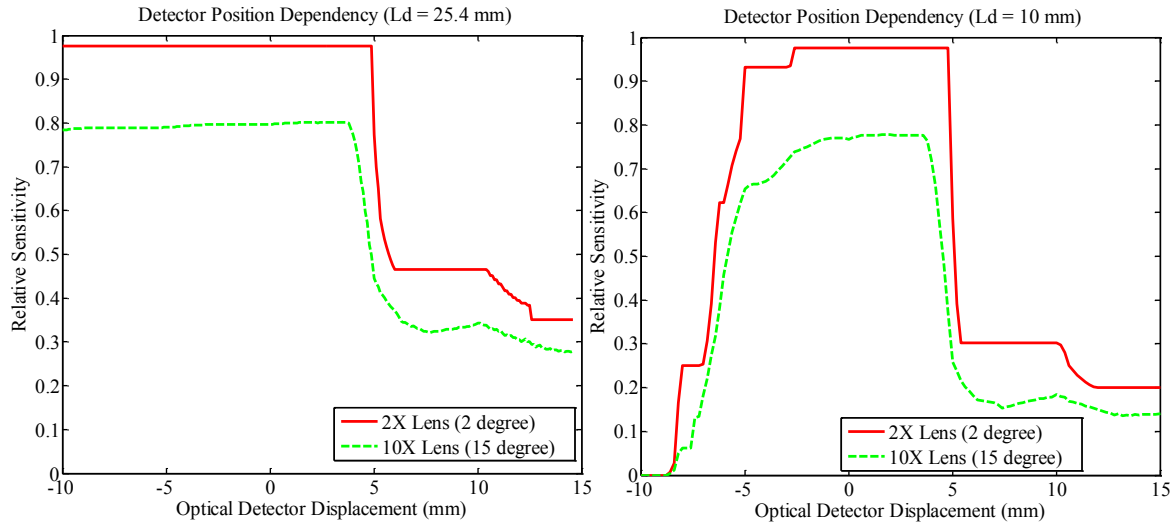**Model results on Optical Detector Position**

Figure 3.18 (above) Model results of relative sensitivity on optical detector positions and (below) the schematic of how the detector position was defined in the sensor setup. Detector position was defined by the distance between the beginning of the detector and the start of the water channel (minus for left displacement of detector and plus for right displacement of detector). The detection lengths considered in this figure were 25.4 mm and 10 mm respectively. The position tolerance was 15 mm for 25.4 mm detection length and 7 mm for 10 mm detector length. Spatial tolerance for the detector position was fairly large.

- **Collection efficiency of emission**

In ref [63], a DO sensor structure was used where the evanescent part of the excitation light (which was confined within SU-8 waveguide) excited fluorophores. The authors injected the excitation light from one end of the waveguide and collected the emission light from the other end of the waveguide, which led to only the part of the emission light rays that met TIR criterion could be collected by the optical detector. As we knew the fluorescent emission was isotropous in a uniform environment, the collection mechanism in ref [63] led to some loss in collected emission intensity. We named this collection mechanism as 'end collection', which served as a reference for the proposed emission collection mechanism in this work.

Model Results of Collection Efficiency

Detection Length Dependency of Different Emission Collection Mechanisms
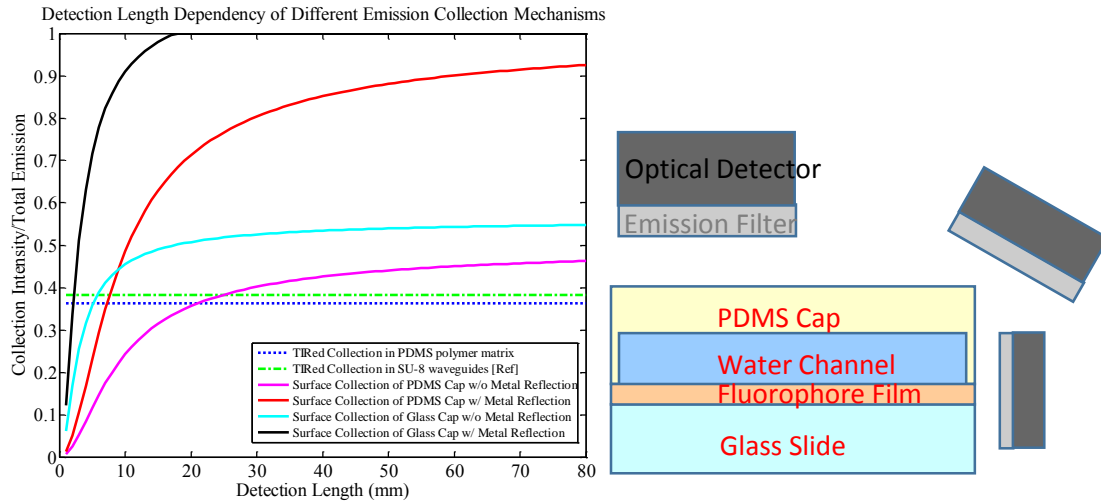

Figure 3.19 (left) Model results of collection efficiency on different emission collection mechanisms and (right) the schematic of how the optical detector could be placed in our system. In reference (D. A. Chang-Yen et al. An integrated optical oxygen sensor fabricated using rapid prototyping techniques), only emission light that met the angle criterion of TIR was collected and detected by the spectrometer. In our design, the optical detector was placed on top of the fluorophore film and resulted in a larger solid angle of collection. Furthermore, if we changed the PDMS cap into a glass slide cap (1 mm) and added a metal reflective layer at the bottom of the sensor, the collection efficiency was even better and exceeded the reference method when detection length was longer than 2 mm.

The collection mechanism we used in our system, which was named 'surface collection', was different from ref [63], in that we collected the fluorescence emission on top of the fluorophore film, making a possible bigger solid angle in collecting the emission. Here we assumed a uniform distribution of fluorescent emission intensity among the 4π solid angle in the fluorophore film of the sensor. The effects of different collecting mechanisms upon the collection efficiency (the ratio of collection intensity over emission intensity) would be analyzed in this part.

Let us first look at 'end collection' in the waveguide structure of ref [63] and in the sensor structure in this work. In ref [63] the direction of fluorescent emission light coming from the fluorophores must meet the angle criterion of TIR inside the SU-8 waveguide, in order to be collected by the spectrometer at the end of the waveguide; the collection efficiency result was shown in green in the graph of Figure 3.20. In the sensor structure in this work, the optical detector was placed at the other lateral side of the sensor (opposite to the light source and the objective lens) in 'end collection' (Figure 3.20). The polymer matrix for the fluorophores was PDMS, which was surrounded on top by water and PDMS cap and at bottom by glass slide. This sandwiched structure also formed a waveguide for the emission light. The TIRed collection efficiency in such a structure was shown in blue in the graph of Figure 3.20.

On the other hand, if 'surface collection' is considered, the collection efficiency would have a direct link with the detection length of the sensor, as a longer detection length corresponded to a bigger solid angle in collecting the emission. In addition, if an Al reflective film was added at the bottom side of the glass slide (reflectivity 89%), downward emission light could be reflected upward and the collection efficiency could nearly double. The model results of this surface collection were shown in magenta and red in the graph of Figure 3.20. If the 3 mm thick PDMS water channel cap was further replaced by a 1 mm thick glass slide, which allowed the optical detector to come nearer to the fluorophore, an even bigger solid

angle could be resulted and a larger proportion of emission intensity was collected; results of this glass cap were shown in cyan and black in the graph of Figure 3.20.

As shown in Figure 3.20, the 'end collection' mechanism in the sensor materials we used and in ref [63] (green and blue straight lines) was compared with 'surface collection' mechanism. In comparison to 'end collection', a better collection efficiency was achieved by 'surface collection' mechanism with Al reflective film and glass cap when the detection length was longer than 2 mm; over 90% collection efficiency could be achieved in this case when the detection length was 10 mm. These results demonstrated the advantages of 'surface collection'. Instead of 7 mm which was obtained in last part when considering sensitivity dependency on detection lengths, 10 mm could be determined as the min value for the optical detector dimension as well as the water channel length. Conclusion had also been reached that 'surface collection' was a more efficient method than 'end collection', as long as the detection length of the system remained in a reasonable range.

- **Glass substrate thickness**

It has been discussed in previous parts about the influences of the relative dimension and position of the optical detector in the system setup; in this and following several parts, focus will be given to the influences from sensor structure dimensions. In previous discussion, a commercially available BK-7 glass slide which was 1 mm thick was assumed as the substrate of the sensor. If in mass production, the thickness of glass substrate could be customized as long as enough mechanical support was provided and good fabrication accuracy was achieved. The thickness of the glass substrate would influence the distance between two consecutive excitation sites on the fluorophore film, in all Type 1, Type 2 and Type 3 scenarios; thus it affected the absorption efficiency and the relative sensitivity of the sensor. A Matlab model to quantitatively determine the influences of glass substrate thickness was therefore presented here.

Model results were shown in Figure 3.21. Glass substrate thicknesses varying from 0.1 to 10.0 mm were examined with excitation beams from 2X and 10X objective lenses. It is assumed in the model that the excitation beam diameter also changed with the thickness of glass slide substrate, so all excitation energy could be injected into the DO sensor. The thinner the glass substrate the higher the potential sensitivity was, which was resulted from a less distance between excitation sites. It is shown that the max system sensitivity started to drop significantly around 3 mm of glass thickness, so 3 mm could be regarded as the upper limit of the glass substrate thickness. When 1 mm thick glass slide for microscopes was employed in sensing setup, little sensitivity increase could be gained when reducing the glass thickness to below 1 mm.

As shown in the upper right graph of Figure 3.21, when the incident angle of excitation was considered combined with the glass thickness, the acceptable incident angle range also remained nearly the same when lowering the thickness of glass substrate. Taking into account that a thinner glass substrate required fabrication customization and led to mechanical weakness, the default choice of a commercially available glass slide with 1 mm thickness was regarded as a nearly optimum choice in the sensor design.
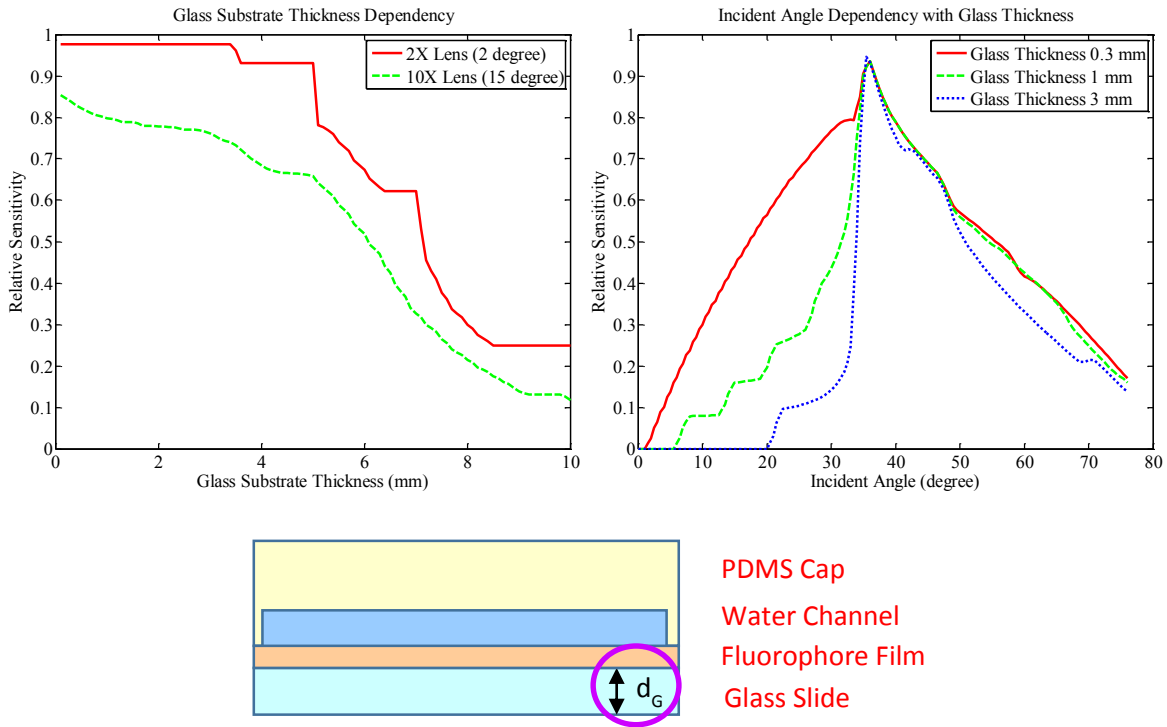
Model Results on Glass Substrate Thickness

Figure 3.20 (above) Model results of relative sensitivity on glass substrate thicknesses and (below) how the glass substrate thickness was defined in the sensor structure. The thickness of the glass substrate influenced the distance between two consecutive excitation sites on the fluorophore film, and thus it affected the absorption efficiency and the relative sensitivity of the sensor. The thinner the glass substrate the higher the potential system sensitivity was. It is shown that the max system sensitivity started to drop significantly around 3 mm of glass thickness. When 1 mm thick glass slide for microscopes was employed in this setup, little sensitivity increase could be gained if we further decreased the glass thickness.

- **PDMS water channel cap thickness**

Besides the glass substrate thickness, the PDMS cap thickness in the sensor structure also influenced the excitation light pathways, particularly in Type 3 scenario (in Figure 3.14) when the light was TIRed inside the 4-layer structure of the sensor. One of the purposes of the PDMS cap was to hold the testing water in channel and to give the whole sensor a mechanical support. Another purpose was to prevent any gas exchange between the ambient air and the testing water, in order to maintain the oxygen concentration unchanged. Since PDMS was a material with high oxygen diffusivity and we even used it as the fluorophore polymer matrix in the sensor, a thick enough PDMS cap was desired to minimize oxygen permeation, as permeation was inversely related to film thickness according to Fick's Law. In this part discussion is focused on the optical influences of the thickness of PDMS water channel cap in the sensor.

From previous analysis it is known that the max sensitivity was achieved when the incident angle of excitation was in Type 2 scenario, where the excitation was TIRed inside the glass slide and the fluorophore film, and this scenario was optically irrelevant to the thickness of PDMS cap. Model results also confirmed this as shown in Figure 3.22. The three lines of different PDMS thickness (1, 3, 5 mm) coincided near the peak of emission rate, with variations only in the area when incident angles were larger than 47.5 °in Type 3 scenario. This figure also verified that PDMS cap had no impact on the tolerance of

the incident angle for max sensitivity. It was worth noting that there was a hump observed in the curve near 60 °when PDMS cap thickness was 5 mm; it was due to the fact that 60 °incident angle could result in more excitations sites than 57 °incident angle at this (25.4 mm) detection length, leading to a larger emission. As the model results proved that PDMS cap thickness influenced neither the max sensitivity nor the range of the incident angle, in following parts, the PDMS cap thickness was still assumed to be 3 mm.

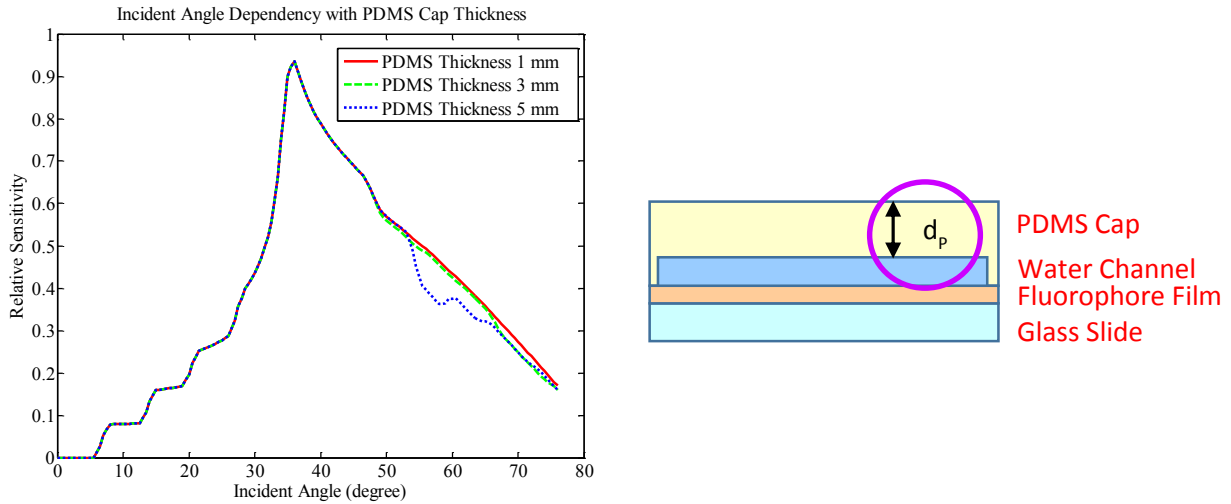**Model Results on Incident Angles Using Different PDMS Cap Thicknesses**

Figure 3.21 (left) Model results of relative sensitivity on incident angles using different PDMS cap thicknesses and (right) the schematic of how the PDMS cap was defined in the sensor structure. As we saw in previous discussion, max point of sensitivity was achieved in Type 2 scenario (incident angle of excitation θ less than 47.5°) in the sensor structure, so PDMS cap thickness posed no influence on the max sensitivity. This figure verified that the PDMS cap also had no impact on the tolerance of the incident angle for good DO sensitivity.

- **Light source horizontal displacement**

In addition to the placement of the optical detector and the dimensions of sensor structures, the alignment of the light source to the sensor, represented by the position of the objective lens in the setup, also posed an influence on DO sensitivity. In this and the next part, the influences of the imperfection of objective lens position will be discussed, which could help determine the position accuracy requirements. It is assumed in previous discussion that a Gaussian beam with spatial standard deviation 0.37 mm (obtained experimentally by a beam profiler) was aligned with the glass slide substrate of the DO sensor; the excitation also stayed just beneath the 2 mm wide water channel to excite the fluorophores that are influenced by oxygen in testing water. In experiments, this perfect alignment may not be met, and the displacement and skew of the light source (objective lens) could happen.

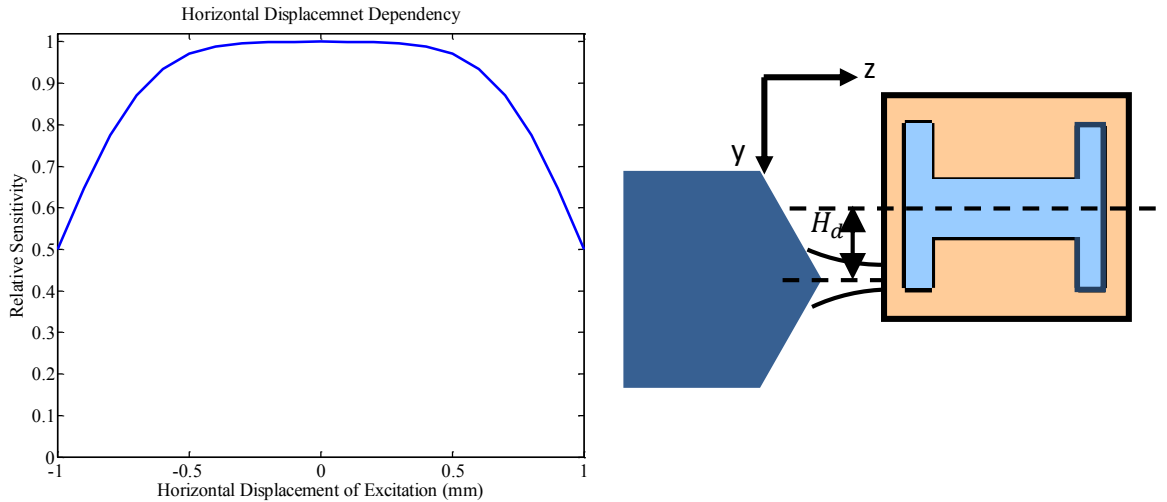# Model Results on Horizontal Displacements of Objective Lens

Figure 3.22 (left) Model results of relative sensitivity on horizontal displacements of the objective lens and (right) the schematic of how the horizontal displacement of the light source was defined in the system setup. We regarded the coincidence of the excitation light and the axis of water channel as 0 displacement. The water channel width was 2 mm. In this model we used Gaussian beam assumption (verified by experiments) and the experimental value of beam spatial standard deviation 0.365 mm. As we saw from the graph, horizontal displacement tolerance was ±5 mm.

In this part the horizontal displacement of the light source will be discussed, which implied that the direction of the excitation light was still the same with water channel length (Z axis in system schematic). The definition of the light source displacement we discussed here was shown in the schematic in Figure 3.23. The coincidence of the excitation light and the axis of water channel was regarded as 0 displacement. The horizontal displacement in Y-Z plane was focused here, because any displacement in this plane would lead to system sensitivity reduction by exciting the fluorophores outside the reach of oxygen. In contrast, although light source displacement in X-Y plane (not shown here) influenced how much excitation energy can be injected into the sensor, which resulted in emission intensity change, this displacement did not affect sensitivity since all the excited fluorophores were still in good contact with oxygen from testing water.

Model results of the light source displacement were also shown in Figure 3.23. It was shown that large horizontal displacements of the excitation light source reduced the system sensitivity. Although a displacement within the range ±0.5 mm aroused little influence, any displacements larger than this range led to fast drop in sensor performance. It was also worth noting that this tolerance range of displacement was related to the width (in Y axis) of the water channel, as well as the excitation beam standard deviation; thus the model results here were only applied to the set dimensions in this part. In conclusion, 1 mm was regarded as the tolerance range for the horizontal position of the objective lens in the sensing setup.

- **Light source skew angle**

Besides horizontal displacement, the direction of the excitation light could also make an angle to the central axis of the water channel in the sensor, and we defined this angle as 'light source skew angle' γ (schematic shown in Figure 3.24). The alignment of the excitation light and the direction of water channel length was regarded as 0 skew angle. The skew of the light source in the Y-Z plane of the system could reduce the sensitivity of the DO system, as part of the light exceeded the boundary of water channel and

excited the fluorophores that were beyond oxygen contact. The skew of the light source in the X-Y plane was not considered in this part, for it would not influence DO sensitivity.

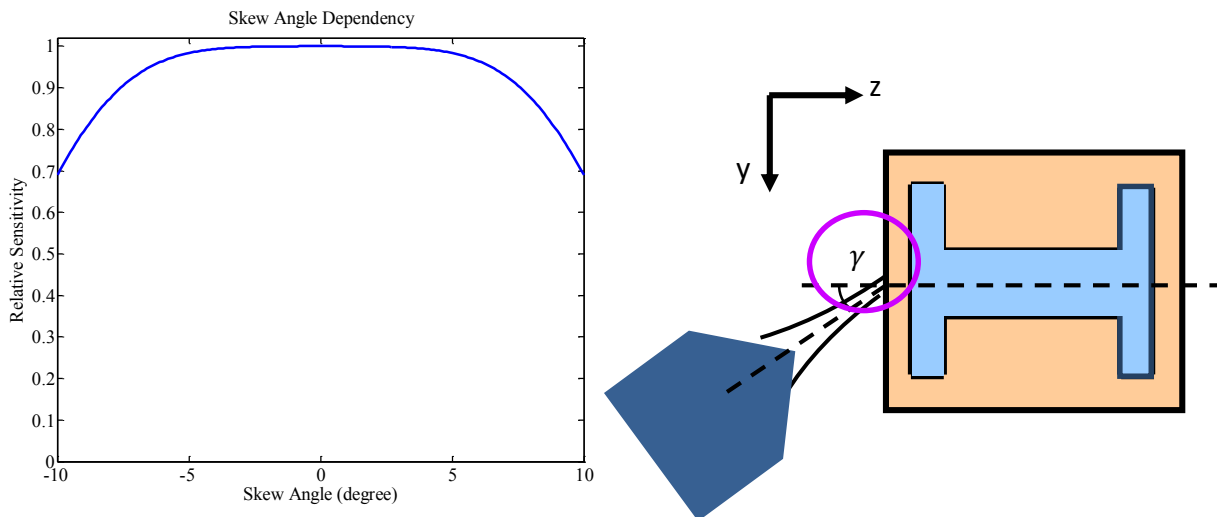**Model Results on Skew Angles of Objective Lens**

Figure 3.23 (left) Model results of relative sensitivity on skew angles of the objective lens and (right) the schematic of how the skew angle of the light source was defined in the system setup. We regarded the alignment of the excitation light and the direction of water channel as 0 skew angle. The water channel width was 2 mm. In this model we used Gaussian beam assumption (verified by experiments) and the experimental data of beam size standard deviation 0.365 mm. The skew angle tolerance was $\pm 5°$.

Model results were shown in Figure 3.24. It was shown that large skew angles of the excitation light reduced DO sensitivity. A skew angle within the range $\pm 5°$ aroused little influence, yet any skew angle beyond this range led to a fast drop in sensor performance. Based on this analysis, $10°$ was regarded as the tolerance range for the skew angle of the objective lens in the horizontal plane. It is worth noting that this value was also related to the excitation beam shape and the length and width of the water channel.

- **Fluorophore film thickness**

Although fluorophore film thickness was one of the dimensional parameters in the sensor structure, unlike other dimensions that were discussed in previous parts, it cannot be analyzed by deduction from Fresnel's Law and Beer-Lambert Law: experimental results in published papers [86] scratched a picture that thinner fluorophore films showed higher sensitivity, which was contradictory to the prediction based on Beer-Lambert Law that a thicker film can absorb more excitation. In addition, it is observed that thicker films showed more obvious downward curvature in Stern-Volmer plot in our experimental results (that would be given in the next chapter). As far as we know, this phenomenon still lacked a detailed explanation which should include a physical model. The experimental evidence forced us to find out explanations that were based on other principles.

Let us first look at how people dealt with model modifications in fluorescence based DO sensors. Several methods existed for explaining the imperfections of DO sensor performances and their non-obeisance to Stern-Volmer equations. Among them the two-site model was used to describe the microscale inhomogeneity of fluorophores in immobilized polymer matrices. In contrast to the case of fluorophores in liquid, the fluorophores in polymer matrices were often heterogeneous on microscale and this fact gave

rise to complex decay kinetics in quenching. The two-site model assumed that the fluorophore existed in two distinctly different environments (different accessibility for oxygen) with one being fully quenchable and the other being unquenchable or little quenchable. This two-site model could be shown as [21]

$$\frac{I}{I_0} = \frac{f}{1+K_{sv}^1[O_2]} + \frac{1-f}{1+K_{sv}^2[O_2]} \qquad (3\text{-}21)$$

where f was the fraction of the total emission from fully quenchable fluorophores in zero-oxygen condition, and k_{sv}^1 and k_{sv}^2 were the Stern-Volmer quenching constants for the two kinds of fluorophores. When the little quenchable fluorophores was entirely unquenched, $k_{sv}^2 = 0$.

Inspired by this two-site model, we proposed a model explaining the sensitivity dependency on fluorophore film thickness. Here it is assumed that the concentration of fluorophores was evenly distributed in the full thickness d of the fluorophore film. Inside the film, a very thin top layer of fluorophores (thickness d_0) which was in direct contact with oxygen molecules in testing water had a complete sensitivity k_a to oxygen quenching ('optimum thickness' d_0); in comparison to that, the fluorophores beneath this thin layer in the rest of the fluorophore film had a much lower sensitivity to oxygen, which we defined as sensitivity k_b, and $k_b = k * k_a$ where $k \ll 1$. Thus the factor f, which was the fraction of total emission from the fully quenchable fluorophores in zero-oxygen condition, could be written as $f = d_0/d$.

The target of the deduction process here was to obtain f and k from experimental data e.g. emission intensity F at different DO concentrations. In this way we could obtain the function of sensitivity dependency on the fluorophore film thickness. Total fluorescence in the absence of quenchers could be stated as

$$F_0 = F_{0b} + F_{0a} \qquad (3\text{-}22)$$

where F_{0a} and F_{0b} represented the fluorescence intensity coming from fully quenchable and partially quenchable fluorophores respectively and $f = F_{0a}/F_0$. When quenchers were present, the fluorescence could be written as

$$F = \frac{F_{0a}}{1+k_a[Q]} + \frac{F_{0b}}{1+kk_a[Q]} \qquad (3\text{-}23)$$

where $[Q]$ represented the quencher concentration, k_a represented the sensitivity of fully quenchable fluorophores and $k * k_a$ represented the sensitivity of partially quenchable fluorophores. By subtraction of the two equations and division by F_0, we got

$$\frac{\Delta F}{F_0} = f\frac{k_a[Q]}{1+k_a[Q]} + (1-f)\frac{kk_a[Q]}{1+kk_a[Q]} \qquad (3\text{-}24)$$

Considering $k \ll 1$, if small terms are dismissed and the equation above was reversed, we obtained

$$\frac{F_0}{\Delta F} = \frac{1+k}{k+(1-k)f} + \frac{1}{[k+(1-k)f]k_a}\frac{1}{[Q]} \qquad (3\text{-}25)$$

Thus the plot of $\frac{F_0}{\Delta F}$ versus $\frac{1}{[Q]}$, where $\frac{F_0}{\Delta F}$ and $\frac{1}{[Q]}$ were all experimentally acquirable, yielded $\frac{1+k}{k+(1-k)f}$ as the intercept; thus an equation of k and f could be obtained by the intercept of the plot from a set of emission intensity data at a given fluorophore film thickness. Because $f = d_0/d$ and 'optimum thickness'

d_0 did not change with fluorophore thicknesses, two sets of the emission intensity data at different fluorophore film thicknesses could provide us with an equation set in which d_0 and k were solvable.

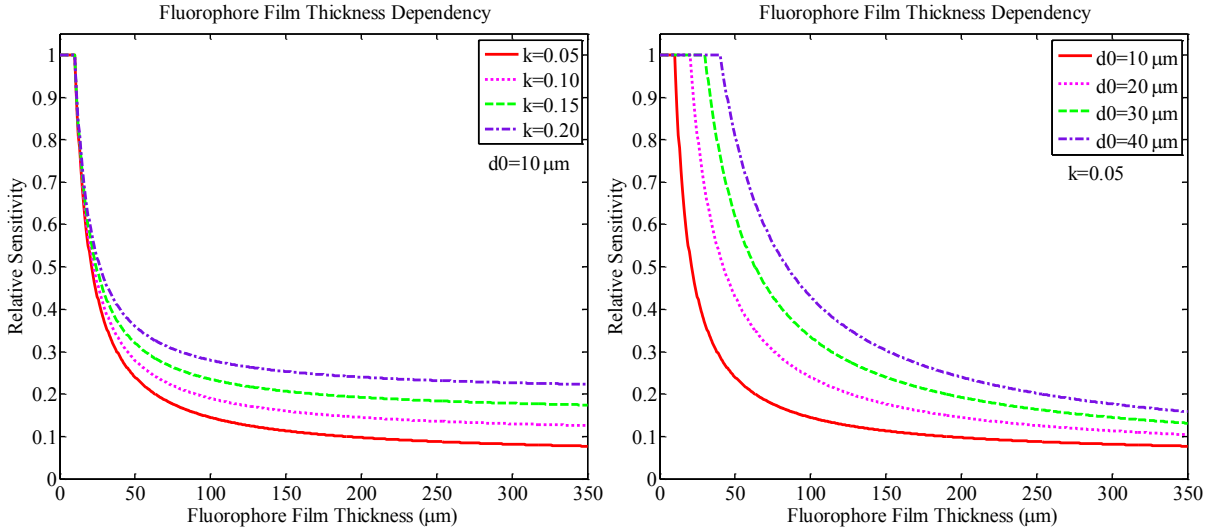**Model Results on Fluorescence Film Thickness**

Figure 3.24 Model results of relative sensitivity using different parameters in fluorescence film thickness model. The left graph showed how the sensitivity would change with fluorophore film thickness when 'optimum thickness' d0 remained the same and the quenching constant ratio k changed from 0.05 to 0.20, and the right graph showed how the sensitivity would change when k remained the same and d0 changed from 10 μm to 40 μm. In principle, relative sensitivity reduced in a hyperbolic relationship when the fluorophore film thickness exceeded the optimum thickness.

Two illustrative plots of the sensitivity's dependency on fluorophore film thickness were shown in Figure 3.25. The left graph showed how the sensitivity changed with fluorophore film thickness when 'optimum thickness' d_0 remained the same and the quenching constant ratio k changed from 0.05 to 0.20, and the right graph showed how the sensitivity changed when k remained the same and d_0 changed from 10 μm to 40 μm. In principle, relative sensitivity reduced in a hyperbolic relationship when the fluorophore film thickness exceeded the optimum thickness.

In summary, with respect to fluorophore film thickness, the sensitivity of DO sensor could be given as

$$K_{sv} = \frac{d_0}{d} k_a + \left(1 - \frac{d_0}{d}\right) k k_a \qquad (3\text{-}26)$$

where d_0, d and k_a were defined before. The specific d_0 and k in certain sensor depended heavily on the sensor structure and the thermodynamic characteristics of the quenchers. What the model in this part did was to predict how the sensor would perform at any fluorophore film thickness given two scenarios were provided. Our experimental results of DO sensitivity at different fluorophore film thicknesses (shown in Chapter 4) would also be analyzed in this way.

- **Response time**

The fluorophore film thickness not only influenced DO sensitivity, but also affected the response time of the sensor. Intuitively, the thicker the fluorophore film the slower the response was.

In ref [87] [88], the authors explored oxygen diffusion energy in different polymer complexes using Stern-Volmer fluorescence techniques and Fickian transport model. The time dependency of reduced fluorescence intensity was deducted as

$$\frac{I_t}{I_0} = A + \frac{8C}{\pi^2} \exp\left(-\frac{D\pi^2 t}{d^2}\right) \qquad (3\text{-}27)$$

where d was the polymer thickness and D was the oxygen diffusivity, $C = k_q \frac{\tau_0}{V} O_2(\infty)$ and A = 1-C, V was the total volume of the fluorophore film, k_q was the quenching constant and τ_0 was the lifetime of the fluorophore used [87] [88].

From the above equation it was shown that the emission response of a DO sensor followed an exponential function. The characteristic response time was proportional to the square of the fluorophore film thickness. Reducing the fluorophore film thickness was valuable to increase the response speed as well as to enhance DO sensitivity. Yet when choosing an appropriate thickness, many other factors matter, such as preventing overly reduced fluorophore film thickness (like 1 μm) in order to maintain consistent performance. Detailed discussion on the emission intensity reduction of newly fabricated sensors will be given in Chapter 4.

- **Excitation directly into the fluorophore film**

In the discussion till now, the excitation light was always injected into the glass slide substrate of the DO sensor, and then TIRed inside part or all of the sensor structure. If a step is taken further, possible better excitation efficiency might be obtained if the excitation travels solely inside the fluorophore film. So in this part we would discuss this possibility.

First let us look at the optical properties of each layer to see whether the case could be met. In the sensor design, the refractive index of the fluorophore film (1.42, PDMS as immobilized polymer matrix) was smaller than glass substrate (1.52), which made it impossible for TIR inside the fluorophore without further modifications. In this part an Aluminum reflective film could be inserted between the PDMS based fluorophore film and the glass substrate: the reflectivity of Al was 89% at 445 ~ 450 nm excitation, so the major part of excitation could be reflected back into the fluorophores (see Figure 3.21 for the schematic).

As an alternative way, a different polymer matrix could be tried. Besides PDMS which we focused on before, PVC (Polyvinyl chloride) and SU-8 (epoxy based) were also commonly used as immobilized polymer matrices in DO sensors and they enjoyed good oxygen diffusivity (refer to Section 2.1.2). The refractive indices of PVC and SU-8 photoresist were 1.54 and 1.82 respectively which were larger than that of glass slide. So the Al reflective film between the fluorophore film and glass could be omitted if the polymer matrix was changed from PDMS to PVC or SU-8.

Model results of relative sensitivity on PDMS (with Al reflection), PVC and SU-8 as immobilized polymer matrices were shown in Figure 3.26, where the size of the excitation beam was assumed to be identical with the fluorophore film thickness. The relative sensitivity '1' in Y-axis of the graphs referred to 100% absorption of excitation light, the same as before in the cases of excitation into the glass slide, so the relative sensitivity here could be compared with previous results. As shown, the best absorption

efficiency of the sensor was achieved at incident angles near 0 °. Sudden changes in the emission rate in all lines were due to transitions from TIR inside fluorophore film into TIR inside a more-layer structure.

Model Results on Incident Angles in Fluorophore Excitation Configuration
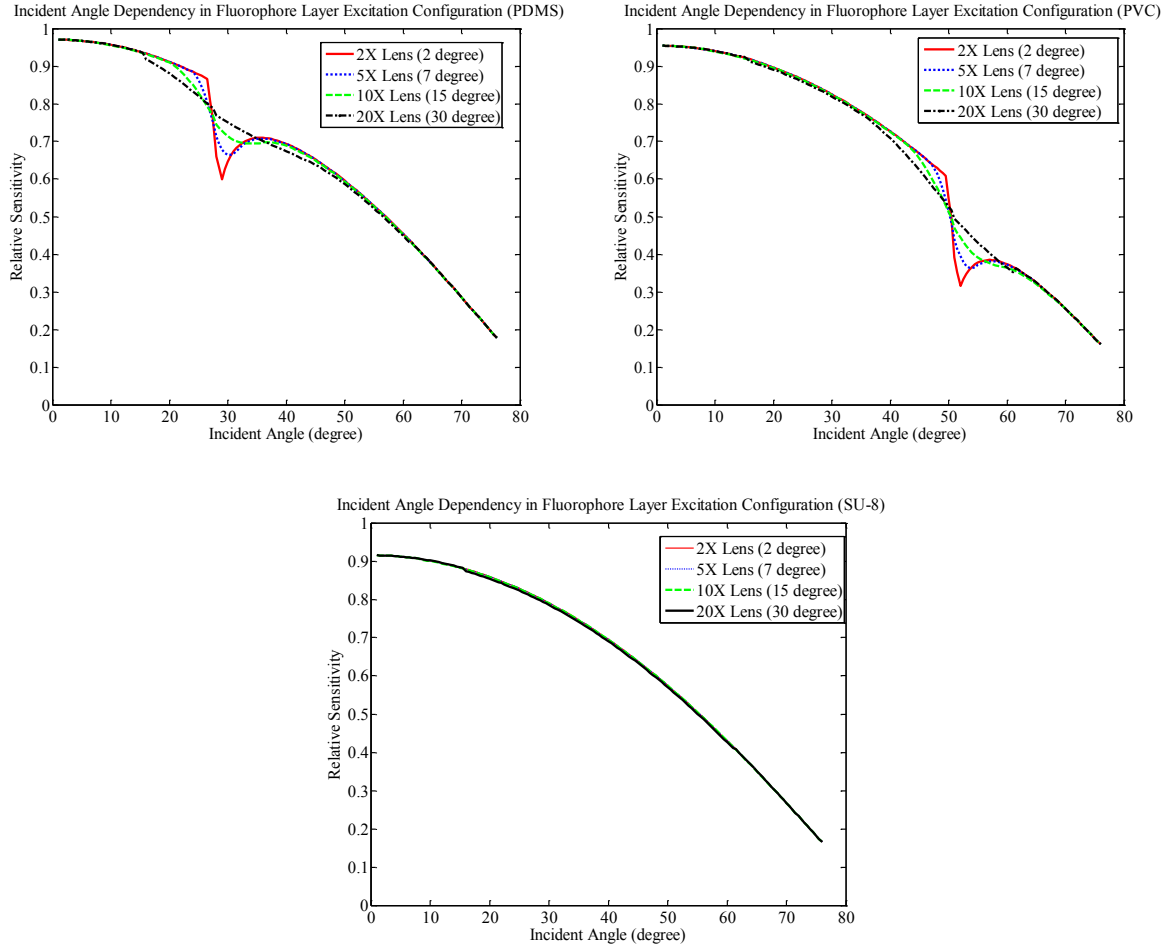

Figure 3.25 Model results of relative sensitivity using PDMS (with Al reflective film), PVC and SU-8 as immobilized polymer matrices. Excitation light was injected directly into the fluorophore film. As the refractive index of PDMS polymer matrix (1.42) was smaller than that of glass slide (1.52) an Aluminum reflective film was added between the fluorophore film and the glass slide; PVC (n=1.54) and SU-8 (n=1.82) have refractive indices larger than that of glass, so the Al film could be omitted. Best absorption efficiency of the sensor was achieved at incident angles near 0 ° in all three materials. Sudden changes in the system sensitivity in all lines were due to the transitions from TIR inside the fluorophore film into TIR inside a more-layer structure.

When the highest possible sensitivity is concentrated, the interested range of the incident angle would be in the vicinity of 0 ° as shown in Figure 3.26. In this range, the excitation light was TIRed inside the fluorophore film without entry into any other layers. Thus there was no need to discuss the influences of the thicknesses of PDMS cap, water channel and glass slide. Instead, the actual beam size of excitation light, which might be much larger than the thickness of the fluorophore film, determined how much excitation could enter into the fluorophore film, so the injection rate played an important role in the actual DO sensitivity.

It is assumed in Figure 3.26 that the beam size of the excitation light was the same as the thickness of the fluorophore film (10 μm). As a matter of fact, this condition was very difficult to meet in experiments even with the help of an optical fiber. Thus an optical model of the excitation beam size dependency was presented in Figure 3.27 for the analysis of fluorophore layer excitation efficiency.

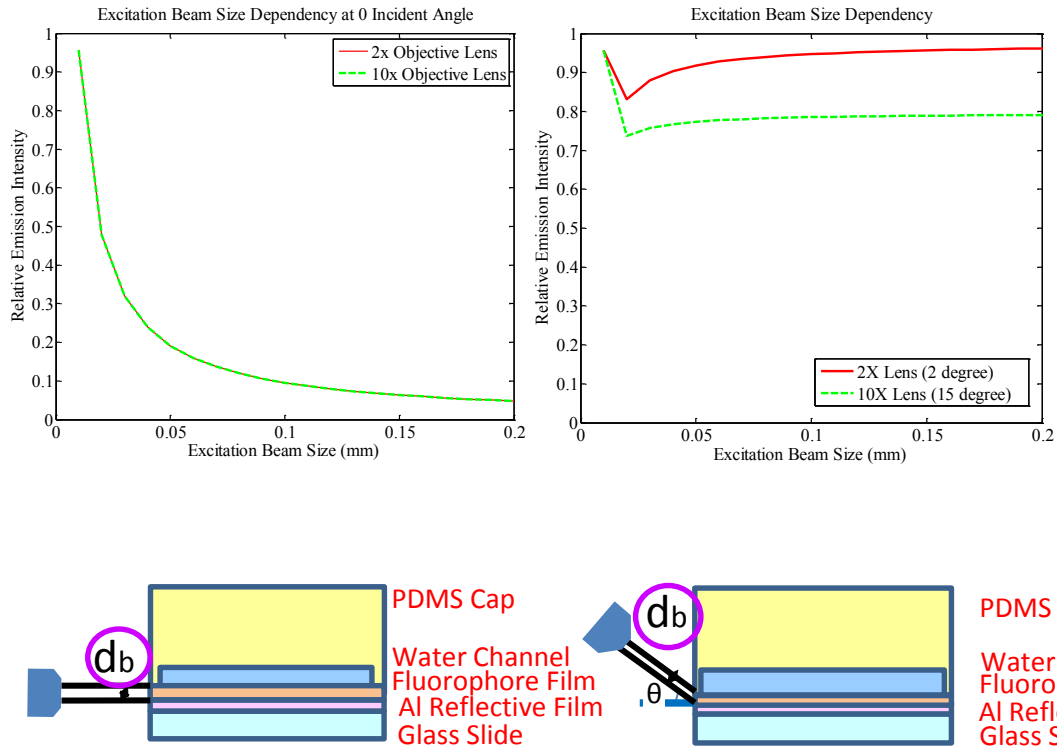**Model Results on Excitation Beam Size in Fluorophore Excitation Configuration**

Figure 3.26 (above) Model results of relative sensitivity on the excitation beam size in fluorophore film excitation configuration and (below) schematics of how the excitation beam sizes were measured in the system. The upper left graph was the sensitivity results when the incident angle was maintained near 0 ° and the upper right graph was the results when incident angle was set freely. Here we took the example of PDMS polymer matrix with Al reflective film. As we saw, relative emission intensity decayed rapidly with larger excitation beam near 0 °incident angle; while the sensitivity could be compensated partially when the incident angle was set freely.

The PDMS polymer matrix (with Al reflective film) was taken as an example in this analysis. Only interested in the effects of beam sizes larger than the thickness of fluorophore film, it is assumed that the residual part of excitation light was injected into the layer of water and PDMS water channel cap, travelling in the pattern of TIR inside PDMS cap/water/fluorophore layers. The excitation light would not enter into the glass substrate as there was an Al film between the fluorophore film and the glass. The model was built with the beam size of excitation varying from 10 μm to 200 μm. The upper left graph showed the emission rate near 0 °incident angle: the relative sensitivity decreased hyperbolically with larger beam sizes; the upper right graph presented the max emission intensity for all incident angles: there was a turning point at 0.02 mm in the line (where the beam size was the double of the fluorophore film

thickness), which implied a transition from the fluorophore layer excitation domination to more-layers' excitation domination. In the latter case, TIR inside PDMS cap/water/fluorophore layer occurred, which resulted in absorption efficiency increase at larger incident angles. The results in this part have shown that an incident angle near 0 °and a small enough excitation beam size would be suggested if TIR inside the fluorophore film is considered.

3.4 Fabrication of sensor structure

The fabrication process of this oxygen sensor is briefly summarized as below:

1). 74 * 25 mm^2 BK-7 glass slide was cleaned by isopropyl alcohol (IPA); if needed sputter a 200 nm Al film on one side of glass slide;

2). PDMS was made by mixing the base and the curing agent (10:1 w.t.);

3). Fluorophore film was made by mixing Ru(dpp)$_3$, ethanol and PDMS prepolymer (1:10:200 w.t.); the film was then spin-coated onto a glass slide (for 10 μm film, spinning 6000 rpm for 1 minute);

4). Solidify the PDMS/pluorophore film by heating at 100℃ for 1 hour;

5). PDMS based water channel was made by conventional soft-lithography method;

6). The PDMS channel was then; bonded with fluorophore film by air plasma. The inlet and outlet of water channel were then connected to flexible tubes for syringe injection;

7). If needed, bonding another glass slide on top of PDMS cap by air plasma to reduce the thickness of PDMS cap and to block gas exchange between water channel and ambient air.

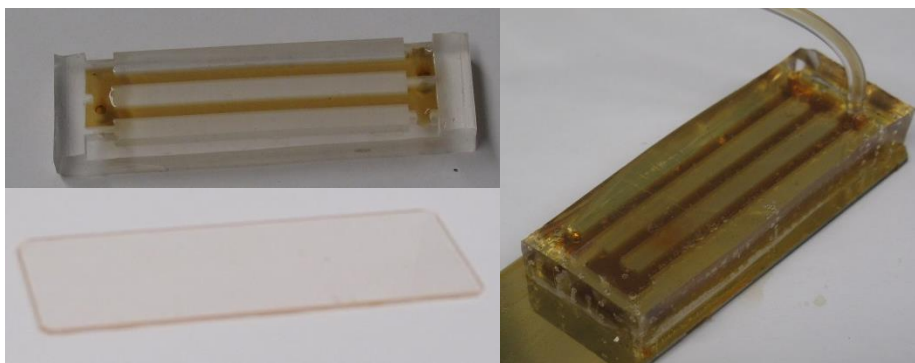**Photograph of DO Sensor Fabrication**

Figure 3.27 The photographs of a PDMS based water channel (upper left), a spin-coated fluorophore film on top of the glass slide (bottom left) and a fabricated DO sensor with Al reflective film at the bottom (right).

Chapter 4   Characterization

In Chapter 3, the details of design and fabrication process of fluorescence quenching based DO sensors were discussed. Employing total-internal-reflection as the sensitivity enhancement method, a number of factors on senor performance were considered in a Matlab model. Feasibility of using an optical power meter and a diode laser was demonstrated based on spectral results; the detailed fabrication process was given as well. All these served as a foundation for the characterization of the DO sensor in this chapter.

The system setup for characterization was depicted in Section 4.1. Preliminary characterization results are given in Section 4.2, for the purposes 1) to test whether the assumptions in the model in Chapter 3 were reasonable, 2) to figure out the working conditions and requirements of this optical sensor and 3) to verify the specifications of essential parts in the system. Section 4.3 introduces the characterization of DO sensitivity. Section 4.4 presents an accuracy estimation of the sensor.

4.1 Characterization system setup

This section presents the operation setup of DO sensor; it applies to the following discussion on system characterization unless otherwise noted.

The DO sensor was placed on an adjustable optical stage, which was immobilized at a desired angle to the excitation beam. A blue diode laser (350 mW, 445~450 nm, Model 20003151, Laserland, Wuhan, China) with collimated output was settled as the light source without additional excitation filter. The power of the excitation laser was 250 mW for enough emission intensity. A ZEISS A-plan 10X / 0.25 Ph1 objective lens in microscope was used for laser focusing. Its purpose was to condense the optical intensity and to reduce the beam size into ~1 mm in diameter for excitation into the glass slide of the sensor; it also gave the excitation beam a cone angle of 15-20 °. The sensor was adjusted in 3-axis movement in order that the glass slide could be at the beam waist of the excitation. In a top view of the setup, the pathway of the excitation light in the sensor was adjusted in the vertical plane of the water channel, in order to excite the fluorophores that were oxygen contacting. Once excited, the fluorophores generated isotropic emission with max intensity peak at 620-625 nm, which was proved by the spectral study in Section 3.2.1. According to the design, the excitation light was total-internal-reflected inside part of all layers of the sensor, resulting in multiple excitation and emission sites in the fluorophore film. A detailed discussion of TIR pattern could be found in Section 3.3.

The quenching effect of oxygen upon the fluorophores was regarded as a thermodynamic process. The oxygen molecules in the testing water diffused into the gas permeable fluorophore layer (made of PDMS) according to Fick's Law. Thermal motion of oxygen molecules made them collide with the fluorophores, and the excessive energy in the excited fluorophores was transferred to ground state oxygen, which was then excited; the fluorophores that lost energy in the process returned back to ground state without optical emission. The fluorescence intensity was thus bimolecularly quenched in the presence of oxygen. The performance of a perfect DO sensor (which meant a uniform distribution of the fluorophores in microscale in the immobilized polymer matrix) followed the prediction of Stern-Volmer equation, in which the reduced emission was inversely proportional to DO concentration.

An OD 6 520-700 nm bandpass filter (BrightLine [TM], FF01-609/181-25, Semrock, Rochester, NY) was placed on top of the sensor for spectral selection of the emission light, and an optical power meter (Model 1830-C, Newport, USA) as the optical detector was located behind the emission filter, in order to

exclude any light interference from excitation and in the ambient environment. The emission filter and the optical detector were particularly placed in the orthogonal direction to the excitation light pathways, to further reduce the excitation intensity seen by the detector. The edge of the optical detector was put in coincidence with the beginning of the water channel in the sensor, for maximizing the collection efficiency of the emission light (model results provided in Section 3.3). Figure 4.1 presented a photograph of the system setup, together with a lateral side picture of DO sensor.
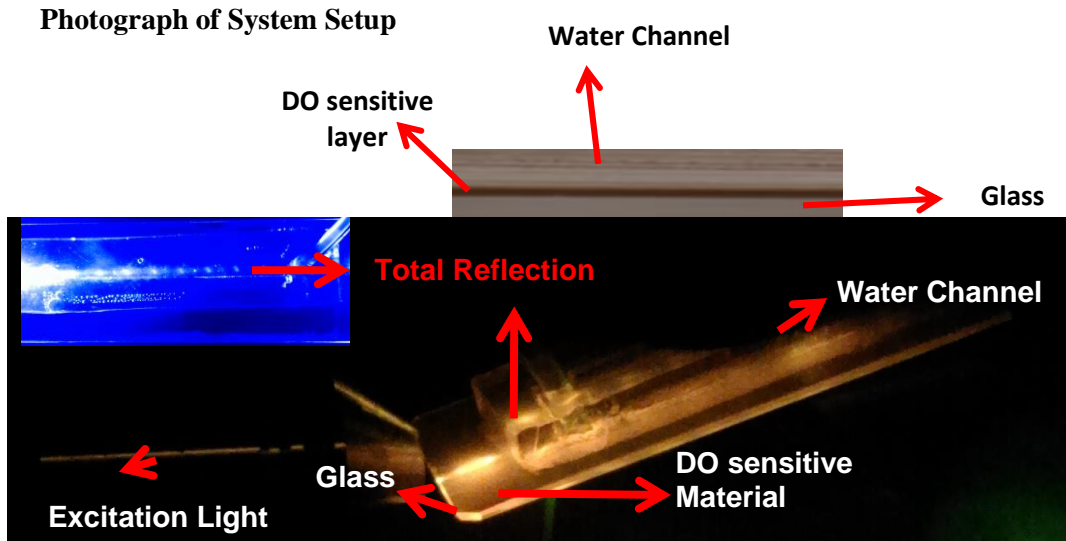

Figure 4.1 (below) Photograph of the system setup for characterization and (top) a lateral side picture of the sensor structure.

Testing water with different DO concentrations was made up of deionized water (18.2 MΩ.cm) pumped with nitrogen and oxygen gas in cylinders. Nitrogen gas (99.9999% pure) and oxygen gas (99.9999% pure) were purchased from Alphagaz (Montreal, Quebec). 10 mL capacity syringes were used to inject the testing water into the inlet of the water channel in sensors. DO concentration in water was calibrated by the optical DO sensing module in a commercially available water quality monitor (Model U-2000, Horiba, Japan).

Table 4.1 summarizes the system components we employed, together with their key specifications, physical size and price for reference. For the ease of system validation, optical power meter and diode laser were employed in this work as a prototype choice. In future development, they could be replaced by photodiode and LED respectively, which would reduce system cost and size. In addition, based on the best incident angle result in this work (Figure 3.15, Figure 4.7 and Figure 4.8), the OD requirements of emission bandpass filter could be much reduced if we use a fixed angled V-grooved fiber (instead of microscope objective lens) for excitation injection: excitation light would be TIRed and trapped inside the sensor (model results shown in Chapter 3), therefore several orders of magnitude less excitation could travel beyond the sensor and reach the optical detector placed on top. When all abovementioned optimizations are achieved, system hardware cost is expected to be less than US $50. Compared with commercially available optical DO sensors which often charge for more than US $700, our solution paved the way for great reduction in cost and size and still offer the same functionalities and even better sensitivity [26].

Summarization of System Components

Components	Key Specifications	Size	Price (USD) [*]	Future Choice [*]
Laserland 450 nm blue diode laser	FWHM 2 nm, 350 mW	4*4*7 cm	$50	LED $10
ZEISS 10X objective lens	NA 0.25, Ph1	3*3*5 cm	$30	Single mode optical fiber $4
Semrock BrightLine™ 609/181 bandpass filter	Transmission 520-700 nm, OD 6 @ 450 nm	2.54*2.54*1 cm	$300	Edmund Optics OD 4 bandpass filter $25
Newport 1830-C optical power meter	190-1800 nm, 100 fW to 2 W	Probe 2*2*4 cm Processor 19*9*22 cm	$500	Photodiode $10
Thorlab Optical stage	Angular adjustment precision 1 °	10*10*10 cm	$70	None
Optofludic sensor (with water injection tube)	Glass, PDMS, plastic tube	3*1*8 cm	N/A	N/A
Syringe	10 mL	1*2*10 cm	$2	None

[*]*Please refer to Appendix 2 for purchase link of each component.*

Table 4.1 Summarization of system components. Key specifications, physical size, reference price and future choice of each component are included. In future development of this work, diode laser and optical power meter could be replaced by LED and photodiode respectively; optical stage and bandpass filter are omitted and V-grooved fiber is used instead of objective lens. These optimizations could further reduce system size and cost.

4.2 Preliminary characterization

4.2.1 Absorption rate of fluorophore film

In the optical model of Chapter 3, we calculated the absorption efficiency of the fluorophore film based upon Beer-Lambert Law and used it to analyze relative DO sensitivity. Four factors, which included the extinction coefficient of the fluorophore, the fluorophore concentration in the film, the fluorophore film thickness and the incident angle of the excitation light into the film, were considered in the optical model. In this section we tried to confirm this calculation by testing the absorbance *A* of the fluorophore film, which was then compared against the theoretical value.

The testing setup of the absorbance was shown in Figure 4.2. The excitation light was incident perpendicularly to the 10 μm thick fluorophore film inside the DO sensor. An optical power meter (Model 1830-C, Newport, USA) was placed before and after the fluorophore film and the recorded values were in the absence and presence of light absorption by the fluorophores. A dark experiment was also conducted to account for the ambient light. Five pairs of optical intensities (one before the fluorophore film and one after in each pair) at different powers of the excitation were shown in Table 4.2. According to a statistical analysis, the absorbance of the fluorophore was A = 0.141 ± 0.005.

According to Beer-Lambert Law, the absorbance A of a structure was the parameter that bridged the theoretical and experimental phenomena of absorption. On one hand, A could be derived as the negative logarithm of the transmitted intensity over the original intensity from experimental results as what we did in Table 4.2; on the other hand, A could be expressed as the product of εcl, where ε was the absorptivity of the light attenuator, c was the concentration of the light attenuator in the structure and l was the distance through which light travelled. As for the theoretical case, the absorptivity of the light attenuator in our case was 29500 $M^{-1}cm^{-1}$ of $Ru(dpp)_3^{2+}$, concentration of light attenuator was 50 mg $Ru(dpp)_3Cl_2$ in 10 mL PDMS, and the distance through which light travelled was 10 μm of fluorophore film thickness. By multiplying them up, we obtain theoretically that the absorbance A was 0.1273.

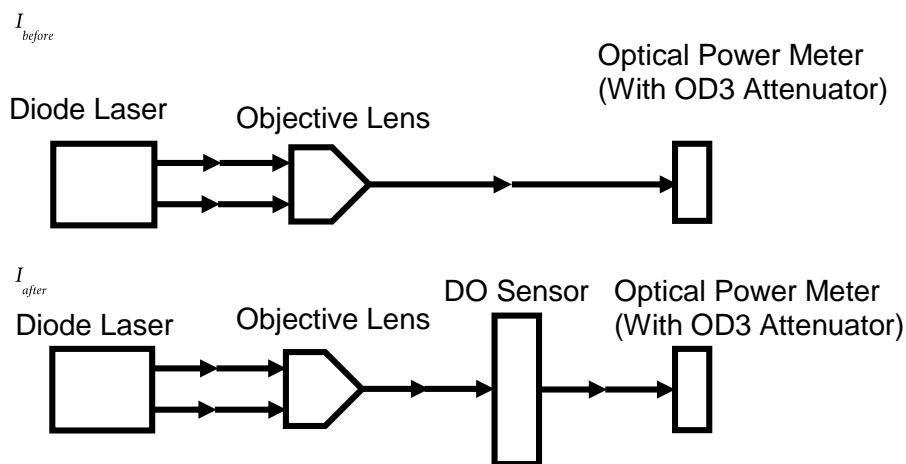**Schematic of Setup in the Experiment of Fluorophore Film Absorption Rate**

Figure 4.2 The schematic of test setup in the experiment of fluorophore film absorption rate. The above picture represented how Ibefore was measured and the bottom picture represented how Iafter was measured. The absorbance of the fluorophore film was a function of Iafter / Ibefore.

Results Summary of Fluorophore Film Absorption Rate Experiments

I_{before} (μW)	I_{after} (μW)	I_{after} / I_{before}	$A = -\log_{10}(I_{after} / I_{before})$
10.20	7.30	0.7157	0.1453
21.98	15.92	0.7243	0.1401
44.27	32.25	0.7285	0.1376
61.54	45.03	0.7317	0.1357
73.40	52.22	0.7114	0.1479

Table 4.2 Results summary of the absorption rate experiments of 10 μm fluorophore film in DO sensor. A 450 nm diode laser light was incident perpendicularly to the fluorophore film inside DO sensor. Ibefore and Iafter were the measured optical intensities before and after the fluorophore film respectively. Iafter / Ibefore and A were calculated values. According to a statistical analysis, the absorbance of the fluorophore was A=0.141 ±0.005.

From above results, it was shown that the theoretical and experimental values of absorbance were comparable, but the experimental one was larger than the theoretical one. Several reasons may contribute to this fact. For example, the whole sensor was used as the light absorber in the absorbance measurement; thus other materials in the sensor especially the glass slide and PDMS cap could influence the test results by light absorbing or scattering, which all contributed to a bigger value in absorbance experiment. In addition, any slight change of the incident angle of the excitation also increased the light pathway, which further built on the experimental absorbance value. As a result, it is understandable that the experimental value is slightly larger than the theoretical one.

4.2.2 Optical density of emission filter

The emission filter is an indispensable part of any fluorescence sensing system. Considering the quantum mechanical processes in fluorescence, the emission intensity of fluorescence is 10^6 times lower than that of the excitation, so a powerful emission filter that can block the excitation wavelength is necessary. In the light of this, an experiment which assures the optical density of the emission filter under excitation wavelength is of great value. This experiment is conducted in this section.

In the characterization setup of the sensor, a 520-700 nm bandpass filter (BrightLine ™, FF01-609/181-25, Semrock, Rochester, NY) was used as the emission filter, which was settled just before an optical detector (the optical power meter) for minimization of environmental noises. This emission filter was notated to have an OD 6 at the excitation wavelength 445 ~ 450 nm. To verify the optical density, a testing setup was built as shown in Figure 4.3. In order to accommodate to the detection range of the optical power meter, an OD 3 optical attenuator was used additionally; thus the optical density of the attenuator was also verified. Test results were summarized in Table 4.3; I_{before} of emission filter, I_{after} of emission filter, I_{before} of attenuator, and I_{after} of attenuator were measured values corresponding to the four steps in Figure 4.3. OD in emission filter test and OD of attenuator were calculated values and the sum of them would be the OD of emission filter. According to a statistical analysis, the emission filter OD at excitation wavelength was 5.16 $\pm$ 0.04, which was slightly smaller than the notated value.
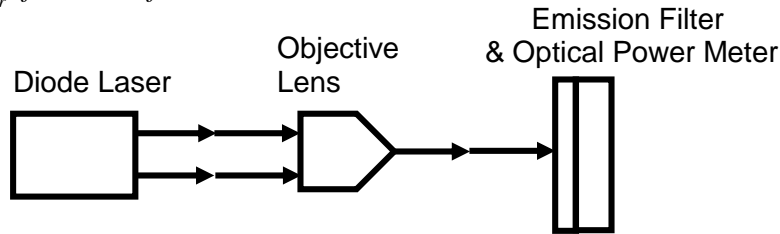
Results Summary on OD Test of Emission Filter

I_{before} of emission filter (μW)	I_{after} of emission filter (μW)	OD in emission filter test = $\log_{10}(I_{before} / I_{after})$	I_{before} of attenuator (μW)	I_{after} of attenuator (nW)	OD of attenuator = $\log_{10}(I_{before} / I_{after})$	OD of emission filter = OD in emission filter test + OD of attenuator
62.55	0.4703	2.12	17.370	16.955	3.0105	5.13
52.92	0.3463	2.18	8.468	8.203	3.0108	5.19
55.43	0.3919	2.15	13.567	13.073	3.0161	5.17
29.16	0.1992	2.17	4.135	3.968	3.0159	5.19
79.15	0.6645	2.07	30.15	29.04	3.0163	5.09

Table 4.2 Results summary of measurements for the optical density of the emission filter. Ibefore of emission filter, Iafter of emission filter, Ibefore of attenuator, and Iafter of attenuator were measured values corresponding to the four steps in Figure 4.9. OD in emission filter test and OD of attenuator were calculated values and the sum of them would be the OD of the emission filter. According to a statistical analysis, the emission filter OD at our excitation wavelength was 5.16 ±0.04.

Schematic of Test Setup in Experiment of OD of Emission Filter

I_{after} of emission filter

Diode Laser

Objective
Lens

Emission Filter
& Optical Power Meter

I_{before} of attenuator

Diode Laser

Objective

Optical Power Meter

I_{after} of attenuator

Diode Laser

Objective Lens

OD3 attenuator
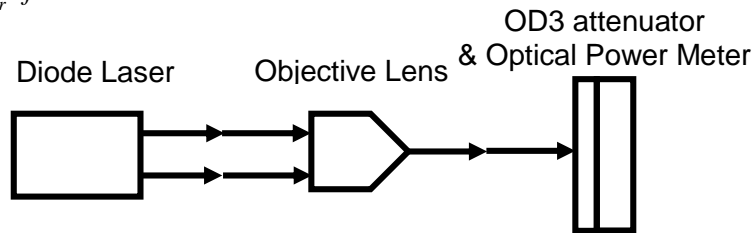& Optical Power Meter

I_{before} of emission filter

Diode Laser

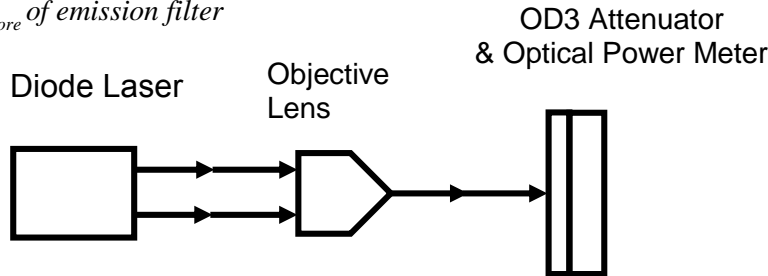Objective
Lens
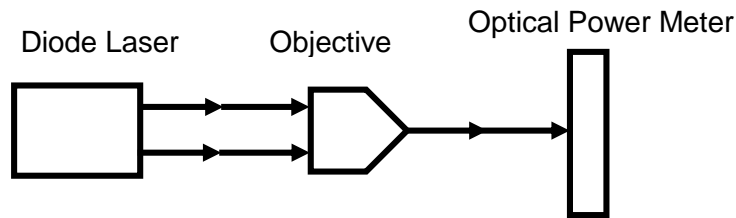
OD3 Attenuator
& Optical Power Meter

Figure 4.3 The schematic of the test setup in the experiment of the optical density of emission filter. The above two pictures represented the procedure of the emission filter test and the bottom two depicted how the optical density of the OD 3 attenuator was verified. Results of the values in each step of the test could be found in Table 4.5.

4.2.3 Repeatability of emission readouts

The DO sensor in this project is intensity based, where the DO concentration relies on the readouts of emission intensities. An optical power meter (Model 1830-C, Newport, USA) was used to obtain the readouts and their repeatability was directly related to the sensor accuracy. The power meter we used enjoyed power measurements from 100 fW to 2 W in the range of 190 ~ 1800 nm. Such a broad measurement capability naturally resulted in the use of multiple sensors in the power meter, and therefore the question of measurement accuracy was aroused. The emission readouts test in this section was

designed in response to this, where we recorded the readouts between switching on and off the optical power meter itself and on and off the room light.

Results of the measurements were shown in Table 4.4. The numbers in the same set were intensities between turning on and off the power meter. The numbers between different sets are intensities between turning on and off the room light (when optical intensity changed from nW to µW and then changed back) while the power meter was left working. From the table it was shown that switching the optical power meter led to a ~0.4% readout change; in contrast, turning on and off the room light generated changes up to 2.4%. Further verification was also conducted when both the power meter and room light were switched on and off: <0.5% readout change was observed. Based on the facts above, it was presumed that the recalibration between switching the optical power meter had little influence on the emission readouts, while several orders of magnitude change of the light seen by the detector (resulted from switching the room light) did have a bigger impact on the final values. This influence might be rooted in the change of the optical sensor and/or the magnification circuits inside the power meter.

Results Summary of Repeatability of Emission Intensity Experiment

Set 1	378.5	379.2	380.1	379.3	379.9
Set 2	373.4	373.1	373.3	374.6	374.7
Set 3	381.8	381.2	381.6	381.3	382.0

Table 4.3 Results summary of the emission intensity experiment. The numbers in the same set were intensities between turning on and off the power meter. The numbers between different sets were intensities between turning on and off the room light (when optical intensity changed from nW to µW and then changed back) while the power meter was left working. From the table it was shown that switching the optical power meter led to a 0.4% readout change; in contrast, turning on and off the room light generated changes up to 2.4%. Therefore as a lesson of this test, we need to forbid the turning on of room light in the whole process of the characterization experiments hereafter.

Therefore as a lesson of this test, we need to forbid the turning on of room light in the whole process of the characterization experiments hereafter. Furthermore, we suggest that a permanent optically-opaque cover can surround the light source, the optical detector and the fluorophores in the mass produced sensors, in order that the influences coming from any optical change in the environment are diminished.

4.2.4 Calibration of DO concentration

To characterize the sensitivity of DO sensor in this project, water samples with different DO concentration were added into the sensor and then measured to obtain different emission intensities. These water samples were prepared by pumping pure oxygen and nitrogen gas into deionized water and the DO concentrations were calibrated by a commercially available optical DO sensor (Model U-2000, Horiba, Japan). Therefore the accuracy of this calibrator influenced the characterization preciseness in this project.

This commercial DO sensor claimed to have a detection range 0-20 ppm with accuracy ±0.2 ppm [89]. 0, 5, 7, 12, 20 ppm of DO concentration were employed as the benchmarks in the sensitivity characterization of our sensor later on, so in this section, water samples were prepared with such concentrations and uncertainties were measured by the Horiba Sensor. Measurement results were shown in Table 4.5 and uncertainties at 0, 5, 7, 12, 20 ppm of DO concentration were all less than 0.2 ppm. Based on the results, ±0.2 ppm as stated in calibration sensor's specification was sufficient to describe the uncertainty. This uncertainty was thus used as the errorbars for DO concentration in the Stern-Volmer plot hereafter.

Results Summary of Uncertainty Experiment by Calibrator

Notated DO concentration (ppm)	0	5	7	12	20
Measured Concentration by calibrator (ppm)	0.05	4.93	7.03	12.03	19.98
	0.13	5.01	7.11	11.98	19.97
	0.09	4.98	7.02	12.12	19.99
	0.03	4.91	6.98	12.09	19.83
	0.11	4.87	6.95	11.98	19.87
Uncertainty of DO concentration (ppm)	0.10	0.09	0.07	0.08	0.11

Table 4.4 Results summary of uncertainty experiment by the calibrator (Horiba Sensor for Water Quality Monitor U-2000). We used these five different DO concentrations in sensitivity characterization in our DO sensors and thus this table showed the uncertainty of notated DO concentration in later characterization experiments. It is shown that ±0.2 ppm as stated in the commercial sensor's specification was sufficient to describe the uncertainty. This uncertainty was used as the errorbars for DO concentration uncertainty in the characterization hereafter.

Photograph of the Calibrator Optical DO Sensor

Figure 4.4 Photograph of the calibrator optical DO sensor (Horiba Sensor for Water Quality Monitor U-2000). The dimension of the detector exceeded 35 cm as shown in the picture.

4.2.5 Emission power loss of new sensors

When a DO sensor was fabricated and set up in the system, it was interesting to observe that an initial process of operation was required before any characterization experiments and/or use for DO measurement. The sensors experienced a significant reduction in emission intensities in this process. We named this phenomenon as the emission power loss.

It was worth noting that the emission power loss was irrelevant to DO concentration change. We controlled the DO concentration to be stable in this initial process. The emission power loss which was still observed was resulted from a reduction of the absolute quantity of fluorophores. Since some of the fluorophores were immobilized loosely in polymer matrix, in the initial operation, when the flowing test water started to contact with the fluorophore film, these fluorophores were gone with the water and

flushed away. This washing led to a loss of the fluorophores present in the sensor, and thus the emission power was permanently reduced without recovery capability.

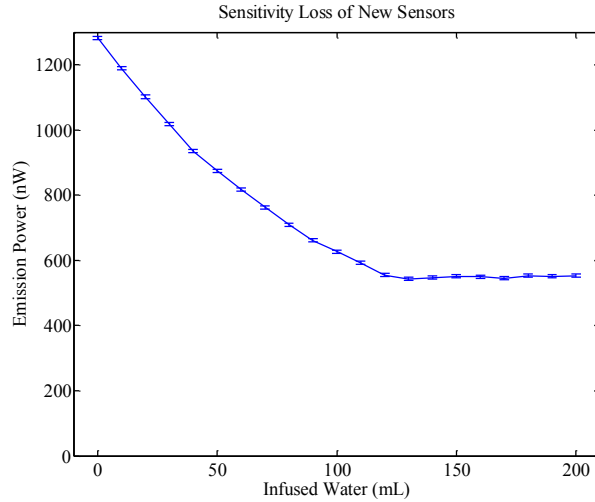### The Emission Power Loss at the Beginning of Operation

Figure 4.5 The emission power loss at the beginning of operation in a newly fabricated DO sensor. DO concentration in testing water was controlled at 0. This emission power loss was due to a reduced quantity of fluorophores. Some fluorophores which were unstable in the polymer matrix were washed away by running testing water in the beginning of operation. After this initial process, the emission power remained stable.

Results Summary of Emission Power Loss Percentage

I_{before} (nW)	I_{after} (nW)	Drop Percent
1283	555	56.7%
1839	892	51.5%
2237	950	57.5%
783	397	49.3%
2021	776	61.6%

Table 4.5 Results summary of emission intensity loss in five newly fabricated DO sensors. Ibefore was the emission power in the first time of water injection into newly fabricated sensors, and Iafter was the emission power when the unstable fluorophores was washed away and the emission power stopped dropping. Typically 100-200 mL water was required in order that the sensors reached Iafter. The drop percent of emission power was 55 ±5%.

Figure 4.5 recorded the speed of emission power loss with continuously flowing water in the channel of a DO sensor. DO concentration was controlled at 0 in testing water. Approximately 120 mL water (equivalent to 12 injections of 10 mL syringe) was needed to flush away the unstable fluorophores in this new sensor. After this process, the sensor maintained the emission intensity and functioned consistently. Table 4.6 showed the summary of total drop percentage in emission intensities of five newly fabricated sensors. Typically 100-200 mL water was required in order that the sensors reached stable performance. The drop percent of emission power was 55 ±5%.

In summary, the emission power loss phenomenon we observed in DO sensors made it necessary a 'shower' in every newly fabricated sensor, especially those sensors that were designed for continuous monitoring. This shower would reduce part of the DO sensitivity, but currently it is necessary for repeated and stable sensor performance.

4.2.6 Dynamic sensing

It is mentioned earlier that there were three methods of DO measurement: chemical, electrochemical and optical. Among them the electrochemical method is dependent on oxygen reduction reaction (ORR) in the electrolyte so it consumes oxygen in operation. In this way electrochemical DO sensors require frequent stir or rapid flow of the testing water, in order to make the DO concentration near the sensors remain refreshed. The optical method, on the other hand, recycles oxygen molecules as the quenchers and therefore could perform in a static environment. This characteristic is regarded as a big advantage of the optical method.

For environmental applications, DO sensors are supposed to work in both natural aqueous conditions and artificial ones (e.g. waste water treatment plants). The water in such conditions can either be flowing or static. Having known that the optical sensor could perform in static water, we are also interested in whether the sensor could function in dynamic water environment. In this section, we would figure out whether the emission intensity of the sensor remains stable if the testing water is flowing inside the water channel of the DO sensors.

Results Summary of Emission Intensity Changes in Dynamic Sensing

Static intensity (nW)	Fluctuation in static state	Min dynamic intensity (nW)	Max dynamic intensity (nW)	Dynamic fluctuation
658	1.5%	643	663	3.1%
620	1.6%	598	632	5.3%
560	1.0%	551	575	4.4%
605	1.7%	584	618	5.0%
521	0.7%	508	546	3.8%

Table 4.6 Results summary of emission intensity changes in dynamic sensing. Five different DO sensors were examined. The optical intensities before the injection of flowing water and the max and min values during the water flowing were shown in this table. DO concentration was 0 and the flow rate of the water was controlled at 0.5 mL/s. Fluctuations in static and dynamic conditions were compared. This table showed that we could obtain a much less fluctuation and a better accuracy on DO sensing when the water in channel was static. If necessary, small mechanical shutters are suggested at the inlet and the outlet of the water channel to keep the water static in channel.

A syringe was used to inject the testing water into the water channel. In this section, DO concentration was 0 and the flow rate of water was controlled at 0.5 mL/s. Frequent changes of the emission intensity readouts from the original value (in static state) were observed, and their max and min values in such flowing process of 20 s (the capacity of the syringe for injection is 10 mL) were recorded in Table 4.6. Five different DO sensors were investigated.

As shown in Table 4.7, the flowing water injection aroused a much bigger dynamic fluctuation in emission intensity than static fluctuation. The variations in dynamic process were in the scale of dozens of nW while the static variations were only ~ 1 nW. Several factors might contribute to this phenomenon. One of the factors could be that the flowing water disturbed the oxygen distribution inside the water channel and in the fluorophore film, so the oxygen quenched the fluorophores to a different degree;

another factor might be that the gas bubbles and other substances inside the testing water scattered the emission light from the fluorophores to a different extent.

No matter what the reasons were, one thing was clear that we could obtain a much better accuracy of DO sensing when the water in channel was static. Therefore in later characterization experiments we concentrated on scenarios with static water. If such sensors are required to work under flowing water conditions in future, small mechanical shutters are suggested at the inlet and the outlet of the water channel, making the water in the channel remain static when optical measurements are in progress.

4.3 Characterization of DO sensitivity

4.3.1 Incident angle of excitation

From this section, the experimental exploration of the best structures and parameters for sensitivity enhancement will be presented in the DO sensor we proposed. Glass layer excitation was employed as it was much easier to realize, when compared with fluorophore film excitation (details see Chapter 3). In this section, we focus on exploring the relationship between incident angle of excitation and the sensor performance. The fluorophore film thickness was set to be 10 μm in this section.

Two sizes of sensors were explored. One was the regular size with features 1) water channel length (Z axis) 40 mm, 2) water channel width (Y axis) 2 mm, 3) PDMS water channel cap 3 mm and 4) without Al reflective film at the bottom; the other was in a miniaturized size with features 1) water channel length (Z axis) 10 mm, 2) water channel width (Y axis) 1 mm, 3) glass water channel cap 1 mm and 4) with Al reflective film at the bottom. As we would find out in Section 4.3.3, Al reflective film at the bottom of the device only doubled the emission intensity but not influenced sensitivity; the purpose of making a miniaturized sensor in this section was to test the miniaturization potential of the sensor device. For example, the water channel length 10 mm and the glass water channel cap were chosen based on the model results on detection length and emission collection efficiency in Chapter 3.

In the experiments, we fastened the fabricated DO sensor on an adjustable optical stage which had angular adjustment capability as well as 3-axis movement. The 445 ~ 450 nm excitation diode laser and the objective lens were fixed parallel to the optical table, in order that the output direction of the excitation light was in the horizontal plane. To further check the angle between the excitation light and the DO sensor plane (with the glass slide edge at the beam waist of the excitation output), a protractor was used to measure this angle with uncertainty less than 1 °. Five different incident angles (15 °, 25 °, 35 °, 45 °, 55 °) were studied in the experiments, which covered our interested range in the model results on incident angle dependency. As for DO concentration, more sample data points were explored in the biologically interested range of 0~5 ppm. A 10X objective lens (ZEISS A-plan, NA 0.25) was used for the regular sized sensor; a 20X objective lens (ZEISS A-plan, NA 0.5) was used for the miniaturized sensor because of smaller water channel width in this case. Schematics to show how the test was performed, together with a photograph of the miniaturized sensor, were shown in Figure 4.6.

Schematic of Incident Angle Definition in DO Sensors

Glass Slide
PDMS Cap
Water Channel
Fluorophore Film
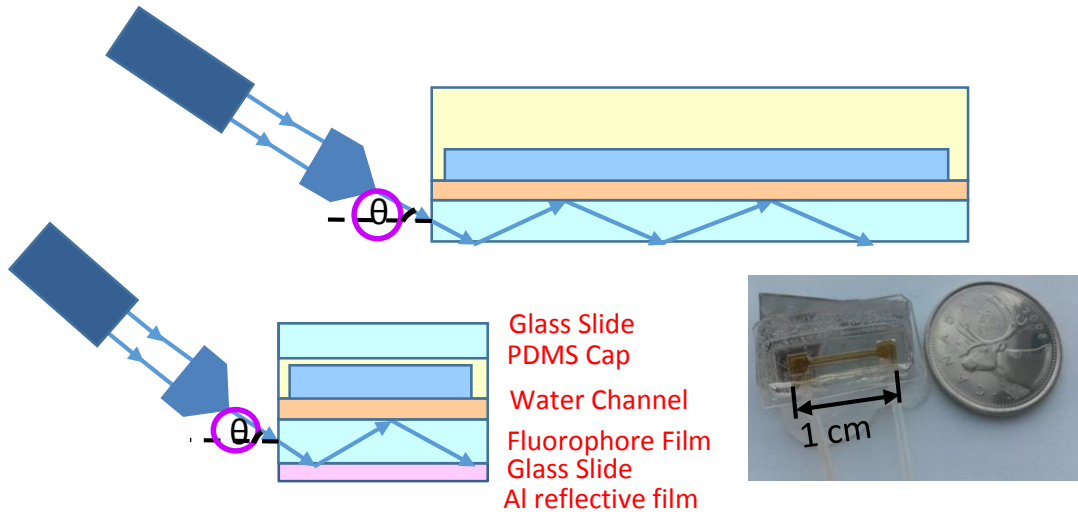Glass Slide
Al reflective film

1 cm

Figure 4.6 (above) The schematic of how the incident angle of excitation was defined in regular sized sensor, (bottom left) the schematic of how the incident angle was defined in miniaturized sensor and (bottom right) a photograph of the miniaturized sensor.

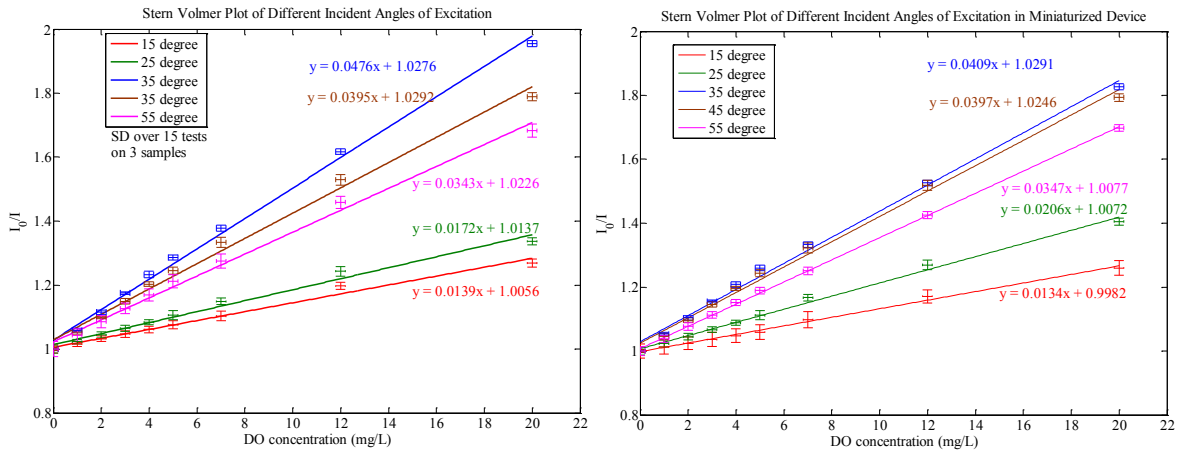## Stern-Volmer Plot of Sensors with Different Incident Angles

Figure 4.7 (left) Stern-Volmer plot on different incident angles in regular sized sensors and (right) Stern-Volmer plot on different incident angles in miniaturized sensors. 5 different incident angles were examined. The horizontal errorbars were set to be 0.2 ppm which was the accuracy of the calibrator DO sensor. The vertical errorbars were the standard deviation of repetitive experiments. The system sensitivity could be represented by the slope of different lines. As we saw, different incident angles led to different sensitivity. This was due to different total-internal-reflected light pathways in the sensor at different angles, which influenced the absorption efficiency of fluorophores. Concisely speaking, the absorption efficiency was increasing when the incident angle was below 35 ° and decreasing when above 35 °.

Comparison between Experimental and Model results of DO Sensitivity on Different Incident Angles of Excitation
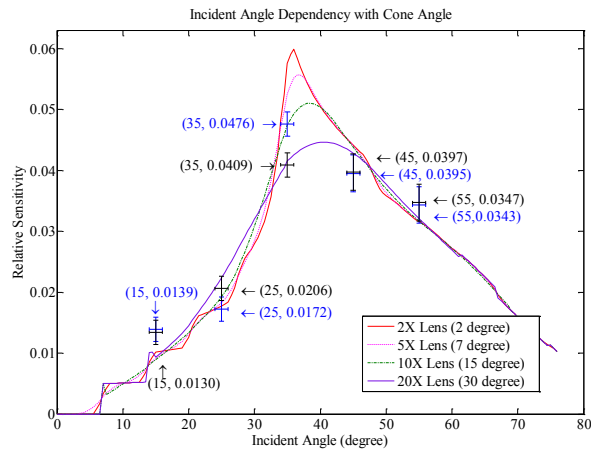

Figure 4.8 Comparison between experimental and model results of DO sensitivity on different incident angles of excitation. A coefficient based on the experimental sensitivity of the regular sized sensor at 35 °incident angle was used to match model and experimental sensitivities in all other scenarios. Blue crosses indicated the regular size sensor with 10X objective lens while black crosses indicated the miniaturized size sensor with 20X objective lens. The uncertainty of incident angles was assumed to be ±1 °. DO sensitivity was first increasing then decreasing with the incident angle of excitation according to the model and backed up by experimental results. More than 4 times increase of system sensitivity could be obtained when we optimized the incident angle of excitation, from perpendicular excitation in previous literature to 35 °incident angle in our sensor structure.

When the system was settled with certain incident angle of excitation, emission intensities were recorded by the optical power meter at different DO concentration. Nitrogen (99.9999% pure) and oxygen gas (99.9999% pure) were added to deionized water to tune DO concentration, which was then calibrated by a commercialized optical DO sensor (Model U-2000, Horiba, Japan) before injection. For sensitivity assessment in our sensors, a complete set of data consist of the emission intensities at a series of DO concentrations; these data points could then generate a regression line in Stern-Volmer plot and the slope of this line indicated Stern-Volmer quenching constant. For both the cases of regular size and miniaturized size, three different sensors were fabricated with exactly the same fabrication process and parameters; five cycles of DO concentration change (increasing sequence of DO concentration) were recorded in each of the sensor in experiments. Thus for every single incident angle and for each size, a total of 15 set of data coming from three different sensors were recorded. The average number of the 15 sets of data was used for the study of DO sensitivity here, while a much more detailed statistical analysis on these data would be shown in Section 4.4 as an estimation of sensor accuracy.

As a basic tool in fluorescence quenching, Stern-Volmer equation served as the platform for sensitivity assessment in this work. As what we mentioned in previous chapters, the ratio between the emission intensities in the absence and in the presence of oxygen was supposed to be in proportion to DO concentration. The sensitivity of the DO sensor was therefore represented by the slope of Stern-Volmer plot in which Y-axis was the ratio and X-axis was DO concentration. Experimental results of the sensor performance on different incident angles in the regular sized and in the miniaturized sensors were presented respectively in Figure 4.7, with horizontal and vertical errorbars on every datum point shown in the pictures.

As we saw from Figure 4.7, different incident angles led to different sensitivities, which were shown by the slope of each line. This was resulted from the different total-internal-reflected light pathways in the sensor at different angles, which influenced the absorption efficiency of the fluorophores. The reason for this had been elaborated in Chapter 3. DO sensitivity reached the largest when the incident angle was 35 ° in both sizes of sensors. Other incident angles could be sequenced in the decreasing order of sensitivity as 45 °, 55 °, 25 ° and 15 °, which corresponded to the model results. Differences in the sensitivities between the regular sized and miniaturized sensors were also observed, which was derived from the different cone angles of excitation in the two cases, as we used two objective lenses.

If we took the slope in the Stern-Volmer plot as the experimental DO sensitivity in certain scenario, we can compare the experimental data with the relative sensitivity in the model results in Chapter 3. A coefficient 0.064 was determined if we matched the experimental sensitivity 0.0473 of the regular sized sensor at 35 °incident angle with its relative sensitivity in the model (this angle was chosen as it led the highest sensitivity). By using this coefficient all the sensitivities we obtained in Figure 4.13 (including both the regular sized sensor and the miniaturized sensor) could be converted and drawn in the model curve, as shown in Figure 4.8. Blue crosses indicated the regular sized sensor with 10X objective lens while black crosses indicated the miniaturized sensor with 20X objective lens. The uncertainty of the incident angles was assumed to be ± 1 °. The system absorption rate was first increasing then decreasing with the incident angle of excitation, according to the model and backed up by experimental results. With the fact that we only used one coefficient for both the regular sized and the miniaturized sensors (which represented different cone angles of excitation), good matches were still observed between experimental and model results, validating the model on incident and cone angle of excitation. More than 4 times increase of system sensitivity could be obtained when we optimized the excitation method, from perpendicular excitation in previous literature to 35 °incident angle in our sensor structure.

4.3.2 Fluorophore film thickness

According to the model in Section 3.3, fluorophore film thicknesses had a big impact on DO sensitivity. A thicker fluorophore film could have a lower sensitivity compared with their thinner counterparts. We would study experimentally the influences of fluorophore film thickness in this section.

DO sensors with 7 different fluorophore film thicknesses were fabricated, and the fluorophore film thickness was 1 μm, 10 μm, 20 μm, 50 μm, 70 μm, 100 μm and 300 μm respectively, as verified by scanning electron microscopy (SEM) tests with a upper-limit resolution 50 nm. Because the fluorophore film was spin-coated on the glass slide in DO sensors, same thickness of the fluorophore film was controlled by the same spin rate in this process.

In characterization experiments, we discovered that the emission intensities from the 1 μm fluorophore film was so unstable that it almost lost all of its emission power at the beginning of operation, as what we described in Section 4.2.5. Thus the sensors with 1 μm thickness were excluded in the analysis hereafter. Regular sized sensors were fabricated for all other fluorophore film thicknesses; 10X objective lens and 45 °incident angle were used for easier control; detection length of emission was set to be 25.4 mm (1 inch). The Stern-Volmer plot of these DO sensors was shown in Figure 4.9.

Among the fluorophore film thicknesses we characterized for sensitivity, 10 μm case reached the highest value, which corresponded to our model result in Section 3.3. Concisely speaking, the oxygen quenching efficiency was diffusion limited and thicker fluorophore films led to greatly reduced oxygen diffusion. In the model in Section 3.3 we assumed two kinds of fluorophores, one with full accessibility to oxygen and the other with partial accessibility in deeper layer of the fluorophore film; a general hyperbolic relationship was predicted between DO sensitivity and the thickness of fluorophore film. If we used the experimental sensitivities in 10 μm and 20 μm cases to calculate the two parameters, namely optimum

thickness d_0 and constant ratio k, in the model, a theoretical result of the thickness dependency could be obtained for this sensor. Figure 4.10 compared the experimental and model sensitivities and good matches were observed. We could see that more than 7 times enhancement could be targeted when we optimized the fluorophore film thickness, reducing it from several hundred to 10 μm.

Stern-Volmer Plot of Sensors with Different Fluorophore Film Thicknesses
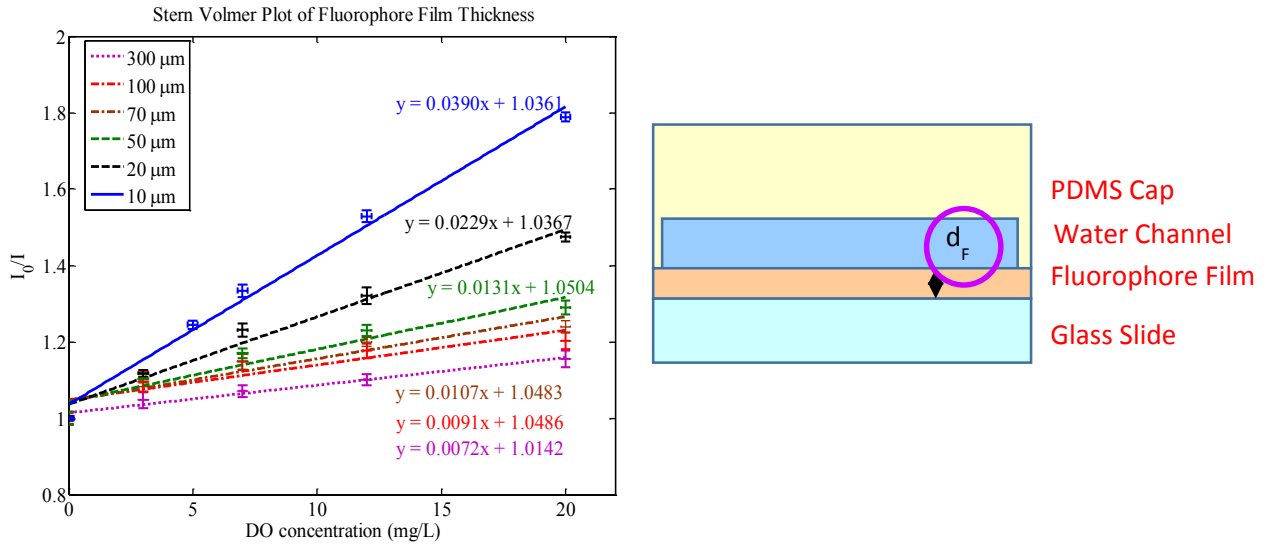
Figure 4.9 (left) Stern-Volmer Plot on different fluorophore film thicknesses and (right) the schematic of how the fluorophore film thickness was defined in the sensor. 6 different cases of film thickness were included. The horizontal errorbars were set to be 0.2 ppm which was the accuracy of the calibrator DO sensor. The vertical errorbars were the standard deviation of repetitive experiments. Among these thicknesses we tested, 10 μm reached the highest sensitivity. This was due to the oxygen quenching efficiency was diffusion limited and oxygen diffusion was greatly reduced in thicker cases.

Comparison between Experimental and Model Results on Different Fluorophore Film Thicknesses
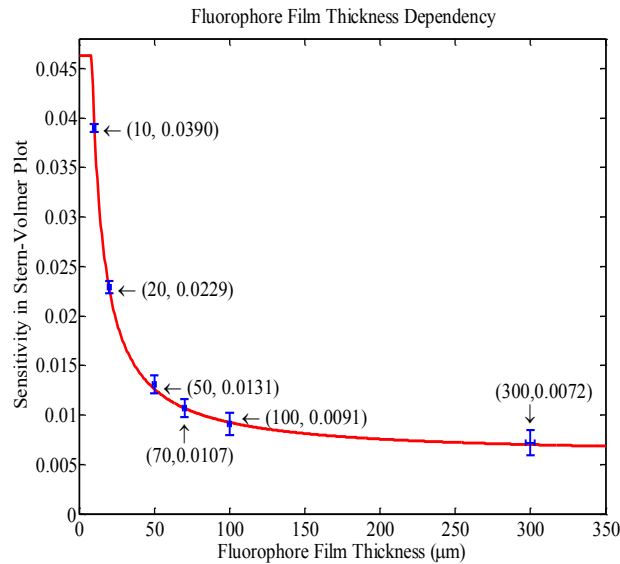

Figure 4.10 Comparison between experimental and model results on different fluorophore film thicknesses. According to the model, a very thin part of the fluorophore layer that was in a closer distance to the water channel (oxygen molecules) showed much greater sensitivity to oxygen than other parts of the fluorophore layer. There were two arbitrary numbers existing in the model so we used the experimental results at 10 μm and 20 μm to calibrate them; the other results at various thicknesses showed good matches with modeling. We could see that more than 7 times enhancement could be targeted when optimizing the fluorophore film thickness.

4.3.3 PDMS buffer layer

In Section 4.2.5 the emission power loss phenomenon of newly fabricated sensors was depicted. This sensitivity reduction at the beginning of operation necessitated a 'shower' for more repeatable measurements. It is presumed that this intensity loss was derived from the wash away of unstable fluorophores in the polymer by flowing water. In the light of this, it is proposed that a PDMS buffer layer could be introduced between the water channel and the fluorophore film, which may act as an isolator to protect the fluorophores from being washed away.

1 μm or 10 μm thickness of pure PDMS was spin-coated on top of the 10 μm fluorophore film in a regular sized sensor (the schematic shown in Figure 4.11). 10X objective lens and 45 °incident angle were chosen for easier control and the detection length of emission light was set to be 25.4 mm (1 inch). The emission power change together with DO sensitivity in stable state was shown in Figure 4.11. Based on the results, 1 μm PDMS buffer layer presented minimal sensitivity reduction compared with the sensor without the buffer layer, but the newly fabricated sensor still showed emission power loss; on the other hand, 10 μm PDMS buffer layer showed constant emission even in the initial stage, but its sensitivity was greatly reduced compared with the sensor without the buffer. Although 10 μm PDMS buffer layer seemed successfully protect the fluorophore layer from water flowing, the dramatic drop in sensitivity mitigated the sensitivity enhancement efforts in this design.

Reasons for the sensitivity drop in 10 μm buffer sensor could be conceived in terms of oxygen diffusion. This buffer layer made fluorophores at a longer diffusional distance towards the oxygen molecules in the

testing water, and this physical separation between the fluorophores and quenchers lowered the sensitivity of the device. Just like the way that a thicker fluorophore film may perform, diffusion limited oxygen encountered bigger problems in successful quenching of fluorophores in a sensor with a buffer layer. Due to the fact that the primary goal of this work is to increase oxygen sensitivity, the method of buffer layer to reduce the emission power in this project is aborted due to the loss of oxygen sensitivity.

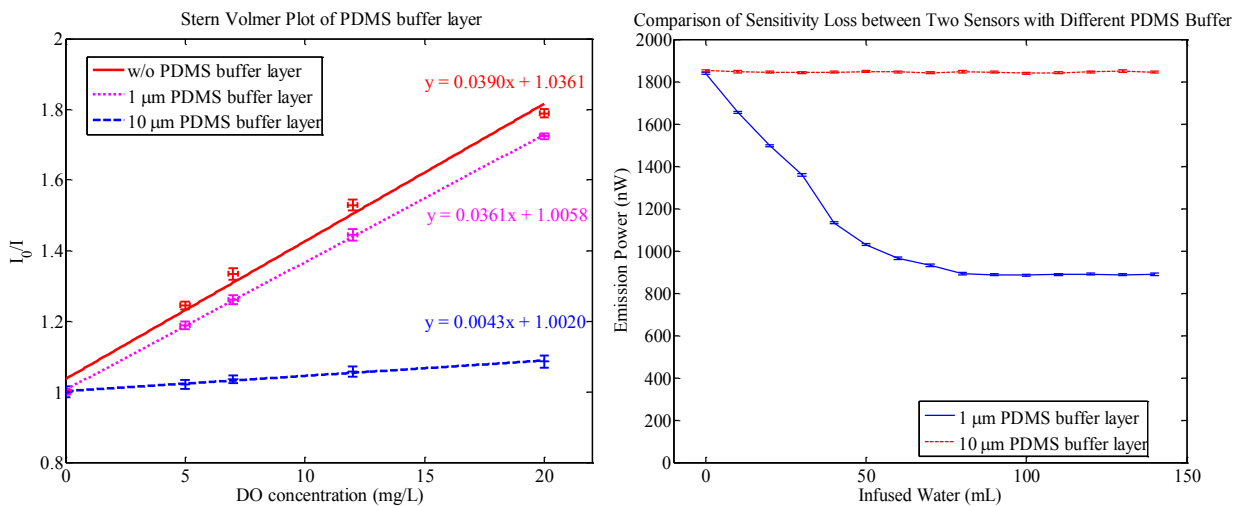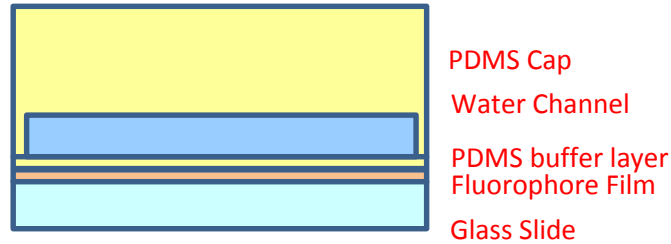**Experimental Characterization on Sensors with PDMS Buffer Layers**

Figure 4.11 (above) The schematic of PDMS buffer layer in DO sensor,(bottom left) Stern-Volmer plot on different PDMS buffer layers in stable state and (bottom right) the emission power changes on different PDMS buffer layers. According to previous experiments, sensitivity loss was observed in newly fabricated sensors, because of the wash away of fluorophores by flowing water in the channel. In this experiment we fabricated DO sensors with 1 μm and 10 μm PDMS buffer layer and tested their sensitivities and losses of emission power. 1 μm PDMS buffer layer presented minimal sensitivity reduction in stable state compared with the sensor without the buffer layer, but the newly fabricated sensors still showed emission power loss; on the other hand, 10 μm PDMS buffer layer showed consistent emission intensity even in the initial stage, but their sensitivity was greatly reduced compared with sensors without the buffer.

4.3.4 Aluminum reflective film

Aluminum film has been proposed many times in this work for the reflection of excitation and/or emission inside the DO sensors. An Aluminum reflective film could be sputtered at the bottom of the

glass slide substrate to enhance the emission collection efficiency, as we modelled in Section 3.3. The purpose of this section was to test whether this Al film would influence DO sensitivity.

200 nm Aluminum film was first sputtered on the glass slide and then this glass slide was used as the substrate for a DO sensor, with the metal coated side facing down (a schematic shown in Figure 4.12). Regular sized sensors were fabricated and 10X objective lens and 45 °incident angle were chosen for easier control; the detection length of emission was set to be 25.4 mm (1 inch). Enhancement of the collected intensity in the Al reflective sensor was easily observed: the intensity readout of water with no oxygen reached 1577 nW from 789 nW (in the sensor without such film), whose emission intensity nearly doubled. However, when we further compared DO sensitivity of the two kinds of sensors, similar performances were observed as shown in Figure 4.12, which implied that the Al reflective film failed to enhance DO sensitivity.

Experimental Characterization on Sensors with Al Reflective Film
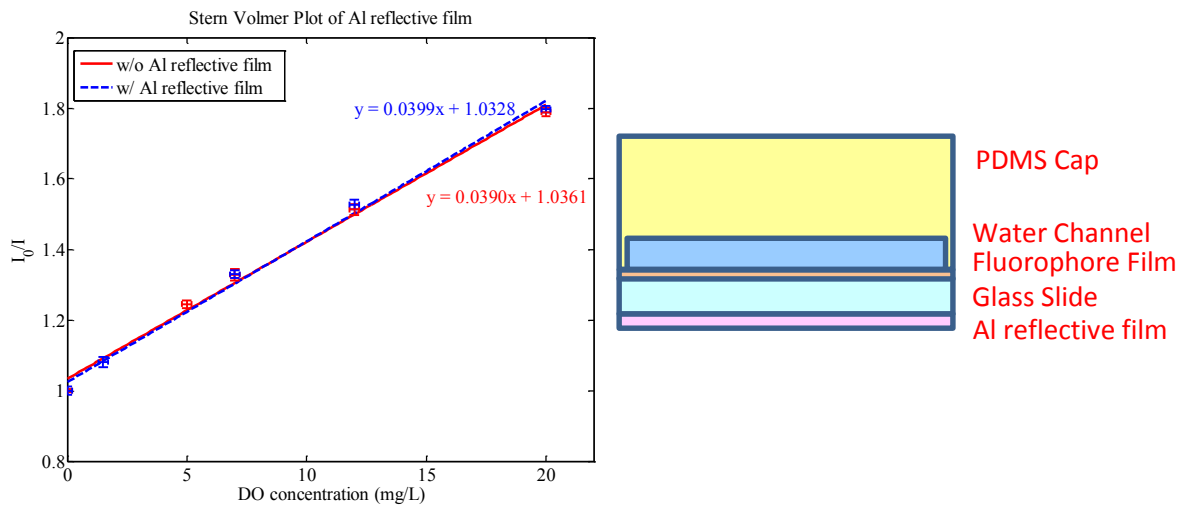

Figure 4.12 (left) Stern-Volmer plot of DO sensors with and without Al reflective film at the bottom of sensor structure and (right) the schematic of the sensor structure with Al reflective film at the bottom of the sensor. Doubled emission intensity was observed with the Al film while the system sensitivity remained the same.

Reasons for this could be traced back by the absorption efficiency of fluorophores. The Al film did not change the amount of excitation light being absorbed by the fluorophores (because TIR of excitation at the bottom of glass slide already existed in sensors without Al film); this absorption value, however, determined DO sensitivity in our configuration. What the Al film changed was just the detectable proportion of the emission light. It doubled the emission intensity readout in the optical power meter but did not influence sensor principle. In other words, it increased the optical noise level as well as the signal level, so signal/noise ratio (SN ratio) remained the same. Thus based on the results in this section, the function of an Al film at the bottom of DO sensors is understood: it would double the collected emission intensity at the same DO sensitivity of the sensor.

4.4 Estimation of sensor accuracy

In Section 4.3.1, it was mentioned that 15 sets of data were collected corresponding to the same incident angle. Three different sensors were fabricated and tested under the same conditions and five cycles of DO concentration were recorded in each sensor. By analyzing these data statistically, we would be able to learn the accuracy of DO sensing in current system setup. This analysis was of great value since it demonstrated to what degree our sensing results could be trusted, though this analysis was scarcely mentioned in previous literature.

The collected emission intensities between different sensors varied largely. Take the condition in the absence of oxygen as an example. The emission intensity readouts from different sensors (with the same fabrication parameters and system setup) could range from 700 nW to 2000 nW, which made it necessary for a calibration process on every single device. This variance among different sensors was derived from a number of reasons, including the alignment between the excitation light and the glass substrate and/or multifarious scattering and emission light loss processes (e.g. due to air bubbles in PDMS water channel cap). We also found this individual calibration of each sensor to be quite common in commercially available fluorescence based DO sensing systems [90] [91].

That being said, a device-to-device discrepancy in the DO sensitivity (represented by the slope of lines in Stern-Volmer plot) was not obvious in our experiments. The standard deviation in the intensity ratio in Stern-Volmer plot was only ~1.2X bigger when we included all the data from different sensors compared with the single sensor case. The uncertainty including all sensors' data in Stern-Volmer plot was thus used to estimate the uncertainty of DO concentration. A reverse regression fit from Y to X axis would be performed as below.

95% confidence interval of the DO concentration was estimated on the case of 35 °incident angle, by a statistical analysis on the reverse regression fit. The method proposed by D. Finney [92] was employed here. This method was designed for situations when a regression curve was used to determine unknown x values from certain y, which was just our purpose: the emission intensity readouts (or its relative ratio) was used to determine the unknown DO concentration. In the light of this, this method was named the x-from-y estimate, and the DO confidence interval was represented by the distance between two hyperbolic curves (on the upper and lower side of the linear regression fit). The formula for the pair of hyperbolic functions was as follows [92].

$$y = y_c \pm t_{v,P} S_{yx} \sqrt{\frac{1}{n} + \frac{1}{N} + \frac{(x-\bar{x})^2}{S_{xx}}} \qquad (4\text{-}1)$$

where $S_{xx} = \sum_{i=1}^{N} x_i^2 - N\bar{x}^2$ and $S_{yx} = \sqrt{\frac{\sum_{i=1}^{N}(y_i - y_{ci})^2}{N-2}}$.

In the equations above, y_c was the estimated y value from the linear curve fitting, $t_{v,P}$ was the student's t distribution, *n* was the number of replications of y measurements for a particular x (in our case was 15) and *N* represented the number of sampling points in x axis (in our case was 6). The 95% confidence interval in the range of 0~5 ppm was shown in Figure 4.13. We saw that the results showed a 0.2 ppm uncertainty in the range, which could be summarized as the sensor accuracy *the larger of 0.2 ppm (mg/L) or 2%*. The x-from-y estimate also predicted a 0.2 ppm uncertainty near 10 ppm and a 0.4 ppm uncertainty near 20 ppm.

As mentioned before, very few academic works on optical DO sensing touched the accuracy of their measurements. Yet even compared with some of the commercially available fluorescence based DO sensors, the accuracy in our sensors (when system parameters were optimized) was still better than or

comparable to them. Commercially available Pasport [TM], WQ-FDO [TM], RINKO [TM], YSI [TM] ROX, Sea-Bird [TM] SBE 63 optical dissolved oxygen sensors have the accuracy of 0.6, 0.4, 0.4, 0.1, 0.1 ppm respectively [90] [91] [93] [94] [95]. Considering the fact that accuracy could be enhanced by the implementation of temperature calibration (this temperature module has been utilized by all of abovementioned commercial systems), the design and fabrication of our sensor enjoyed good competence in the state-of-the-art technology, at a greatly reduced cost.

95% confidence interval of DO concentration in 0~5 ppm
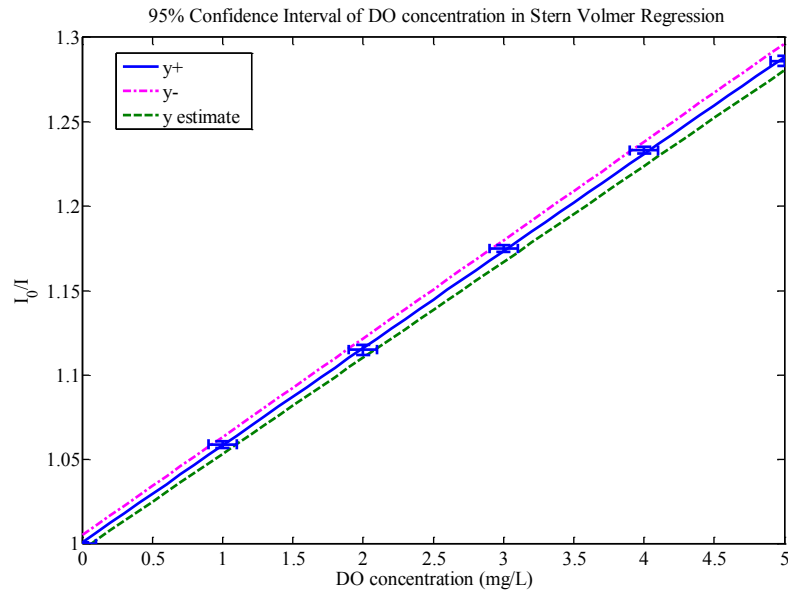
Figure 4.13 95% confidence interval of DO concentration in 0~5 ppm. The hyperbolic lines above and below the linear regression (y+ and y-) were used to estimate the accuracy of DO sensing. Making a horizontal line at certain relative intensity (parallel to the X-axis), the intercept between the lines y+ and y- was the 95% confidence interval for certain DO concentration. The accuracy was the larger of 0.2 ppm (mg/L) or 2%, which was comparable to commercially available sensors.

Chapter 5   Conclusion

In summary, we have developed a fluorescence quenching based dissolved oxygen sensor for environmental applications. Autonomous monitoring was realized and the reduction in cost/size was targeted for in the design. Total-internal-reflection was used to enhance DO sensitivity for the compensation of performance loss in miniaturized cost-friendly sensors. After theoretical and experimental explorations, the work demonstrated in this report clearly shows several achievements, from which we can draw the main conclusions in this project.

- Realized DO sensitivity enhancement, which was derived from
    - Total-internal-reflection design
    - Optimization of the incident angle of excitation (4X enhancement)
    - Optimization of the fluorophore film thickness (7X enhancement)
- Built 1st model on fluorescence based DO sensing on device scale, which contributed to a detailed performance analysis
- Accomplished sensor fabrication at a lower cost, thanks to the use of cost-friendly materials and soft lithography techniques
- Showed the possibility for great reduction in system expenses (from US $700 to US $30), enabled by the total-internal-reflection design where emission filter could be omitted and lowest-cost LED and photodiode could be used
- Paved way for system miniaturization, as the sensor was microfabricated and DO sensitivity was enhanced to work together with smaller-size reduced light sources and optical detectors in the system

Appendix 1   Source Code in Matlab Model

Fresnel Law
```
function [Reflection, RefractiveAngle]=FresnelLaw(n1, n2, Angle)
RefractiveAngle=asind(n1/n2*sind(Angle));
Rs=((n1*cosd(Angle)-n2*cosd(RefractiveAngle))/(n1*cosd(Angle)+n2*cosd(RefractiveAngle)))^2;
Rp=((n1*cosd(RefractiveAngle)-n2*cosd(Angle))/(n1*cosd(RefractiveAngle)+n2*cosd(Angle)))^2;
Reflection=(Rs+Rp)/2;
End
```

Absorption Rate in optofluidic DO sensing device based on Fresnel Law
```
function y=AbsorptionRateWithFresnelLaw_4Variables(ExcitationAngle,PDMSthickness,
DetectionWidth,GlassThickness)
FluoRefractiveIndex=1.41; % PDMS
PrependicularAbsorption1=-0.1273;
PrependicularAbsorption2=-0.1273;
QuantumEfficiency=0.064; %0.064 in experiment fitting of incident angle;
[R0,theta1]=FresnelLaw(1,1.52,ExcitationAngle);
y1=cosd(ExcitationAngle)*(1-R0)*QuantumEfficiency;
if ExcitationAngle<=34.5 %total reflection angle between glass and PDMS fluo layer 34.5910 degree
    d=450/4/pi*(1.52^2*cosd(theta1)^2-FluoRefractiveIndex^2)^(-0.5); %in original formular, sine
function is used by theta2
    A1=d/785;
    ExcitationSites=floor(DetectionWidth/cotd(theta1)/2/GlassThickness);
    Atotal=1-(1-A1)^ExcitationSites;
    y=Atotal*y1;
elseif (34.5<ExcitationAngle) && (ExcitationAngle <=47.4) % total reflection angle between water and
PDMS fluo layer is 47.3805 degree
    theta2=90-theta1;
    [R1,theta3]=FresnelLaw(1.52,FluoRefractiveIndex,theta2);
    MainRayLoss=(1-R1)^2*10^(2*PrependicularAbsorption1/cosd(theta3)); % equivalent to 0.7
    ExcitationSites=floor(DetectionWidth/cotd(theta1)/2/GlassThickness);
    a1=1-10^(2*PrependicularAbsorption1/cosd(theta3)); % equivalent to 0.3
    Asubtotal=a1*(1-MainRayLoss^ExcitationSites)/(1-MainRayLoss); %sum of geometric progression
    if DetectionWidth/cotd(theta1)/3/GlassThickness<1
        Aglass=0;
    else
        Aglass=a1*R1*(1-R1);
    end
    if DetectionWidth/cotd(theta1)/GlassThickness<1
        Afluo=0;
    else
        Afluo=a1*MainRayLoss*R1*(1-R1);
    end
    Atotal=Asubtotal+Aglass+Afluo;
    y=Atotal*y1;
elseif ExcitationAngle > 47.4 % total reflection angle between water and PDMS water channel cap
    theta2=90-theta1;
```

```
    [R1,theta3]=FresnelLaw(1.52,FluoRefractiveIndex,theta2);
    [R2,theta4]=FresnelLaw(FluoRefractiveIndex,1.33,theta3);
    MainRayLoss=(1-R1)*(1-R2)^2*10^(PrependicularAbsorption2/cosd(theta3));

ExcitationSites=floor(DetectionWidth/(2*cotd(theta1)*GlassThickness+2*tand(theta3)*PDMSthickness))
*2+floor(rem(DetectionWidth,2*cotd(theta1)*GlassThickness+2*tand(theta3)*PDMSthickness)/(2*cotd(
theta1)*GlassThickness));
    a1=1-10^(PrependicularAbsorption2/cosd(theta3));
    Asubtotal=a1*(1-MainRayLoss^ExcitationSites)/(1-MainRayLoss);
    if DetectionWidth/cotd(theta1)/3/GlassThickness<1
        Aglass=0; %
    else
        Aglass=a1*R1*(1-R1);
    end
    if DetectionWidth/cotd(theta1)/GlassThickness<1
        Afluo=0;
    else
        Afluo=a1*R2*(1-R1)+a1*MainRayLoss*R1*R2*(1-R1)+a1*MainRayLoss*R2*(1-R1)^3;
    end
    if DetectionWidth/cotd(theta1)/GlassThickness<1
        Awater=0;
    else
        Awater=a1*MainRayLoss*R2*(1-R1)*(1-R2)^2;
    end
    Atotal=Asubtotal+Aglass+Afluo+Awater;
    y=Atotal*y1;
else
    y=0;
end
end
```

Incident Angle Test of Absorption Rate
```
clear all; close all; clc;

x=0:0.5:76;   % define angle steps for x;
% x1=0.1:0.01:6; % define PDMSthickness steps for x1, water channel thickness 100 um
y=ones(numel(x),1); % make y array the same size as the number of x
z=ones(numel(x),1);  % for cone angle 2 degree
a=ones(numel(x),1);
b=ones(numel(x),1);
c=ones(numel(x),1);
% a=0*(0.1:0.01:6);

for i=1:numel(x)
    y(i)=AbsorptionRateWithFresnelLaw_4Variables(x(i),3,25.4,1);   % apply function to each x value to
generate y value
end;

z=y;
a=y;
b=y;
```

```
c=y;
%a=y;

   for i=3:numel(x)-2
     z(i)=1/6*(y(i-2)+y(i-1)+2*y(i)+y(i+1)+y(i+2));  %average between half angle 1 degrees, regarded as
collimated beam
   end;


   for i=16:numel(x)-15
     a(i)=1*(0.0072*y(i-15)+0.0093*y(i-14)+0.0119*y(i-13)+0.0148*y(i-12)+0.0182*y(i-
11)+0.0219*y(i-10)+0.0259*y(i-9)+0.0301*y(i-8)+0.0344*y(i-7)+0.0386*y(i-6)+0.0426*y(i-
5)+0.0461*y(i-4)+0.0491*y(i-3)+0.0513*y(i-2)+0.0527*y(i-
1)+0.0918*y(i)+0.0527*y(i+1)+0.0513*y(i+2)+0.0491*y(i+3)+0.0461*y(i+4)+0.0426*y(i+5)+0.0386*y(
i+6)+0.0344*y(i+7)+0.0301*y(i+8)+0.0259*y(i+9)+0.0219*y(i+10)+0.0182*y(i+11)+0.0148*y(i+12)+0.
0119*y(i+13)+0.0093*y(i+14)+0.0072*y(i+15));  %average between half angle 7.5 degrees, regarded as
collimated beam
   end;


   for i=8:numel(x)-7
     b(i)=1*(0.0188*y(i-7)+0.0297*y(i-6)+0.0438*y(i-5)+0.0603*y(i-4)+0.0772*y(i-3)+0.0921*y(i-
2)+0.1024*y(i-
1)+0.1514*y(i)+0.1024*y(i+1)+0.0921*y(i+2)+0.0772*y(i+3)+0.0603*y(i+4)+0.0438*y(i+5)+0.0297*y(
i+6)+0.0188*y(i+7));  %average between half angle 3.5 degrees
   end;

for i=31:numel(x)-30
  c(i)=1*(0.0035*y(i-30)+0.0041*y(i-29)+0.0047*y(i-28)+0.0053*y(i-27)+0.0059*y(i-26)+0.0066*y(i-
25)+0.0074*y(i-24)+0.0082*y(i-23)+0.0091*y(i-22)+0.01*y(i-21)+0.0109*y(i-20)+0.0119*y(i-
19)+0.0129*y(i-18)+0.014*y(i-17)+0.0151*y(i-16)+0.0161*y(i-15)+0.0172*y(i-14)+0.0183*y(i-
13)+0.0193*y(i-12)+0.0203*y(i-11)+0.0213*y(i-10)+0.0222*y(i-9)+0.0231*y(i-8)+0.0238*y(i-
7)+0.0245*y(i-6)+0.0252*y(i-5)+0.0257*y(i-4)+0.0261*y(i-3)+0.0264*y(i-2)+0.0265*y(i-
1)+0.0686*y(i)+0.0035*y(i+30)+0.0041*y(i+29)+0.0047*y(i+28)+0.0053*y(i+27)+0.0059*y(i+26)+0.00
66*y(i+25)+0.0074*y(i+24)+0.0082*y(i+23)+0.0091*y(i+22)+0.01*y(i+21)+0.0109*y(i+20)+0.0119*y(i
+19)+0.0129*y(i+18)+0.014*y(i+17)+0.0151*y(i+16)+0.0161*y(i+15)+0.0172*y(i+14)+0.0183*y(i+13)
+0.0193*y(i+12)+0.0203*y(i+11)+0.0213*y(i+10)+0.0222*y(i+9)+0.0231*y(i+8)+0.0238*y(i+7)+0.024
5*y(i+6)+0.0252*y(i+5)+0.0257*y(i+4)+0.0261*y(i+3)+0.0264*y(i+2)+0.0265*y(i+1)); % half cone
angle 15 degree
end;

x1=[15 25 35 45 55];
y1=[0.0139 0.0172 0.0476 0.0395 0.0343];
e1=[0.002 0.002 0.002 0.003 0.003];
y2=[0.0134 0.0206 0.0409 0.0397 0.0347];
e2=[0.002 0.002 0.002 0.003 0.003];
he=[1 1 1 1 1];
figure(2);
%plot(x,y,'g');
hold all;
box on;
```

```
% plot(x,b);
plot(x,z,'-r');% plot x vs z
 %contour3(z);
plot(x,b,':m');
plot(x,a,'-.g');
plot(x,c,'-c');

errorbar(x1,y1,e1,'b','linestyle','none');
herrorbar(x1,y1,he,'b');
errorbar(x1,y2,e2,'k','linestyle','none');
herrorbar(x1,y2,he,'k');
text(15,0.0137,' \downarrow ');
text(15,0.0137,'(15, 0.0139)');
text(15,0.0137,' \uparrow ');
text(15,0.0137,'(15, 0.0130)');

text(25,0.0168,' \leftarrow (25, 0.0172)');
text(25,0.0168,' \leftarrow (25, 0.0206)');
text(35,0.0473,' (35, 0.0476)  \rightarrow');
text(35,0.0473,' (35, 0.0409)  \rightarrow ');
text(45,0.0390,' \leftarrow (45, 0.0395)');
text(45,0.0390,' \leftarrow (45, 0.0397)');
text(55,0.0339,' \leftarrow (55,0.0343)');
text(55,0.0339,' \leftarrow (55, 0.0347)');


 title('Incident Angle Dependency with Cone Angle');

 xlabel('Incident Angle (degree)');

 ylabel('Relative Sensitivity');

 axis([0,80,0,0.063]);

legend('2X Lens (2 degree)','5X Lens (7 degree)','10X Lens (15 degree)','20X Lens (30 degree)');
```

Detection Length Test

```
clear all; close all; clc;
x=0:0.7:70;   % define angle steps for x;
y=zeros(numel(x),1); % make y array the same size as the number of x
z=zeros(numel(x),1);  % for cone angle 2 degree
a=zeros(numel(x),1);
b=zeros(numel(x),1);
c=zeros(numel(x),1);
d=zeros(numel(x),1);
e=zeros(numel(x),1);
f=zeros(numel(x),1);
g=zeros(numel(x),1);
h=zeros(numel(x),1);
% a=0*(0.1:0.01:6);
```

```matlab
    % 5 mm detection length
    for i=1:numel(x)
      y(i)=AbsorptionRateWithFresnelLaw_4Variables(x(i),3,5,1);   % apply function to each x value to
generate y value
    end;
    z=y;
    for i=3:numel(x)-2
      z(i)=1/6*(y(i-2)+y(i-1)+2*y(i)+y(i+1)+y(i+2)); %average between half angle 1 degrees, regarded as
collimated beam
    end;

    %10 mm detection length
    for i=1:numel(x)
      a(i)=AbsorptionRateWithFresnelLaw_4Variables(x(i),3,10,1);   % apply function to each x value to
generate y value
    end;
    b=a;
    for i=3:numel(x)-2
      b(i)=1/6*(a(i-2)+a(i-1)+2*a(i)+a(i+1)+a(i+2)); %average between half angle 1 degrees, regarded as
collimated beam
    end;


    % 20 mm detection length
    for i=1:numel(x)
      c(i)=AbsorptionRateWithFresnelLaw_4Variables(x(i),3,20,1);   % apply function to each x value to
generate y value
    end;
    d=c;
    for i=3:numel(x)-2
      d(i)=1/6*(c(i-2)+c(i-1)+2*c(i)+c(i+1)+c(i+2)); %average between half angle 1 degrees, regarded as
collimated beam
    end;

    %30 mm detection length
    for i=1:numel(x)
      e(i)=AbsorptionRateWithFresnelLaw_4Variables(x(i),3,30,1);   % apply function to each x value to
generate y value
    end;
    f=e;
    for i=3:numel(x)-2
      f(i)=1/6*(e(i-2)+e(i-1)+2*e(i)+e(i+1)+e(i+2)); %average between half angle 1 degrees, regarded as
collimated beam
    end;

    %40 mm detection length
    for i=1:numel(x)
      g(i)=AbsorptionRateWithFresnelLaw_4Variables(x(i),3,40,1);   % apply function to each x value to
generate y value
    end;
    h=g;
```

```
    for i=3:numel(x)-2
       h(i)=1/6*(g(i-2)+g(i-1)+2*g(i)+g(i+1)+g(i+2));  %average between half angle 1 degrees, regarded as
collimated beam
    end;

figure;
plot(x,y,'g');
hold all;
plot(x,z,'-r');
plot(x,b,'--g');
plot(x,d,':b');
plot(x,f,'-c');
plot(x,h,'-k');
box on;

title('Incident Angle Dependency with Detection Length');

xlabel('Incident Angle (degree)');

 ylabel('Relative Sensitivity');

 axis([0,80,0,1]);

%legend('Cone Angle 2 Degree','Cone Angle 7 Degree','Cone Angle 15 Degree','Cone Angle 30 Degree');

legend('Detection Length 5 mm', 'Detection Length 10 mm', 'Detection Length 20 mm', 'Detection Length
30 mm', 'Detection Length 40 mm');
```

Glass Thickness Test
```
clear all; close all; clc;

x=0:0.5:76;   % define angle steps for x;
y=ones(numel(x),1); % make y array the same size as the number of x
z=ones(numel(x),1);  % for cone angle 2 degree
a=ones(numel(x),1);
b=ones(numel(x),1);
c=ones(numel(x),1);
d=ones(numel(x),1);
e=ones(numel(x),1);
f=ones(numel(x),1);

% 1 mm PDMS thickness
for i=1:numel(x)
   y(i)=AbsorptionRateWithFresnelLaw_4Variables(x(i),1,25.4,1);   % apply function to each x value to
generate y value
end;
z=y;
for i=3:numel(x)-2
   z(i)=1/6*(y(i-2)+y(i-1)+2*y(i)+y(i+1)+y(i+2));  %average between half angle 1 degrees, regarded as
collimated beam
end;
```

```
%3 mm PDMS thickness
for i=1:numel(x)
    a(i)=AbsorptionRateWithFresnelLaw_4Variables(x(i),3,25.4,1);   % apply function to each x value to
generate y value
end;
b=a;
for i=3:numel(x)-2
    b(i)=1/6*(a(i-2)+a(i-1)+2*a(i)+a(i+1)+a(i+2));  %average between half angle 1 degrees, regarded as
collimated beam
end;

% 5 mm PDMS thickness
for i=1:numel(x)
    c(i)=AbsorptionRateWithFresnelLaw_4Variables(x(i),5,25.4,1);   % apply function to each x value to
generate y value
end;
d=c;
for i=3:numel(x)-2
    d(i)=1/6*(c(i-2)+c(i-1)+2*c(i)+c(i+1)+c(i+2));  %average between half angle 1 degrees, regarded as
collimated beam
end;

figure;
hold all;
plot(x,z,'-r');
plot(x,b,'--g');
plot(x,d,':b');

box on;
title('Incident Angle Dependency with PDMS Cap Thickness');
xlabel('Incident Angle (degree)');
ylabel('Relative Sensitivity');
legend('PDMS Thickness 1 mm', 'PDMS Thickness 3 mm', 'PDMS Thickness 5 mm');
```

Glass Thickness Test
```
clear all; close all; clc;

x=0:0.5:76;   % define angle steps for x;
y=ones(numel(x),1); % make y array the same size as the number of x
z=ones(numel(x),1);  % for cone angle 2 degree
a=ones(numel(x),1);
b=ones(numel(x),1);
c=ones(numel(x),1);
d=ones(numel(x),1);
e=ones(numel(x),1);
f=ones(numel(x),1);
g=ones(numel(x),1);
h=ones(numel(x),1);

% 0.3 mm glass thickness
```

```
for i=1:numel(x)
    y(i)=AbsorptionRateWithFresnelLaw_4Variables(x(i),3,25.4,0.3);   % apply function to each x value to
generate y value
end;
z=y;
for i=3:numel(x)-2
    z(i)=1/6*(y(i-2)+y(i-1)+2*y(i)+y(i+1)+y(i+2));  %average between half angle 1 degrees, regarded as
collimated beam
end;

% 1 mm glass thickness
for i=1:numel(x)
    a(i)=AbsorptionRateWithFresnelLaw_4Variables(x(i),3,25.4,1.0);   % apply function to each x value to
generate y value
end;
b=a;
for i=3:numel(x)-2
    b(i)=1/6*(a(i-2)+a(i-1)+2*a(i)+a(i+1)+a(i+2));  %average between half angle 1 degrees, regarded as
collimated beam
end;


% 3 mm detection length
for i=1:numel(x)
    c(i)=AbsorptionRateWithFresnelLaw_4Variables(x(i),3,25.4,3);   % apply function to each x value to
generate y value
end;
d=c;
for i=3:numel(x)-2
    d(i)=1/6*(c(i-2)+c(i-1)+2*c(i)+c(i+1)+c(i+2));  %average between half angle 1 degrees, regarded as
collimated beam
end;

figure;
hold all;
plot(x,z,'-r');
plot(x,b,'--g');
plot(x,d,':b');
box on;
title('Incident Angle Dependency with Glass Thickness');
xlabel('Incident Angle (degree)');
ylabel('Relative Sensitivity');
legend('Glass Thickness 0.3 mm', 'Glass Thickness 1 mm', 'Glass Thickness 3 mm');
```

Detector Position Test

```
clear all; close all; clc;  % Changing DetectorPosition is useful in all ExcitationAngle, but it may still
performs differently when smaller or greater than 34.5 degree
x=0:0.5:76;   % define angle steps for x;
DetectorWidth=10;
x1=-10:0.2:15; % detector postion is defined by the distance between the left edge of device and the left
edge of detector; 40 mm (water channel length) - 25.4 mm (1 inch detector)= 14.6 mm
```

```
y=ones(numel(x),numel(x1)); % make y array the same size as the number of x * x1
z=ones(numel(x),numel(x1));
b=ones(numel(x),numel(x1));
a=ones(numel(x1),1);
c=ones(numel(x1),1);
for i=1:numel(x)
    for j=1:numel(x1)
    if x1(j)<0
        y(i,j)=AbsorptionRateWithFresnelLaw_4Variables(x(i),3,x1(j)+DetectorWidth,1);
    else
y(i,j)=0.5*AbsorptionRateWithFresnelLaw_4Variables(x(i),3,x1(j)+DetectorWidth,1)+0.3*AbsorptionRa
teWithFresnelLaw_4Variables(x(i),3,x1(j)+DetectorWidth+0.1,1)+0.2*AbsorptionRateWithFresnelLaw_
4Variables(x(i),3,x1(j)+DetectorWidth+0.2,1)-
AbsorptionRateWithFresnelLaw_4Variables(x(i),3,x1(j),1);  % apply function to each x value to generate
y value
    end
    end;

end;

z=y;
b=y;
for j=1:numel(x1)
    for i=3:numel(x)-2
        z(i,j)=1/6*(y(i-2,j)+y(i-1,j)+2*y(i,j)+y(i+1,j)+y(i+2,j)); %average between half angle 1 degrees
    end;
end;

for j=1:numel(x1)
    for i=16:numel(x)-15
        b(i,j)=1*(0.0072*y(i-15,j)+0.0093*y(i-14,j)+0.0119*y(i-13,j)+0.0148*y(i-12,j)+0.0182*y(i-
11,j)+0.0219*y(i-10,j)+0.0259*y(i-9,j)+0.0301*y(i-8,j)+0.0344*y(i-7,j)+0.0386*y(i-6,j)+0.0426*y(i-
5,j)+0.0461*y(i-4,j)+0.0491*y(i-3,j)+0.0513*y(i-2,j)+0.0527*y(i-
1,j)+0.0918*y(i,j)+0.0527*y(i+1,j)+0.0513*y(i+2,j)+0.0491*y(i+3,j)+0.0461*y(i+4,j)+0.0426*y(i+5,j)+0
.0386*y(i+6,j)+0.0344*y(i+7,j)+0.0301*y(i+8,j)+0.0259*y(i+9,j)+0.0219*y(i+10,j)+0.0182*y(i+11,j)+0.
0148*y(i+12,j)+0.0119*y(i+13,j)+0.0093*y(i+14,j)+0.0072*y(i+15,j)); %average between half angle 1
degrees
    end;
end;

for j=1:numel(x1)  %find the largest absorption for every PDMSthickness in all ExcitationAngle
    a(j)=y(1,j);
    for i=2:numel(x)
        if a(j)<y(i,j)
            a(j)=y(i,j)
        end;
    end;
end;

for j=1:numel(x1)  %find the largest absorption for every PDMSthickness in all ExcitationAngle
    c(j)=b(1,j);
```

```
    for i=2:numel(x)
        if c(j)<b(i,j)
            c(j)=b(i,j)
        end;
    end;
end;
figure(1);
hold all;
plot(x1,a,'-r');
plot(x1,c,'--g');
box on;

title('Detector Position Dependency');

xlabel('Optical Detector Displacement (mm)');

ylabel('Relative Sensitivity');

axis([-10,15,0,1]);

legend('2X Lens (2 degree)','10X Lens (15 degree)');
```

Collection Efficiency Test
```
clear all; close all; clc;
 x=1:1:80; %Detection Width
 y=ones(numel(x),1);
 z=ones(numel(x),1);
 a=ones(numel(x),1);
 b=ones(numel(x),1);
 c=ones(numel(x),1);
 d=ones(numel(x),1);
 e=ones(numel(x),1);
 f=ones(numel(x),1);
 h=ones(numel(x),1);
 m=ones(numel(x),1);

for i=1:numel(x)
   [y(i),z(i)]=CollectionRate(3, x(i),1.41, 0);
end;

for i=1:numel(x)
   [a(i),b(i)]=CollectionRate(3, x(i),1.52,1);
end;

 for i=1:numel(x)
   [c(i),d(i)]=CollectionRate(3, x(i),1.41, 1);
end;

  for i=1:numel(x)
   [e(i),f(i)]=CollectionRate_Glass(1, x(i),1.41, 0);
end;
```

```
 for i=1:numel(x)
  [h(i),m(i)]=CollectionRate_Glass(1, x(i),1.41, 1);
end;

figure;
hold all;
plot(x,y,':b');
plot(x,a,'-.g');
plot(x,z,'-m');
plot(x,d,'-r');
plot(x,f,'-c');
plot(x,m,'-k');
```

Horizontal Displacement Test
```
clear all; close all; clc;
ChannelWidth=2;
sigma=0.265; % from experiment 0.365
normal=normcdf(ChannelWidth/2,0,sigma)-normcdf(-ChannelWidth/2,0, sigma);
x=-1:0.1:1;
y=(normcdf(ChannelWidth/2+x,0,sigma)-normcdf(-ChannelWidth/2+x,0,sigma))/normal;
figure;
plot(x,y);
axis([-1,1,0,1.02]);

 title('Horizontal Displacemnet Dependency');

 xlabel('Horizontal Displacement of Excitation (mm)');

 ylabel('Relative Sensitivity');
```

Skew Angle Test
```
clear all; close all; clc;
ChannelWidth=2;
sigma=0.265; % from experiment 0.365
DetectionWidth=10;
normal=normcdf(ChannelWidth/2,0,sigma)-normcdf(-ChannelWidth/2,0, sigma);
gamma=-10:0.1:10;%skew angle in degree
x=DetectionWidth*sind(gamma)/2;
y=(normcdf(ChannelWidth/2+x,0,sigma)-normcdf(-ChannelWidth/2+x,0,sigma))/normal;
figure;
plot(gamma,y);
axis([-10,10,0,1.02]);

 title('Skew Angle Dependency');

 xlabel('Skew Angle (degree)');

 ylabel('Relative Sensitivity');
```

Absorption Rate in Fluorophore Film Excitation Configuration

```matlab
function y=AbsorptionRateWithTIRinsideFluoLayer_7Variables(ExcitationAngle,PDMSthickness,
DetectionWidth,GlassThickness,FluoRefractiveIndex,BeamSize,FluoThickness)
% for PDMS, FluoRefractiveIndex is 1.41
PrependicularAbsorption1=-12.73;
%PrependicularAbsorption2=-13;
[R0,theta1]=FresnelLaw(1,FluoRefractiveIndex,ExcitationAngle);
theta2=90-theta1;
QuantumEfficiency=1;
y1=FluoThickness*cosd(ExcitationAngle)/BeamSize*(1-R0)*QuantumEfficiency; % apply to when
FluoThickness is less than or equal to BeamSize !!!!
if FluoRefractiveIndex>1.8195
    a1=1-10^(PrependicularAbsorption1*FluoThickness/cosd(theta2));
    ExcitationSites=floor(DetectionWidth/cotd(theta1)/FluoThickness);
    MainRayLoss=10^(PrependicularAbsorption1*FluoThickness/cosd(theta2));
    Atotal=a1*(1-MainRayLoss^ExcitationSites)/(1-MainRayLoss);
    y=Atotal*y1;
elseif (FluoRefractiveIndex<=1.8195) && (FluoRefractiveIndex>1.6640) %may pass into glass
    ThetaGlass=asind(1.52/FluoRefractiveIndex);
    if theta2>=ThetaGlass
        a1=1-10^(PrependicularAbsorption1*FluoThickness/cosd(theta2));
        ExcitationSites=floor(DetectionWidth/cotd(theta1)/FluoThickness);
        MainRayLoss=10^(PrependicularAbsorption1*FluoThickness/cosd(theta2));
        Atotal=a1*(1-MainRayLoss^ExcitationSites)/(1-MainRayLoss);
        y=Atotal*y1;
    else
        a1=1-10^(2*PrependicularAbsorption1*FluoThickness/cosd(theta2));
        [R1,theta3]=FresnelLaw(FluoRefractiveIndex, 1.52, theta2);
        MainRayLoss=10^(2*PrependicularAbsorption1*FluoThickness/cosd(theta2))*(1-R1);
        ExcitationSites=floor(DetectionWidth/2/GlassThickness/tand(theta3));
        Asubtotal=a1*(1-MainRayLoss^ExcitationSites)/(1-MainRayLoss);
        Afluo=R1*10^(2*PrependicularAbsorption1*FluoThickness/cosd(theta2))*a1*(1-
R1^(floor(DetectionWidth/2/FluoThickness/tand(theta2))-1))/(1-R1);
        Atotal=Asubtotal+Afluo;
        y=Atotal*y1;
    end
elseif (FluoRefractiveIndex<=1.6640) && (FluoRefractiveIndex>1.52)
    ThetaGlass=asind(1.52/FluoRefractiveIndex);
    ThetaWater=asind(1.33/FluoRefractiveIndex);
    if theta2>=ThetaGlass
        a1=1-10^(PrependicularAbsorption1*FluoThickness/cosd(theta2));
        ExcitationSites=floor(DetectionWidth/cotd(theta1)/FluoThickness);
        MainRayLoss=10^(PrependicularAbsorption1*FluoThickness/cosd(theta2));
        Atotal=a1*(1-MainRayLoss^ExcitationSites)/(1-MainRayLoss);
        y=Atotal*y1;
    elseif (theta2<ThetaGlass) && (theta2>=ThetaWater)
        a1=1-10^(2*PrependicularAbsorption1*FluoThickness/cosd(theta2));
        [R1,theta3]=FresnelLaw(FluoRefractiveIndex, 1.52, theta2);
        MainRayLoss=10^(2*PrependicularAbsorption1*FluoThickness/cosd(theta2))*(1-R1);
        ExcitationSites=floor(DetectionWidth/2/GlassThickness/tand(theta3));
        Asubtotal=a1*(1-MainRayLoss^ExcitationSites)/(1-MainRayLoss);
```

```
    Afluo=R1*10^(2*PrependicularAbsorption1*FluoThickness/cosd(theta2))*a1*(1-
R1^(floor(DetectionWidth/2/FluoThickness/tand(theta2))-1))/(1-R1);
    Atotal=Asubtotal+Afluo;
    y=Atotal*y1;
   else
     a1=1-10^(PrependicularAbsorption1*FluoThickness/cosd(theta2));
     [R1,theta3]=FresnelLaw(FluoRefractiveIndex, 1.52, theta2);
     [R2,theta4]=FresnelLaw(FluoRefractiveIndex, 1.33, theta2);
     [R3,theta5]=FresnelLaw(1.33,1.41,theta4);
     MainRayLoss=10^(PrependicularAbsorption1*FluoThickness/cosd(theta2))*(1-R1)*(1-R2)*(1-R3);

ExcitationSites=floor(DetectionWidth/(2*tand(theta3)*GlassThickness+2*tand(theta5)*PDMSthickness))
*2+floor(rem(DetectionWidth,2*tand(theta3)*GlassThickness+2*tand(theta5)*PDMSthickness)/(2*tand(
theta3)*GlassThickness));
     Asubtotal=a1*(1-MainRayLoss^ExcitationSites)/(1-MainRayLoss);

Afluo=R1*10^(PrependicularAbsorption1*FluoThickness/cosd(theta2))*(1+R2*10^(PrependicularAbsor
ption1*FluoThickness/cosd(theta2)))*a1*(1-
(R1*R2)^(floor(DetectionWidth/2/FluoThickness/tand(theta2))-1))/(1-R1*R2);
     Atotal=Asubtotal+Afluo;
     y=Atotal*y1;
   end
elseif (FluoRefractiveIndex<=1.52) && (FluoRefractiveIndex >1.33)
   ThetaWater=asind(1.33/FluoRefractiveIndex);
   if theta2>=ThetaWater
     a1=1-10^(2*PrependicularAbsorption1*FluoThickness/cosd(theta2));
     [R1,theta3]=FresnelLaw(FluoRefractiveIndex, 1.52, theta2);
     MainRayLoss=10^(2*PrependicularAbsorption1*FluoThickness/cosd(theta2))*(1-R1);
     ExcitationSites=floor(DetectionWidth/2/GlassThickness/tand(theta3));
     Asubtotal=a1*(1-MainRayLoss^ExcitationSites)/(1-MainRayLoss);
     Afluo=R1*10^(2*PrependicularAbsorption1*FluoThickness/cosd(theta2))*a1*(1-
R1^(floor(DetectionWidth/2/FluoThickness/tand(theta2))-1))/(1-R1);
     Atotal=Asubtotal+Afluo;
     y=Atotal*y1;
   else
     a1=1-10^(PrependicularAbsorption1*FluoThickness/cosd(theta2));
     [R1,theta3]=FresnelLaw(FluoRefractiveIndex, 1.52, theta2);
     [R2,theta4]=FresnelLaw(FluoRefractiveIndex, 1.33, theta2);
     [R3,theta5]=FresnelLaw(1.33,1.41,theta4);
     MainRayLoss=10^(PrependicularAbsorption1*FluoThickness/cosd(theta2))*(1-R1)*(1-R2)*(1-R3);

ExcitationSites=floor(DetectionWidth/(2*tand(theta3)*GlassThickness+2*tand(theta5)*PDMSthickness))
*2+floor(rem(DetectionWidth,2*tand(theta3)*GlassThickness+2*tand(theta5)*PDMSthickness)/(2*tand(
theta3)*GlassThickness));
     Asubtotal=a1*(1-MainRayLoss^ExcitationSites)/(1-MainRayLoss);

Afluo=R1*10^(PrependicularAbsorption1*FluoThickness/cosd(theta2))*(1+R2*10^(PrependicularAbsor
ption1*FluoThickness/cosd(theta2)))*a1*(1-
(R1*R2)^(floor(DetectionWidth/2/FluoThickness/tand(theta2))-1))/(1-R1*R2);
     Atotal=Asubtotal+Afluo;
     y=Atotal*y1;
```

```
        end
    else
        y=0;
    end
end
```

Beam Width Test in Fluorophore Film Excitation Configuration

```
clear all; close all; clc;  % Changing DetectionWidth is useful in all ExcitationAngle, but it may still
performs differently when smaller or greater than 34.5 degree

x=10:0.5:76;   % define angle steps for x;
x1=0.01:0.01:1;
y=ones(numel(x),numel(x1)); % make y array the same size as the number of x * x1
z=ones(numel(x),numel(x1));
b=ones(numel(x),numel(x1));
a=ones(numel(x1),1);
c=ones(numel(x1),1);

for i=1:numel(x)
    for j=1:numel(x1)
      y(i,j)=(x1(j)-
0.01)/x1(j)*AbsorptionRateWithFresnelLaw_4Variables(x(i),3,25.4,1)+AbsorptionRateWithTIRinsideFlu
oLayer_7Variables(x(i),3,25.4,1,1.41,x1(j),0.01); % apply function to each x value to generate y value
    end;

end;

z=y;
b=y;

for  j=1:numel(x1)
    for i=3:numel(x)-2
       z(i,j)=1/6*(y(i-2,j)+y(i-1,j)+2*y(i,j)+y(i+1,j)+y(i+2,j));  %average between half angle 1 degrees
    end;
end;

for  j=1:numel(x1)
    for i=16:numel(x)-15
       b(i,j)=1*(0.0072*y(i-15,j)+0.0093*y(i-14,j)+0.0119*y(i-13,j)+0.0148*y(i-12,j)+0.0182*y(i-
11,j)+0.0219*y(i-10,j)+0.0259*y(i-9,j)+0.0301*y(i-8,j)+0.0344*y(i-7,j)+0.0386*y(i-6,j)+0.0426*y(i-
5,j)+0.0461*y(i-4,j)+0.0491*y(i-3,j)+0.0513*y(i-2,j)+0.0527*y(i-
1,j)+0.0918*y(i,j)+0.0527*y(i+1,j)+0.0513*y(i+2,j)+0.0491*y(i+3,j)+0.0461*y(i+4,j)+0.0426*y(i+5,j)+0
.0386*y(i+6,j)+0.0344*y(i+7,j)+0.0301*y(i+8,j)+0.0259*y(i+9,j)+0.0219*y(i+10,j)+0.0182*y(i+11,j)+0.
0148*y(i+12,j)+0.0119*y(i+13,j)+0.0093*y(i+14,j)+0.0072*y(i+15,j));  %average between half angle 1
degrees
    end;
end;

for  j=1:numel(x1)  %find the largest absorption for every PDMSthickness in all ExcitationAngle
    a(j)=y(1,j);
    for i=2:numel(x)
```

```
    if a(j)<y(i,j)
        a(j)=y(i,j)
      end;
   end;
end;

for  j=1:numel(x1)  %find the largest absorption for every PDMSthickness in all ExcitationAngle
  c(j)=b(1,j);
   for i=2:numel(x)
     if c(j)<b(i,j)
        c(j)=b(i,j)
      end;
   end;
end;

figure;
hold all;
plot(x1,a,'r');
plot(x1,c,'--g');
box on;

title('Excitation Beam Size Dependency');

xlabel('Excitation Beam Size (mm)');

ylabel('Relative Emission Intensity');

axis([0,0.2,0,1]);

legend('2X Lens (2 degree)','10X Lens (15 degree)');
```

Fluorophore Film Thickness Model
```
clear all; close all; clc;

x=0:0.5:350;
y=ones(numel(x),4);
z=ones(numel(x),4); % make y array the same size as the number of x * x1
x0=[10 20 30 40];
fraction =[0.05 0.10 0.15 0.20];
for j=1:4
for i=1:numel(x)
if x(i)<= x0(1)
   y(i,j)=1;
else
   y(i,j)=x0(1)/x(i)+(x(i)-x0(1))/x(i)*fraction(j);
end;
end;
end;

for j=1:4
for i=1:numel(x)
```

```matlab
if x(i)<= x0(j)
  z(i,j)=1;
else
   z(i,j)=x0(j)/x(i)+(x(i)-x0(j))/x(i)*fraction(1);
end;
end;
end;


figure(1);
hold all;
plot(x,y(:,1),'r');
plot(x,y(:,2),':m');
plot(x,y(:,3),'--g');
plot(x,y(:,4),'-.c');
box on;
title('Fluorophore Film Thickness Dependency');

xlabel('Fluorophore Film Thickness (\mum)');

ylabel('Relative Sensitivity');

axis([0,350,0,1.05]);
legend('k=0.05','k=0.10','k=0.15','k=0.20');
text(10,0.39,' d0=10\mum');

figure(2);
hold all;
plot(x,z(:,1),'r');
plot(x,z(:,2),':m');
plot(x,z(:,3),'--g');
plot(x,z(:,4),'-.c');

box on;
title('Fluorophore Film Thickness Dependency');

xlabel('Fluorophore Film Thickness (\mum)');
```

Appendix 2   Purchase Links of System Components

All these items are listed in Table 4.1.

Laserland 450 nm blue diode laser (US $50)	https://item.taobao.com/item.htm?spm=a1z10.5-c.w4002-1241807667.18.sgWQ9Z&id=10473470157
LED as the light source in future choices (US $10)	https://item.taobao.com/item.htm?spm=a230r.1.14.64.KCjb6k&id=10849964504&ns=1&abbucket=2#detail
ZEISS 10X objective lens (US $30)	https://item.taobao.com/item.htm?spm=a230r.1.14.32.oru1KG&id=520521808872&ns=1&abbucket=2#detail
Single mode optical fiber in future choices (US $4)	http://world.tmall.com/item/39703376460.htm?spm=a230r.1.14.55.CjeSUw&id=39703376460&ns=1&abbucket=2
Semrock BrightLine^{TM} 609/181 bandpass filter (US $300)	http://www.semrock.com/FilterDetails.aspx?id=FF01-609/181-25
Edmund Optics OD 4 filter in future choices (US $25)	http://www.edmundoptics.com/optics/optical-filters/bandpass-filters/visible-bandpass-interference-filters/43081/
Newport 1830-C optical power meter (US $500)	http://www.ebay.ca/itm/Used-Newport-1830C-Optical-Power-Meter-W-818-IR-Detector-Calibration-Module-/271973197503?hash=item3f52dda6bf
Photodiode as the optical detector in future choices (US $10)	http://world.tmall.com/item/42125327367.htm?spm=a230r.1.14.6.Wi2PQo&id=42125327367&cm_id=140105335569ed55e27b&abbucket=2
Thorlab optical stage (US $70)	https://www.thorlabs.com/newgrouppage9.cfm?objectgroup_id=4271
Syringe (US $1)	https://www.thorlabs.com/newgrouppage9.cfm?objectgroup_id=4271

Bibliography

[1] H. Cheng, Y. Hu and J. Zhao, "Meeting china's water shortage crisis: current practices and challenges," *Environmental Science and technology,* pp. 43(2), 240, 2009.

[2] J. Xie, "Addressing China's water scarcity," *The world bank,* 2009.

[3] A. Ebenstein, "Water pollution and digestive cancers in China," *Research Gate,* 2008.

[4] R. Calderon, "The epidemiology of chemical contaminants of drinking water.," *Food and chemical toxicity,* p. 13, 2000.

[5] World Health Organization, "Fecal pollution and water quality," 2014.

[6] World Health Organization, "Water quality and health strategy," 2013.

[7] K. Hipel, "Risk analysis of the Walkerton drinking water crisis," *Canadian water resources journal,* p. 395, 2008.

[8] B. Pellerin, "Optical sensors for water quality," *Lakeline,* p. 13, 2014.

[9] L. Bengtsson, R. W. Herschy and R. W. Fairbridge, "Encyclopedia of lakes and reservoirs," *Springer Netherlands,* 2012.

[10] P. Chambers and T. Mills, "Dissolved oxygen conditions and fish requirements in the Athabasca, Peace and Slave rivers: assessment of present conditions and future trends," *Northern River Basins Study,* 1996.

[11] M. Hitchman, Measurement of dissolved oxygen, Wiley, 1978.

[12] B. Jones, "Oxygen-the most important water quality parameter?," *Water Column,* p. 1, 2011.

[13] J. Hargreaves, "Measuring dissolved oxygen in aquaculture," SRAC publication, 2002.

[14] Environment Canada, "Great Lakes Surveillance Program," [Online]. Available: http://www.ec.gc.ca/scitech/default.asp?lang=en&n=3F61CB56-1.

[15] Hamilton, City of, "Hamilton water and waste water treatment plant," [Online]. Available: https://www.hamilton.ca/NR/rdonlyres/A06A29EC-0A14-4BB6-9FA7-8F2F4613BDC5/0/WTPBrochure.pdf.

[16] P. Vanrollegham, "On-line monitoring equipment for waste water treatment processes: state of the art," *Water science and technology,* p. 1, 2003.

[17] Inc, Epcor Water Services, "2013 Wastewater treatment annual report," The province of Alberta, 2013.

[18] H. Tai, Y. Yang, S. Liu and D. Li, "A review of measurement methods of dissolved oxygen in water," *Computer and Computing Technologies in Agriculture V. IFIP Advances in Information and Communication Technology Volume 369,* pp. 569-576, 2012.

[19] J. Carpenter, "The accuracy of the Winkler method for dissolved oxygen analysis," *Limnology and oceanography,* p. 135, 1965.

[20] L. Hsu and P. R. Selvaganapathy, "Development of a low cost hemin-based dissolved oxygen sensor with anti-biofouling coating for water monitoring," *IEEE sensors Journal,* 2014..

[21] J. Lakowicz, Principles of fluorescence spectroscopy, Springer, 2006.

[22] E. Moreno, "Time resolved fluorescence spectroscopy with LabView," in *Modelling, programming and simulations using LabVIEW software*, 2001.

[23] Y. Amao, "Probes and polymers for optical sensing of oxygen," *Microchimica Acta,* pp. 1-12, 2003.

[24] R. Ramamoorthy, "Oxygen sensors: materials, methods, designs and applications," *Journal of materials science,* p. 4271, 2003.

[25] B. Cox, "A review of dissolved oxygen modeling techniques for lowland rivers," *The Science of the Total Environment,* p. 303–334, 2003.

[26] YSI, "The Dissolved Oxygen Handbook," 2010.

[27] S. M. Grist, L. Chrostowski and K. Chueng, "Optical sensors for applications in microfluidic cell culture," *Sensors,* pp. 10(10), 9286-9316, 2010.

[28] M. Willett, "Oxygen sensing for industrial safety – evolution and new approaches," *Sensors,* p. 6084, 2014.

[29] Y. Fainman, L. Lee and C. Yang, Optofluidics: fundamentals, devices and applications, McGraw-Hill, 2010.

[30] M. Qyaranta, S. Borisov and I. Klimant, "Indicators for optical oxygen sensors," *Bioanal Rev,* pp. 4, 115-157, 2012.

[31] A. Mills, "Optical oxygen sensors: utilizing the luminescence of platinum metals complexes," *Platinum metals review,* p. 115, 1997.

[32] E. Caraway, "Photophysics and photochemistry of oxygen sensors based on luminescent transition-metal complexes," *Analytical chemistry,* p. 337, 1991.

[33] C. Chu, "Review on recent developments of fluorescence oxygen and carbon dioxide optical fiber sensors," *Photonic sensors,* p. 234, 2011.

[34] S. Lamansky, "Highly Phosphorescent Bis-Cyclometalated Iridium Complexes: Synthesis, Photophysical Characterization, and Use in Organic Light Emitting Diodes," *JACS,* p. 4304, 2001.

[35] S. Kochmann, "Sensing and imaging of oxygen with parts per billion limits of detection and based on the quenching of the delayed fluorescence of (13)C70 fullerene in polymer hosts," *Analytical chemistry,* p. 1300, 2013.

[36] M. Anni, "Oxygen Optical Gas Sensing by Reversible Fluorescence Quenching in Photo-Oxidized Poly(9,9-dioctylfluorene) Thin Films," *Journal of physical chemistry,* p. 1559, 2010.

[37] K. Nagai, T. Masuda and T. Nakagawa, "Poly[1-(trimethylsilyl)-1-propyne] and related polymers: synthesis, properties and functions.," *Progress in polymer science,* vol. 26, p. 721, 2001.

[38] H. Hah, T. Sakai and K. Asai, "Synthesis of poly(ethynylplatinumporphyrin) and its application as an oxygen pressure-sensitive paint.," *Macromolecule symposium,* vol. 24, p. 27, 2003.

[39] D. Pradhan, R. Choudhary and B. Samantaray, "Effect of Plasticizer on Structural and Electrical Properties of Polymer Nanocompsoite Electrolytes.," *Internatioanl journal of electrochemical science,* vol. 2, p. 861, 2007.

[40] T. Okada, S. Nishijima, Y. Honda and Y. Kobayashi, "Physical properties of epoxy and free volume evaluated by positron annihilation spectroscopy," *Journal de Physique IV,* 1993.

[41] R. McFarlane and M. C. Hamilton, "A Fluorescence Based Dissolved Oxygen Sensor".*Fiber Optic Sensors II.*

[42] L. Shen, M. Ratterman, D. Klotzkin and I. Papautsky, "A CMOS optical detection system for point-of-use luminescent oxygen sensing," *Sensors and actuators B: Chemical,* vol. 155, p. 430, 2011.

[43] T. Yoshihara, Y. Yamaguchi and S. Tobita, "Ratiometric Molecular Sensor for Monitoring Oxygen Levels in Living Cells," *Angewandte Chemie International Edition,* vol. 51, no. 17, p. 4148, 2012.

[44] Y. Feng, J. Cheng, L. Zhou, X. Zhou and H. Xiang, "Ratiometric optical oxygen sensing: a review in respect of material design," *Analyst,* vol. 137, no. 21, p. 4885, 2012.

[45] A. Kocincova, S. Borisov, C. Krause and O. Wolfbeis, "Fiber-optic microsensors for simultaneous sensing of oxygen and pH, and of oxygen and temperature.," *Analytical chemistry,* vol. 79, no. 22, p. 8486, 2007.

[46] S. Borisov, R. Seifner and I. Klimant, "A novel planar optical sensor for simultaneous monitoring of oxygen, carbon dioxide, pH and temperature.," *Analytical Bioanalytical Chemistry,* vol. 400, p. 2463, 2011.

[47] S. Grant, J. Satcher and K. Bettencourt, "Development of sol-gel-based fiber optic nitrogen dioxide gas sensors.," *Sensors and Actuators B: Chemical,* vol. 69, no. 1, p. 132, 2000.

[48] E. Barra, "The liquid-mirror telescope as a viable astronomical tool," *Journal of the royal astronomical society of Canada,,* vol. 245, p. 76, 1982.

[49] D. Psaltis, S. Quake and C. Yang, "Developing optofluidic technology through the fusion of microfluidics and optics," *Nature,* vol. 442, p. 381, 2006.

[50] K. Lee, S. Yoon, K. Lee and S. Kim, "Optofluidic particle manipulation in a liquid-core/liquid-cladding waveguide. Optics express," *Optics Express,* vol. 20, no. 16, p. 17348, 2012.

[51] R. Reimann, W. Alt, T. Kampschulte, T. Macha, L. Ratschbacher, N. Thau, S. Yoon and D. Meschede., "Cavity-Modified Collective Rayleigh Scattering of Two Atoms," *Physical review letter,* vol. 114, p. 2, 2015.

[52] P.Rai-Choudhury, MEMS and MOEMS technology and applications., SPIE PRESS, 2010.

[53] C. Cohen-Tannoudj, "Manipulating atoms with photons," *Review of modern physics,* vol. 70, no. 3, 1998.

[54] B. Kuswandi, Nuriman, J. Huskens and W. Verboom, "Optical sensing systems for microfluidic devices: a review," *Analytica chimica acta,* vol. 601, pp. 141-155, 2007.

[55] K. Ro, K. Lim, B. Shim and J. Hahn, "Integrated Light Collimating System for Extended Optical-Path-Length Absorbance Detection in Microchip-Based Capillary Electrophoresis," *Analytical chemistry,* vol. 77, p. 5160, 2005.

[56] S. Lee, S. Cho, C. Lee, B. Kim and Y. Kim, "Microfluidic chip for biochemical reaction and electrophoretic separation by quantitative volume control," *Sensors and Actuators B,* vol. 110, p. 164, 2005.

[57] R. Su, J. Lin, F. Qu, Z. Chen, Y. Gao and M. Yamada, "Capillary electrophoresis microchip coupled with on-line chemiluminescence detection," *Analitica Chimica Acta,* vol. 508, p. 11, 2004.

[58] J. Wu and M. Gu, "Microfluidic sensing: state of the art fabrication and detection techniques," *Journal of Biomedical Optics,* vol. 16, no. 8, p. 080901, 2011.

[59] J. C. McDonalds and G.Whitesides, "Poly(dimethylsiloxane) as a material for fabricating microfluidic devices.," *Accounts of chemical research,* vol. 35, no. 7, p. 491, 2002.

[60] G. W. Y.Xia, "Soft lithography," *Annual review of materials science,* vol. 28, p. 153, 1998.

[61] J. Ng, I. Gitlin, A. Stroock and G. Whitesdies, "Components for integrated poly(demethylsiloxane) microfluidic systems.," *Electrophoresis,* vol. 23, no. 20, p. 3461, 2002.

[62] J. C. McDonalds, M. Chabinyc and G. Whitesides, "Prototyping of microfluidic devices in poly(demethylsiloxane) using solid-object printing.," *Analytical chemistry,* vol. 74, p. 1537, 2002.

[63] D. Chang-Yen and B. Gale, "An integrated optical oxygen sensor fabricated using rapid-prototyping techniques.," *Lab on a chip,* vol. 3, p. 297, 2003.

[64] B. G. G. Chang-Yen, "A novel integrated optical dissolved oxygen sensor for cell culture and micro total analysis systems.," in *MEMS*, Las Vegas, NV, 2002.

[65] D. B. Papkovsky, A. N. Ovchinnikov, V. I. Ogurtsov, G. V. Ponomarev and T. Korpela., "Biosensors on the basis of luminescent oxygen sensor: the use of microporous light-scattering support materials.," *Sensors and actuators B.,* vol. 51, p. 137, 1998.

[66] B. Han, I. Manners and M. Winnik, "Oxygen sensors based on mesoporous silica nanoparticles on layer-by-layer self-assembled films," *Chemical materials,* vol. 17, no. 12, p. 3160, 2005.

[67] C. Chu, Y. Lo and T. Sung, "Enhanced oxygen sensing properties of Pt(II) cpmplex an dye entrapped core-shell nanoparticles embedded in sol-gel matrix," *Talanta,* vol. 82, no. 3, p. 1044, 2005.

[68] A. B. Brennan and C. M. Kirschner, "Bio-inspired antifouling strategies," *Annu. Rev. Mater. Res.,* vol. 42, p. 211, 2012.

[69] C. Ho. and I. Wong, "Surface molecular property modifications for poly(dimethylsiloxane) (PDMS) based microfluidic devices.," *Microfluid Nanofluid,* vol. 7, p. 291, 2009.

[70] M. Rabe, D. Verdes and S. Seeger, "Understanding protein adsorption phenomena at solid surfaces.," *Advances in colloid and interface science,* vol. 162, p. 87, 2011.

[71] H. G. M. Awad, "Effect of surface temperature on the fouling of heat transfer surfaces.," in *Eleventh International Water Technology Conference, IWTC11*, Eygpt, 2007.

[72] H. Videla, "Biofouling and microbially influenced corrosion.," in *International biodeterioration and biodegradation*, 1992.

[73] C.Shan, "Progress of marine biofouling and antifouling technologies.," in *Chinese science bulletin*, 2011.

[74] M. Chen, "Structures and antifouling properties of low surface energy non-toxic antifouling coatings modified by nano-SiO2 powder," *Science in China, Series B: Chemistry,* vol. 51, p. 848, 2008.

[75] A. Zeyad, C. Ren and L. Simon, "Evaluation of polydimethylsiloxane (PDMS) surface modification approaches for microfluidic applications," *Colloids and Surfaces A: Physicochemical and Engineering Aspects,* vol. 415, p. 406, 2012.

[76] A.-M. Gu and P. Abgrall, "Lab-on-chip technologies: making a microfluidic network and coupling it into a complete microsystem—a review.," *Journal of Micromechanics and Microengineering,* vol. 17, 2007.

[77] M. Amiji and K. Park, "Prevention of protein adsorption and platelet-adhesion on surfaces by PEO PPO PEO triblock copolymers.," *Biomaterials,* vol. 13, p. 682, 1992.

[78] V. Barbier, M. Tatoulian and H. Li, "Stable modification of PDMS surface properties by plasma polymerization: Application to the formation of double emulsions in microfluidic systems.," *Langmiur,* vol. 22, no. 12, p. 5230, 2006.

[79] P. Dittrich, K. Tachitawa and A. Manz, "Micro total analysis systems. Latest advancements and trends.," *Analytical chemistry,* vol. 78, no. 12, p. 3887, 2006.

[80] D. Bodas and C. Khan-Malek, "Formation of more stable hydrophilic surfaces of PDMS by plasma and chemical treatments.," *Microelectronic engineering,* vol. 83, no. 4, p. 1277, 2006.

[81] H. Becker and C. Gartner, "Polymer microfabrication methods for microfluidic analytical applications," *Polymer microfabrication methods for microfluidic analytical applications,* vol. 21, no. 1, p. 12, 2000.

[82] A. Piruska, I. Nikcevic and S. Lee, "The autofluorescence of plastic materials and chips measured under laser irradiation," *Lab on a chip,* pp. 5(12),1348, 2005.

[83] A. E. Siegman., "How to (maybe) measure laser beam quality.," in *optical society of America annual meeting*, Long Beach, CA.

[84] G. Day and C. F.Stubenrauch, "Laser far-field beam-profiler measurements by the focal plane technique.," *NBS Technical Note 1001,* 1978.

[85] D. Axelrod., "Total internal reflection fluorescence microscopy in cell biology.," *Traffic,* vol. 2, p. 764, 2001.

[86] E. Park, K. Reid and R. Kopelman, "Ratiometric fiber optic sensors for the detection of inter- and intra-cellular dissolved oxygen.," *Journal of materials chemistry,* vol. 19, p. 2913, 2005.

[87] S. Ugur, O. Yargi and O. Pekcan., "Oxygen diffusion into polystyrene-bentonite films," *Applied clay science,* vol. 43, p. 447, 2009.

[88] O. Yargi, S. Ugur and O. Pekcan., "Diffusion energies of oxygen diffusing into polystyrene (PS)/poly (N-isopropylacrylamide) composites.," *Polymer advanced technologies,* vol. 23, p. 776, 2013.

[89] Horiba Handbook, " http://www.horiba.com/fileadmin/uploads/Process-Environmental/Documents/W-20XD_Literature.pdf".

[90] YSI Handbook , "http://www.ysi.com/media/pdfs/E32-6150-ROX-DO-Sensor.pdf".

[91] Sea-bird Handbook , "Sea-bird Handbook http://www.seabird.com/sbe63-optical-dissolved-oxygen-sensor".

[92] P. F. Dunn., Measurement and data analysis for engineering and science. 3rd edition, CRC press, 2014.

[93] Pasport Handbook, http://www.pasco.com/prodCatalog/PS/PS-2196_pasport-optical-dissolved-oxygen-sensor/index.cfm.

[94] WQ-FDO Handbook, http://www.globalw.com/downloads/WQ/WQ-FDOB.pdf.

[95] Rinko Handbook , http://www.rocklandocean.com/resources/RINKOsepc.pdf.

SIGMA-ALDRICH®

Request to Use Sigma-Aldrich Copyrighted Material

Part I – to be filled in by Requester:

Request Date   Apr 7 2015   Requester Signature   Du Fei

Requester Information:

Name	Fei Du	Building	ETB 303
Title	Miss	Street	1280 Main St. W.
Department	Biomedical Engineering	City	Hamilton
Organization	McMaster University	State	ON
Phone	289-237-3716	Zip Code	L8S 4L8
Email	duf5@mcmaster.ca	Country	Canada

Material Requested to be Used:

Form (check one)   ☐ Printed   ☑ Electronic

Source Publ. Name or URL   Please see the datasheet also in the attachment.

Source Publ. Edition _____   Source Publ. Issue _____

Source Publ. Year _____   Source Publ. Pages _____

Source Publ. Volume _____

Description of Material and the intended use (Submit a photocopy or screen image of the context in which the copyrighted material will be used)

What I proposed in my master degree thesis is a method to enhance the sensitivity of optical dissolved oxygen sensing. I used your product 76886 as the fluorophore. Excerpt including the use of spectra information the product in my thesis is included in the attachment.
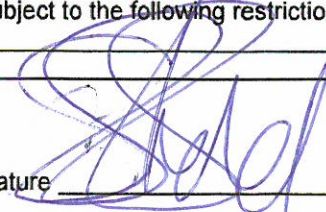
Type of Use (check one)   ☐ For Profit   ☑ Not for Profit

If Material will be reproduced, how many copies will be made? 2 _____

Part II – to be filled in by Sigma-Aldrich Authorizer

Sigma-Aldrich Co. LLC hereby grants permission for one-time use of the material described above for the purpose stated,

- provided a suitable acknowledgment is given, e.g., "Reproduced with permission from Sigma-Aldrich Co. LLC" or "Reproduced with permission of Sigma-Aldrich Co. LLC from publication name, year, volume, issue and pages"
- and subject to the following restrictions: _____

_____

Authorized Signature _____   Date 5/5/2015

Please submit completed form and any attachments to legal@sial.com

Rev. April 2014

Enabling Science to Improve the Quality of Life